# COMPUTATIONAL FLUID DYNAMIC SIMULATIONS OF MEMBRANE AND RESIN-BASED CHROMATOGRAPHY

BY

UMATHENY UMATHEVA

THESIS

A thesis submitted in partial fulfilment of the requirements
for the degree of Master of Applied Science in Chemical Engineering
in the School of Graduate Studies of
McMaster University, September 2019

Hamilton, Ontario

Examining Committee:

Supervisor: Dr. Raja Ghosh
Committee: Dr. David Latulippe, Dr. P. Ravi Selvaganapathy

**Master of Applied Science, Chemical Engineering**

**McMaster University, Hamilton, Ontario, Canada**

| | |
|---|---|
| **TITLE:** | Computational Fluid Dynamic Simulations of Membrane and Resin-based Chromatography |
| **AUTHOR:** | Umatheny Umatheva |
| **SUPERVISOR:** | Dr. Raja Ghosh |
| **NUMBER OF PAGES:** | i, 89 |

# Abstract

Many of the industrial processes, used by manufacturers to produce biologics, have not been significantly updated since their original design and conception. And thus, there is a great opportunity to update and optimize manufacturing processes. Downstream purification is often considered the bottleneck of the manufacturing process and when biologics are being purified for clinical applications, the final purity is paramount. As a result, pharmaceutical products are subjected to multiple concentration, conditioning, and chromatographic steps. The pharmaceutical industry is constantly and slowly evolving and is always looking to improve efficiency. Simulations and modeling are becoming more commonly used in the pharmaceutical industry as a tool to strategically design and test new production and separation processes developed at the research and development scale. In this thesis, computational fluid dynamics (CFD) modeling was used to develop more efficient bioseparation processes by (1) using a cuboid module geometry and (2) chromatographic medium with product-specific affinity ligands. The laterally-fed class of chromatography modules has a unique cuboidal geometry, with lateral feeding of the sample in the channel above the bed and lateral collection of permeate. CFD simulations and experimental results have shown that the laterally-fed class of chromatography devices can produce sharper elution peaks, have better peak resolution, and consequently purer product fractions than conventional membrane and resin-based chromatographic formats. The enhanced performance by the laterally-fed class of chromatography devices is attributed to improved system fluidics and narrow solute residence time distribution. One other approach to improving efficiency is to address the tradeoff between purity and recovered yield, due to the non-specific binding nature of many commercial resins and membranes. Purification using high-affinity biological ligands selected on specificity to the target molecule could be a feasible solution. A purification scheme for pertactin was developed with final eluate purity of 90% and approximately 100% recovery.

# Acknowledgments

I have been extremely fortunate to work with many people that were able to contribute and influence my professional and personal growth.

To begin, I would like to thank my supervisor, Professor Raja Ghosh, for providing valuable mentorship and letting me explore opportunities and topics I found interesting.

I would like to thank my collaborators at Sanofi Pasteur, Dr. Melih Tamer and Dr. John Riley, for the opportunities I was given to conduct parts of my research in an industrial setting.

I would like to thank Dr. Pedram Madadkar for setting an example for me to follow. Thank you to all the members of the Ghosh lab, both past and present, Dr. Guoqiang Chen, Dr. Seung Mi Yoo, Rahul Sadavarte, Dr. Si Pan and Lionel Alforque who's influence began when I was undergraduate summer student.

Also, I would like to thank my parents and sister for being my cheerleaders. you made it possible to for me to accomplish all that I have, thank you. To my friends, EM, KD, KP, MP, KC, AL, and CV, for their dependable friendship, continual counsel and support, thank you.

# Table of Contents

# List of Abbreviations

| | |
|---|---|
| AC | Affinity chromatography |
| ANOVA | Analysis of variance |
| BSA | Bovine serum albumin |
| CFD | Computational fluid dynamics |
| cP | Component pertussis |
| CV | Colum volume |
| ELISA | Enzyme-linked immunosorbent assay |
| EP | Elution pool |
| EU | Endotoxin unit |
| FCC | Face-centered cubic |
| FEM | Finite element method |
| FHA | Filamentous hemagglutinin |
| FIM | Fimbriae |
| FT | Flow-through |
| HETP | Height equivalent to theoretical plates |
| HIC | Hydrophobic interaction chromatography |
| HP | High performance |
| HPLC | High performance liquid chromatography |
| IEC | Ion exchange chromatography |
| LAL | Limulus amoebocyte lysate |
| LFMC | Laterally -fed membrane chromatography |
| LPS | Lipopolysaccharides |
| LRV | Log reduction value |
| mAb | Monoclonal antibody |
| MC | Membrane chromatography |
| MV | Membrane volume |

| | |
|---|---|
| NSERC | Natural sciences and engineering research council of Canada |
| ORF-RE | Ontario research fund research excellence |
| pI | Isoelectric point |
| PRN | Pertactin |
| PT | Pertussis toxin |
| Q | Quaternary ammonium |
| RTD | Residence time distribution |
| SDS-PAGE | Sodium dodecyl sulfate polyacrylamide gel electrophoresis |
| SM | Starting material |

# Chapter 1

# Introduction

## 1.1 Downstream Purification of Proteins

The manufacture of biological products such as monoclonal antibodies, enzymes, and vaccine begin in upstream processes. In these stages, the cells are isolated, and cultured to quantities to be purified. Downstream processes describe all the steps that take place following the completion of microbial fermentation to purify target molecules. The purification of biological products often follows the CiPP (capture, intermediate purification, and polishing) strategy (Ghosh, 2006; Lightfoot and Moscariello, 2004). In this scheme, the primary capture step isolates and concentrates the target proteins, intermediate purification removes bulk material and polishing steps remove difficult impurities. The primary capture step uses low-resolution methods such as precipitation, filtration, and centrifugation to reduce the volume being processed. The intermediate purification and polishing steps are high-resolution methods of targeted chromatography to achieve the desired purity of the product. The main challenge with this approach to protein purification is that there is a tradeoff between the recovered yield and the purity (Ghosh, 2006; Lightfoot and Moscariello, 2004). In applications where the proteins are purified for therapeutic purposes, the final product must meet strict regulatory limits in allowable impurities.

Protein purification is based on differences in the physicochemical properties of the proteins in the mixture. Many intermediate purification steps are based on protein characteristics such as polarity, electrostatic charge, and hydrophobicity (Ghosh, 2006; Lightfoot and Moscariello, 2004). In chromatographic separation, targeted isolation of the molecule of interest is done by selecting a stationary phase and properties of the binding and eluting buffers to bind the target molecule to the stationary phase. After other impurities are washed away, the bound molecules are stripped from the support following a gradient or step change to the elution buffer.

### Ion Exchange Chromatography (IEC)

The driving force of ion-exchange chromatography is electrostatic interaction between the target molecule and the stationary media, which contains charged groups (Fekete et al., 2015). In cation-exchange chromatography, the support matrix is negatively charged and the target molecule in the feed material is a net positive. Whereas in anion-exchange chromatography the support matrix is positively charged and the target molecule in the feed

material is a net negative. The charge of the target molecule can be modified by pH such that in pH conditions below the isoelectric point (pI) the protein is net positive and when the pH is above the pI, it is a net negative. This chromatographic method is particularly useful when the target molecule has a pI that is greatly different from the impurities of the feed.

## Hydrophobic Interaction Chromatography (HIC)

Proteins are comprised of hydrophilic and hydrophobic amino acids residues. Hydrophobic interaction chromatographic is based on the strength of the interaction between the hydrophobic regions of the target molecules and the stationary media (Queiroz et al., 2001). The mobile phase will have a high concentration of an anti-chaotropic salt such as ammonium sulphate or sodium sulphate which will promote adsorption of protein via hydrophobic residues onto the ligands of the stationary media. Once the protein is bound to the support matrix, elution can be achieved by decreasing the salt concentration.

## Affinity Chromatography (AC)

Affinity chromatography was first introduced as a method for purifying biological products by curatreaceas et als as a method that exploited the highly specific binding interaction between a ligand and a target molecule (Cuatrecasas, 1970a, 1970b; Cuatrecasas et al., 1968; Cuatrecasas and Anfinsen, 1971). The shape of the ligand is complementary to the target molecule and once the ligand-molecule complex is formed it is held together by a non-covalent interactions (i.e. hydrogen bonding, van der Waals forces, and hydrophobic interaction). This reaction is reversible upon the change in the environment which results in conformational changes in the ligand.

## Laterally-Fed Class of Chromatography Devices

The laterally-fed class of chromatographic devices is a collection of novel membrane and packed-bed chromatography devices that have a cuboidal or rectangular geometry (Madadkar et al., 2015; Madadkar and Ghosh, 2016; Ghosh et al., 2016; Ghosh, 2016). In these devices, fluid is guided along channels above the bed and collected in laterally towards the outlet. The fluidics of this design lends itself to improved resolving abilities compared to conventional formats by reducing the residence time distribution. The laterally-fed membrane chromatography (LFMC) device has an improved design that produces a high-resolution purification of multicomponent feed material, which makes membrane-based modules suitable for intermediate purification, in addition to final polishing steps (Madadkar et al., 2015). The packed-bed cuboid is based on the same flow features of the LFMC device (Ghosh, 2016). This module is designed for improved resolving capabilities in applications where resin-based media is preferred.

## 1.2 CFD in the Pharmaceutical Industry

The interest in modern process and product development technology such as computational fluid dynamics (CFD) is increasing in the pharmaceutical industry in response to greater expectations from customers, demands for greater profitability and tighter FDA regulations (Pordal et al., 2002). Currently, the industry is under immense pressure to improve efficiency in all aspects (i.e. process, time, resources, etc.) and it is not uncommon for process and product development to occur simultaneously. As a result, tools and methods for rapid prototyping and analysis are required. CFD technology, originally used in applications of mechanical and aerospace engineering, is a tool being adopted by the pharmaceutical industry (Joshi and Ranade, 2003; Pordal et al., 2002). The use of CFD methods has the potential to shorten product-process development cycles, improve optimization of existing processes, aid in efficient designing of new products and processes, and reduce time to market (Joshi and Ranade, 2003; Pordal et al., 2002). It can be used to analyze operations of mixing, separation, and purification and drying. Since many industrial unit operations process large volumes of fluid, any improvements in efficiency and performance can be translated into an increase in revenue and decrease costs.

CFD simulations are based on the first principles of mass, momentum, and energy conservation. Since the work being discussed in this thesis is based on chromatographic unit operations, the Navier-Stokes (conservation of momentum), continuity equation (conservation of mass), species mass balances and Brinkman equations for flow in porous domains are usually numerically solved.

## 1.3 Thesis structure

This thesis report is structured as a hybrid thesis comprising of published and unpublished projects. Chapters 2, 4 and 5, are standalone chapters that have been published or are prepared manuscripts for publication. Chapters 3 and 6 are mini-chapters that are directly related to the preceding chapters.

Chapter 1
*Introduction*
This chapter introduces key concepts and structure of this thesis.

Chapter 2
*Computational fluid dynamic (CFD) simulation of laterally-fed membrane chromatography*
This chapter is a CFD study comparing the fluidics of the laterally-fed membrane chromatography and the stacked disc devices. This study identifies the key characteristics of the LFMC design that allows for high-resolution protein separation. This chapter has been published in *Chemical Engineering Research and Design*.

Chapter 3
*An evaluation of a radial flow membrane adsorber and a laterally-fed membrane chromatography device*
This chapter is a CFD study comparing the fluidics of the laterally-fed membrane chromatography module and the radial flow devices. This study identifies flow pattern attributes of the radial flow device that limits its use in high-resolution purification applications.

Chapter 4
*Computational fluid dynamic (CFD) simulation of a cuboid packed-bed device*
This chapter is a CFD study comparing the fluidics of the cuboid packed-bed with the conventional packed-bed column. This work identifies common challenges with the conventional configuration, in terms of fluidics, and shows how the cuboidal format addresses these concerns. This chapter with minor revisions has been submitted to *Chemical Engineering Research and Design*.

Chapter 5
*Purification of bacterial virulence factor pertactin using high affinity ligands*
This chapter follows an industry partnered project with Sanofi Pasteur. It includes a design of experiments for design space screening of a new affinity chromatographic method, using biological high-affinity ligand, for the purification of Pertactin.

Chapter 6
*CFD simulations of pertactin purification by affinity chromatography*
This chapter models the bind and elute mode of operation of an affinity chromatography column.

Chapter 7
*Conclusion and Future work*
This chapter summarizes the major contributions from this thesis and directions of future work.

# References

Cuatrecasas, P., 1970a. Agarose Derivatives for Purification of Protein by Affinity Chromatography. Nature 228, 1327–1328. https://doi.org/10.1038/2281327a0

Cuatrecasas, P., 1970b. Protein Purification by Affinity Chromatography Derivatizations of agarose and polyacrylamide beads. J. Biol. Chem. 245, 3059–3065.

Cuatrecasas, P., Anfinsen, C.B., 1971. [31] Affinity chromatography, in: Methods in Enzymology, Enzyme Purification and Related Techniques. Academic Press, pp. 345–378. https://doi.org/10.1016/0076-6879(71)22033-4

Cuatrecasas, P., Wilchek, M., Anfinsen, C.B., 1968. Selective enzyme purification by affinity chromatography. Proc. Natl. Acad. Sci. 61, 636–643. https://doi.org/10.1073/pnas.61.2.636

Fekete, S., Beck, A., Veuthey, J.-L., Guillarme, D., 2015. Ion-exchange chromatography for the characterization of biopharmaceuticals. J. Pharm. Biomed. Anal., REVIEW 2015 113, 43–55. https://doi.org/10.1016/j.jpba.2015.02.037

Ghosh, R., 2016. Using a box instead of a column for process chromatography. J. Chromatogr. A 1468, 164–172. https://doi.org/10.1016/j.chroma.2016.09.044

Ghosh, R., 2006. Principles of Bioseparations Engineering. World Scientific Publishing Company.

Ghosh, R., Madadkar, P., Wu, Q., 2016. On the workings of laterally-fed membrane chromatography. J. Membr. Sci. 516, 26–32. https://doi.org/10.1016/j.memsci.2016.05.064

Joshi, J.B., Ranade, V.V., 2003. Computational Fluid Dynamics for Designing Process Equipment: Expectations, Current Status, and Path Forward. Ind. Eng. Chem. Res. 42, 1115–1128. https://doi.org/10.1021/ie0206608

Lightfoot, E. n., Moscariello, J. s., 2004. Bioseparations. Biotechnol. Bioeng. 87, 259–273. https://doi.org/10.1002/bit.20111

Madadkar, P., Ghosh, R., 2016. High-resolution protein separation using a laterally-fed membrane chromatography device. J. Membr. Sci. 499, 126–133. https://doi.org/10.1016/j.memsci.2015.10.041

Madadkar, P., Wu, Q., Ghosh, R., 2015. A laterally-fed membrane chromatography module. J. Membr. Sci. 487, 173–179. https://doi.org/10.1016/j.memsci.2015.03.056

Pordal, H.S., Matice, C.J., Fry, T.J., 2002. The role of computational fluid dynamics in the

pharmaceutical industry. Pharm. Technol. 26, 72.

Queiroz, J.A., Tomaz, C.T., Cabral, J.M.S., 2001. Hydrophobic interaction chromatography of proteins. J. Biotechnol. 87, 143–159. https://doi.org/10.1016/S0168-1656(01)00237-1

Ramos-de-la-Peña, A.M., González-Valdez, J., Aguilar, O., 2019. Protein A chromatography: Challenges and progress in the purification of monoclonal antibodies. J. Sep. Sci. 42, 1816–1827. https://doi.org/10.1002/jssc.201800963

# Chapter 2

# CFD simulations of laterally-fed membrane chromatography

This chapter is a comparison of the LFMC device and the stacked disc device. The evaluation looks at system fluidics and its effects on solute residence time distribution. This paper explains the high resolution capabilities of membrane chromatography when used in the LFMC device format.

In this work, I completed the CFD simulations and was the primary author of the manuscript. Dr. Pedram Madadkar helped with my initial understanding of the LFMC device and method. Dr. Ravi Selvaganapathy provided an introduction to CFD and edited the manuscript. Dr. Raja Ghosh supervised the project and edited the manuscript. This chapter is published in Chemical Engineering Research and Design.

*Computational fluid dynamic (CFD) simulation of laterally-fed membrane chromatography*
Umatheny Umatheva, Pedram Madadkar, P. Ravi Selvaganapathy and Raja Ghosh

Chemical Engineering Research Design, 137 (2018), pp. 412-420
DOI: 10.1016/j.cherd.2018.07.026

# Computational fluid dynamics (CFD) simulation of laterally-fed membrane chromatography

Umatheny Umatheva[a], Pedram Madadkar[a], P. Ravi Selvaganapathy[b], Raja Ghosh[a*]

[a] Department of Chemical Engineering, McMaster University
[b] Department of Mechanical Engineering, McMaster University

[*]Corresponding Author
Email: rghosh@mcmaster.ca
Phone: +1 905−525 9140 ext 27415

**Abstract**
Currently, most bioseparation processes used for purification of bio-pharmaceutical products such as vaccines, monoclonal antibodies, and enzymes use resin-based column chromatography. Resolution and productivity are two of the major factors that should be optimized in any purification process. While column chromatography techniques give high-resolution and consequently very high product quality, they are slow, leading to low productivity and high production cost. One of the alternatives to resin-based columns is membrane chromatography, where a stack of membrane sheets is used as chromatographic media. Membrane chromatography is a fast and scalable technique; however, it is not commonly used for some of the critical purification steps due to its low-resolution capability. A technique newly developed in our group called laterally-fed membrane chromatography (or LFMC) combines high-resolution separation with high-productivity. It is, therefore, suitable for rapid, multicomponent protein purification. LFMC not only gives a higher resolution than other membrane chromatography devices, but it also gives comparable resolution to that obtained with equivalent resin-based packed bed columns, even at significantly higher flow rates, as demonstrated in our previous work. This paper examines the system fluid dynamics in an LFMC device using computational fluid dynamics (CFD) simulations and explains the reasons behind its superior separation attributes.

**Keywords:** membrane chromatography, membrane device, laterally-fed membrane chromatography, computational fluid dynamics, bioseparation

# Introduction

Two very important factors that should be optimized in any purification technique are resolution and productivity. Currently, the gold standard technique used for bioseparation, i.e. purification of biological products such as biopharmaceuticals, is resin-based column chromatography which gives excellent resolution (Przybycien et al., 2004). However, the dominant transport mechanism in column chromatography is diffusion, which slows down the process and thereby decreases productivity and increases production cost (Farkas et al., 1997, 1996, 1994). For biopharmaceutical products, a longer purification time also increases the risk of product degradation and aggregation. Therefore, an ideal bioseparation process should combine high-resolution with high-productivity.

Membrane chromatography is an alternative to column chromatography which uses a stack of porous membrane sheets as chromatographic media. Conventional membrane chromatography is a fast and scalable technique, suitable for purification of biological products (Orr et al., 2013; Suen et al., 2003). However, it cannot be used where high-resolution separation is required. It is instead more commonly used in low-resolution polishing type applications. Commonly used conventional membrane chromatography devices include stacked disc and radial flow devices (Ghosh et al., 2013; Ghosh and Wong, 2006; Teepakorn et al., 2016). The stacked disc device, like the packed bed column, has a cylindrical geometry and as a result, the central region of the stack gets saturated with solute much earlier than the peripheral regions. This leads to inefficient use of the membrane volume. In a radial flow device, the membrane sheets are spirally wound leading to large dead volumes on both the feed and permeate side of the membrane roll. In addition, the radial flow design leads to varying membrane area along the bed height which could adversely affect the resolution (Li and Tung, 2008). Moreover, both stacked disc and radial flow devices suffer from poor flow distribution and other design deficiencies which lead to shallow breakthroughs and highly inefficient use of the membrane binding capacity.

Efficient module design centered around superior flow distribution within the device greatly affects the separation performance in membrane chromatography (Marriott and Sorensen, 2003). In our group, we developed laterally-fed membrane chromatography (LFMC) specifically to address some of the design deficiencies of currently used membrane chromatography modules and thereby combine high-resolution with speed in multicomponent protein separations (Ghosh et al., 2016; Madadkar et al., 2017, 2016, 2015; Madadkar and Ghosh, 2016). The LFMC device is based on the use of a stack of rectangular flat sheet membranes (see Figure 2.1) (Ghosh et al., 2016; Madadkar et al., 2017, 2016, 2015; Madadkar and Ghosh, 2016). The feed fluid enters the module through a top or feed channel, penetrates the membrane stack at different locations along its length, and eventually emerges on the other side of the membrane stack. The emerging fluid is collected in the bottom or permeate channel and is directed towards the device outlet. The lateral channels typically contain pillar arrays or other types of flow distributors for increasing the flow uniformity and for supporting the membrane stack and holding it in place.

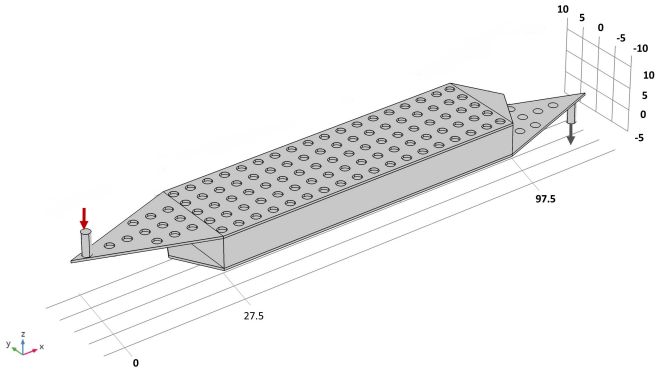


Figure 2.1: Laterally-fed membrane chromatography module

Recently published studies have shown that the resolution obtained with LFMC is significantly better than that of a stacked disc and radial flow membrane modules, and is comparable to that obtained with equivalent resin-based packed bed chromatography (Ghosh et al., 2016; Madadkar et al., 2017, 2016, 2015; Madadkar and Ghosh, 2016). The LFMC module has significantly (i.e. 3-9 times) more theoretical plates compared to equivalent commercial columns, especially during higher flow rate separation (Sadavarte et al., 2018). This paper examines the fluid dynamics within an LFMC device using computational fluid dynamics (CFD) simulations to explain some of the reasons for its superior separation performance. Although radial flow devices are widely used in polishing steps in many bioseparation processes, they are not suitable for bind and elutde separation applications. A comparison of the separation efficiency (in terms of resolution) between the LFMC, the stacked disc, and radial flow devices clearly show the radial flow device gives the worst performance (Ghosh et al., 2016; Madadkar et al., 2015; Madadkar and Ghosh, 2016). In this study, we have therefore chosen to focus our attention on a CFD based comparison between the two better performing devices, i.e. the LFMC and stacked disc devices.

# Model Setup

Computational fluid dynamics (CFD) modeling technology is an established tool in the aerospace and automotive industries and is increasingly being used in the chemical (Joshi and Ranade, 2003; Naveen Pathak et al., 2008). Recently, the pharmaceutical industry has begun to shown interest in using CFD modeling to provide insight on fluid flow in equipment to help reduce risks associated with scale-up of process equipment and for troubleshooting (Joshi and Ranade, 2003; Kremer and Hancock, 2006; Naveen Pathak et al., 2008; Pordal et al., 2002). CFD models provide the opportunity to study changes in design parameters and operating conditions without running wet lab experiments. However, the accuracy and reliability of a CFD model depend on factors such as accuracy of model initial and boundary conditions, computational numerical accuracy, and scientific understanding of the governing laws and the nature of the fluids (Joshi and Ranade, 2003; Kremer and Hancock, 2006; Naveen Pathak et al., 2008; Pordal et al., 2002).

COMSOL Multiphysics 5.2a was used to model the fluidics within an LFMC device. The specific device modeled was used in our earlier experimental studies (Madadkar et al., 2016; Madadkar and Ghosh, 2016). The steady-state model was built using the *Reacting Flow, Diluted Species* physics package and the transient study was conducted using *Particle Tracing for Fluid Flow* physics package. COMSOL Multiphysics uses the finite element method (FEM) when solving models. The software runs the finite element analysis with adaptive meshing using an assortment of numerical solvers.

## Fluid Flow

CFD models are based on the solution of the fundamental conservation laws of mass, momentum, and energy. These laws are described as partial differential equations that are solved numerically. The equations that were solved in the LFMC model are Navier–Stokes equation (Equation 2.1), and the Brinkman equations (Equation 2.2), which are extensions of the Navier–Stokes and continuity equations in porous media (Brinkman, 1949). The Navier-Stokes equation can be simplified since the fluid in the devices is incompressible as seen in Equation 2.1b. In the Navier–Stokes equation, the inertial forces are balanced with the sum of the pressure forces, viscous forces and any external forces applied to the fluid. Both the Navier-Stokes and Brinkman equations are solved together with the continuity equation (Equation 2.3), more specifically Equation 2.3b for an incompressible fluid. The Navier-Stokes equation represents the conservation of momentum, whereas the continuity equation represents the conservation of mass.

$$\left(\frac{\partial \rho u}{\partial t} + \rho u \cdot \nabla u\right) = \nabla P + \nabla \cdot (\mu(\nabla u + (\nabla u)^T) - \frac{2}{3}\mu(\nabla u)) + F \tag{2.1a}$$

$$\rho\left(\frac{\partial u}{\partial t} + u \cdot \nabla u\right) = \nabla P + \nabla \cdot (\mu(\nabla u + (\nabla u)^T)) + F \tag{2.1b}$$

$$\frac{\rho}{\epsilon}\left(\frac{\partial u}{\partial t} + (\nabla \cdot u)\frac{u}{\epsilon}\right) = -\nabla P + \nabla \cdot \left(\frac{1}{\epsilon}(\mu(\nabla u + (\nabla u)^T))\right) + \left(\frac{\mu}{K_b} + Q_{in}\right) u \tag{2.2a}$$

$$\frac{\partial(\epsilon\rho)}{\partial t} + \nabla \cdot (\rho u) = Q_{in} \tag{2.2b}$$

$$\frac{\partial \rho}{\partial t} + \nabla \cdot (\rho u) = 0 \tag{2.3a}$$

$$\nabla \cdot u = 0 \tag{2.3b}$$

The above equations are solved using a set of model parameters such as inlet, outlet and physical parameters, which are shown in Table 2.1. The model was solved with no-slip boundary conditions at the walls and at the boundary at the channel-membrane interface the Stokes velocity in the channel equaled the Brinkman velocity in the porous media.

The initial and boundary conditions were taken from previously published experimental conditions for consistency and for model validation (Madadkar et al., 2016; Madadkar and Ghosh, 2016). Both models were modeled with a tetrahedral mesh, with finer element size used in the pillared channels and courser element size used in the membrane stack. Identical results were achieved for course and normal mesh sizes in the bed.

Table 2.1: Model parameters used in the CFD steady-state simulation for stacked dick and LFMC devices (Madadkar et al., 2016; Madadkar and Ghosh, 2016)

| Parameter | Value | |
|---|---|---|
| $L$ | Length (m) | 0.07 |
| $W$ | Width (m) | 0.02 |
| $R$ | Stacked disc radius (m) | 0.0211 |
| $h_c$ | Channel/header height (m) | $5\times10^{-4}$ |
| $h_b$ | Packed-bed height (m) | $6.6\times10^{-3}$ |
| $Q_{in}$ | Inlet flow rate ($m^3/s$) | $2.5\times10^{-7}$ |
| $\epsilon$ | Sartobind S Porosity (-) | 0.78 |
| $K_b$ | Sartobind S permeability ($m^2$) | $1.18\times10^{-14}$ |
| $T$ | Temperature (K) | 298.15 |
| $D_{NaCl}$ | Diffusion coefficient of NaCl in water ($m^2/s$) | $2.9\times10^{-9}$ |
| | Relative tolerance (-) | $10^{-3}$ |

### Particle Tracing and Residence Time Distribution

Table 2.2: Additional model parameters used in the CFD transient simulation)

| Parameter | Value | |
|---|---|---|
| $\rho_p$ | Density of Tracer particle ($kg/m^3$) | 968 |
| $d_p$ | Tracer particle diameter (m) | $2.27\times10^{-10}$ |

The transient study was completed using *Particle Tracing for Fluid Flow* physics package. In this study, 1000 tracer particles were tracked. The motion of these particles is defined by Newton's second law. The velocity field was calculated at steady state, which was then used to determine the particle motion in the LFMC. Additional model parameters used in the transient simulation are shown in Table 2.2. The residence time of each of the particles was computed and plotted as a distribution.

## Results and Discussion

In a recent paper (Ghosh et al., 2016), we analyzed the fluidics in an LFMC and in a stacked disc device using mass balance based mathematical models and validation experiments. This paper will revisit many of the claims on fluid distribution and residence time using more rigorous CFD models. This study gives a more in-depth explanation using tracer

and RTD data on how the channel and header design effects the resolution performance. In addition, the model gives insight on pressure and velocity profiles within the membrane bed which are difficult to measure experimentally.

## LFMC

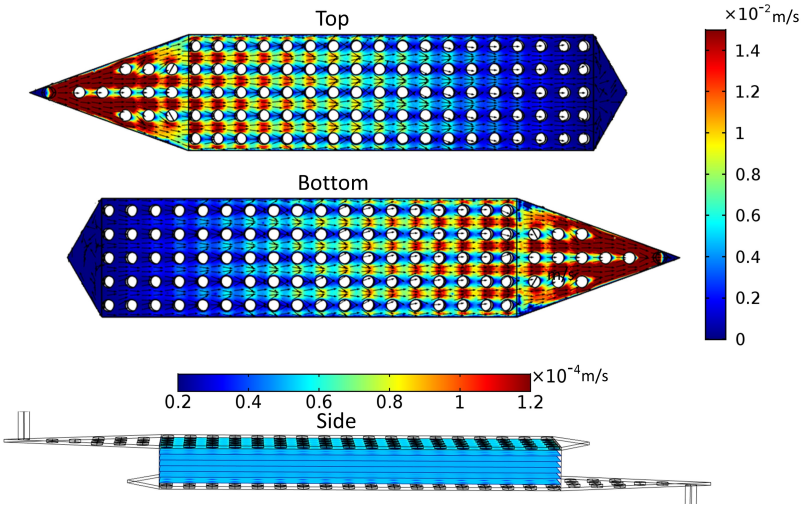


Figure 2.2: Velocity in flow distributing channels and membrane bed when the volumetric flow rate is 15 mL/min

The inlet region of the LFMC module was designed specifically to disperse the flow coming in from external piping and to allow for flow development before entering the region of the channel above the membrane bed. In the physical devices, the desired bed height is achieved by stacking multiple layers of membrane sheets. The stacked sheets provide a more uniform flow distribution and any defects in a particular layer can be compensated for by the flow through the subsequent sheets (van Reis and Zydney, 2007), as a result, the bed region was modeled as a homogenous porous region. In addition, the membrane permeability used in the models was assumed to be constant and was based on the assumption that the fluid would flow through the membrane stack (i.e. z-direction). Figure 2.2 shows the velocity distribution in the top and bottom channels as well as the membrane stack. The influent liquid has the highest velocity and the velocity of the liquid in the top channel decreases along the length (x-axis) as fluid permeates into the membrane stack below. The velocity vectors indicate that the fluid travels laterally along the length of the top channel with slight mixing due to the presence of the pillars. The aligned nature of the pillar array gives rise to stagnant regions behind each pillar and this is the primary contributor to the variations in the velocity along the y-axis. Figure 2.2 shows that the velocity profiles in the top and bottom channels are almost mirrored images of each other. Figure 2.3 shows the magnitude of liquid velocity changes with length in the top and bottom channels, along three sets of lines indicated in Figure 2.3 (A: y = -2, 2; B: y = -6, 6; C: y = -9.8, 9.8). The velocity decreases linearly, at all locations in the y-axis, in the top channel above the membrane bed. The linear decrease in velocity in the top channel agrees with our previous claim, made using the

mass balance based model, that the rate is equal to the permeate flux divided by the channel height (Ghosh et al., 2016). Modifying the array pattern to a staggered configuration would make the velocity in the y-direction more uniform. When all the liquid has been collected in the bottom channel, the net velocity at the outlet is identical to that at the top channel inlet as could be expected with an incompressible liquid.

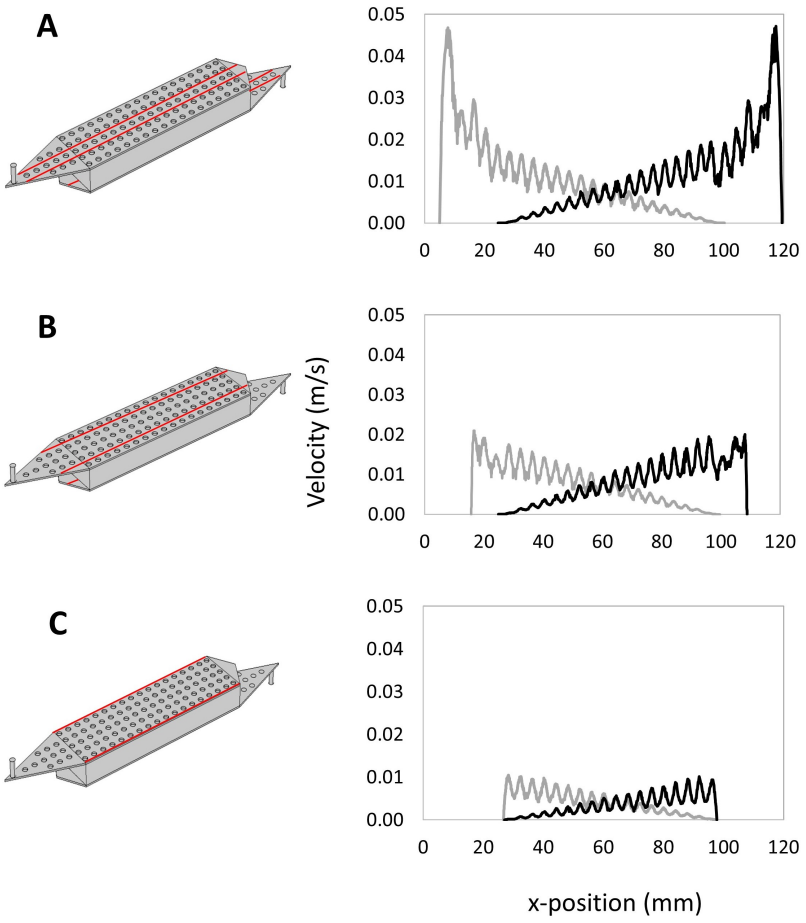


Figure 2.3: Velocity in flow distributing channels at A) y = -2, 2 B) y = -6, 6 C) y = -9.8, 9.8. (Grey line: top channel, Black line: bottom channel)

In our earlier paper (Ghosh et al., 2016), we elucidated that for the efficient functioning of an LFMC device, the hydraulic resistance in the lateral channels have to be identical, and these, in turn, have to be significantly lower in magnitude than that in the membrane stack. Figure 2.4 summarizes the pressure drop in the different sections and regions within the LFMC device. Figure 2.4A shows the pressure in the feed and permeate channels along the x-direction. Quite clearly, the pressure drop in the channels was negligibly low. The pressure drop of the module and AKTA system, reported in previous publications (Madadkar et al., 2016; Madadkar and Ghosh, 2016), was about 40 kPa. Considering the pressure losses associated with the tubing and fittings used to connect the module to the AKTA system,

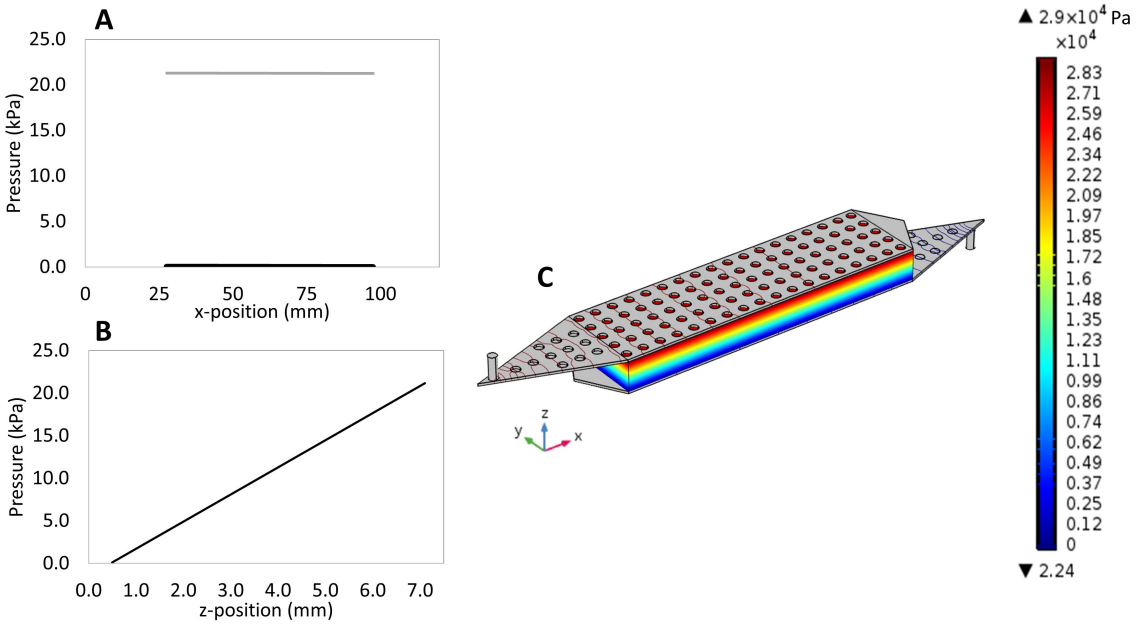


Figure 2.4: A) Gauge pressure in flow distributing channels at y = 2, -2. (grey line: top channel, black line: bottom channel) B) Gauge pressure value though membrane bed C) Pressure contours in LFMC device when the volumetric flow rate is 15 mL/min

it is reasonable to have a net pressure drop of 21.3 kPa across the membrane stack. The pressure decreases linearly across the membranes stack, i.e. in the z-direction, as expected for an incompressible fluid moving within a porous bed of constant permeability. As seen in Figure 2.4A and 2.4B, the pressure drop and thereby the hydraulic resistance in the top and bottom channels, i.e. along the x-direction, were significantly lower than the corresponding values within the membrane stack, i.e. along the z-direction. Therefore, the experimental conditions (Madadkar et al., 2016; Madadkar and Ghosh, 2016) were ideal for the efficient functioning of the LFMC device. The pressure contour lines (Figure 2.4C) also show that the pressure in any x-y plane within the membrane stack was uniform. Therefore, the flow of liquid within the membrane stack took place only in the normal or z-direction.

## Stacked Disc

The LFMC module was compared in a head to head manner with a hypothetical equivalent stacked disc device. The devices both had the same cross-sectional area, bed height, channel height and dead volume. As can be seen in Figure 2.5A, the top header in the stacked disc device could not effectively distribute the centrally fed fluid to the peripheral regions. The velocity profiles in the feed and permeate headers look identical, i.e. the liquid velocity was very high near the center and decreased very significantly in a radially outward direction. As discussed in our previous paper (Ghosh et al., 2016), on the feed side, the fluid begins to permeate the membrane upon entering the module and the cross-sectional area for flow in the header increases radially, causing a rapid decrease in velocity, as seen in Figure 2.5B. The radial velocity curve is not smooth due to mixing effects caused by the pillars. The

rapid decrease in radial velocity in the header results in an inefficient use of the peripheral regions of the membrane. As a result, membrane utilization efficiency is drastically reduced.

Figure 2.6 summarizes the pressure drop in the membrane stack and the headers of the stack disc device. Figure 2.6A shows that the pressure change in the headers along the radial direction was negligible. The net pressure drop across the membrane bed was 31.5 kPa (see Figure 2.6B). The pressure decreased linearly along the z-direction, i.e. across the membrane stack as could be anticipated for an incompressible fluid moving through porous media with constant permeability. Figure 2.6C shows the pressure contours through the membrane stack which indicates that the pressure drop was uniform, as a result, permeate flux could also be expected to be uniform. Therefore, the difference in performance between an LFMC device and a stacked disc could be attributed to differences in fluid flow adjacent to the respective membrane stacks, i.e. in the channels and headers. This is consistent with the analysis and conclusions of our earlier paper (Ghosh et al., 2016).

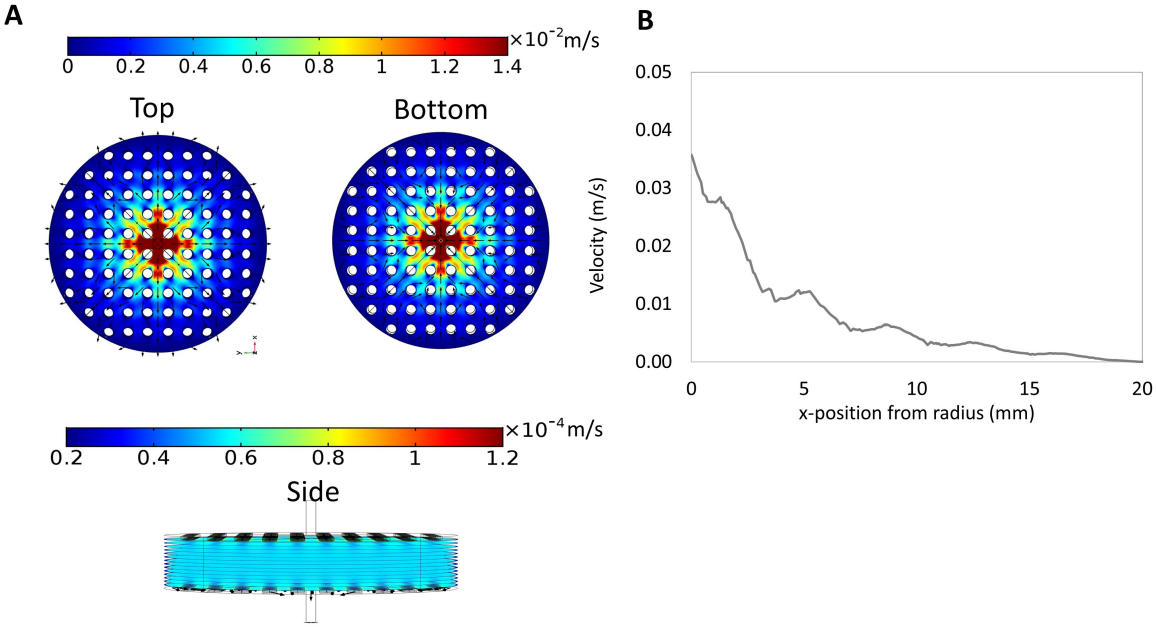


Figure 2.5: Velocity in flow distributing header and membrane bed when the volumetric flow rate is 15 mL/min B) Velocity magnitudes along radius of stacked disc

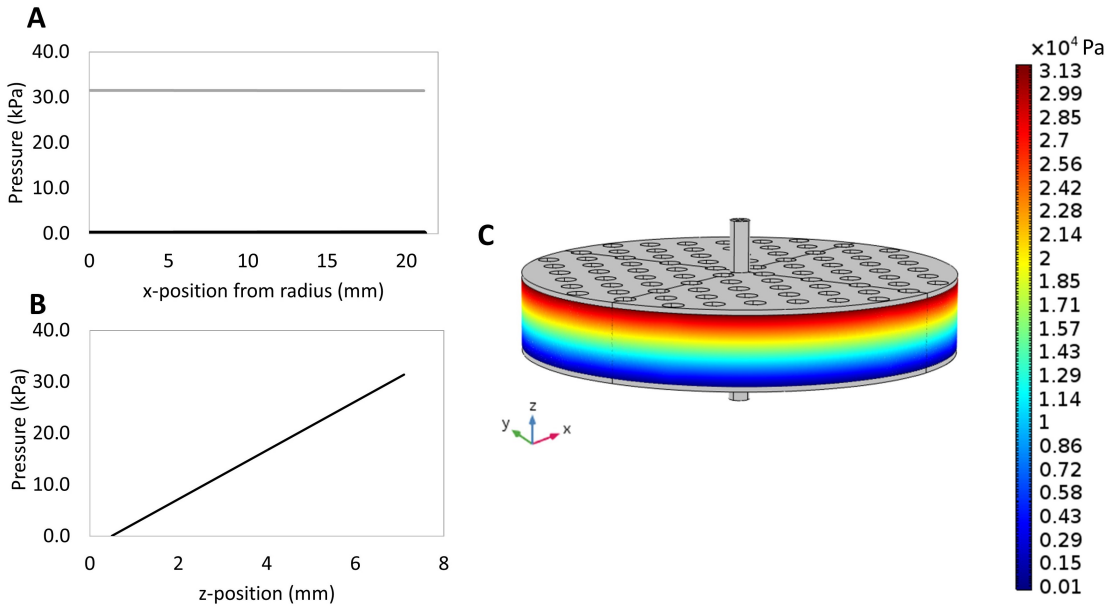


Figure 2.6: A) Gauge pressure in flow distributing headers along radius. (grey line: top header, black line: bottom header) B) Gauge pressure value though membrane bed C) Pressure contours in stacked disc when the volumetric flowrate is 15 mL/min

## Residence Time

As discussed in our earlier papers (Ghosh et al., 2016), the higher resolution obtained with the LFMC device could be primarily attributed to the uniformity in solute flow path length and thereby the narrower residence time distribution (RTD). Uniformity in residence time within a chromatography device results in a sharper elution peak and thereby higher separation efficiency, and consequently a purer product (Yuan et al., 1999). Figure 2.7A shows the RTD for the LFMC device based on the injection of a pulse containing 1000 tracer particles, that flow through the device and do not have any binding or affinity to the separation material. Although the contact of tracer particles with the membrane stack was varying along the x-axis and y-axis, the path lengths were similar since the particles travel the length of $2h_c + h_b + L$ and any additional distance along the y-axis was considered insignificant due to the greater influence of x-dimension of the module. The uniformity of the path length in conjunction with the nature of the velocity changes in the feed and permeate channels, i.e. linear decrease in the top, linear increase in the bottom channels respectively, could be the cause for the narrowness of the RTD. Figure 2.7B shows the corresponding RTD for the stacked disc which was modeled as a one-eight wedge taking advantage of the axial symmetry of the membrane stack housed within the device. The broadness of the RTD could be attributed to a combination of factors. Firstly, the variability in particle path length was considerably greater with the stacked disc device. Particles along the center travelled a distance of $2h_c + h_b$, whereas all other particles traveled a distance of $2h_c + h_b + 2f(R)$. In addition, the corresponding the fluid velocities in the feed and permeate headers experienced by particles traveling various paths had a significant impact on the RTD. The residence time

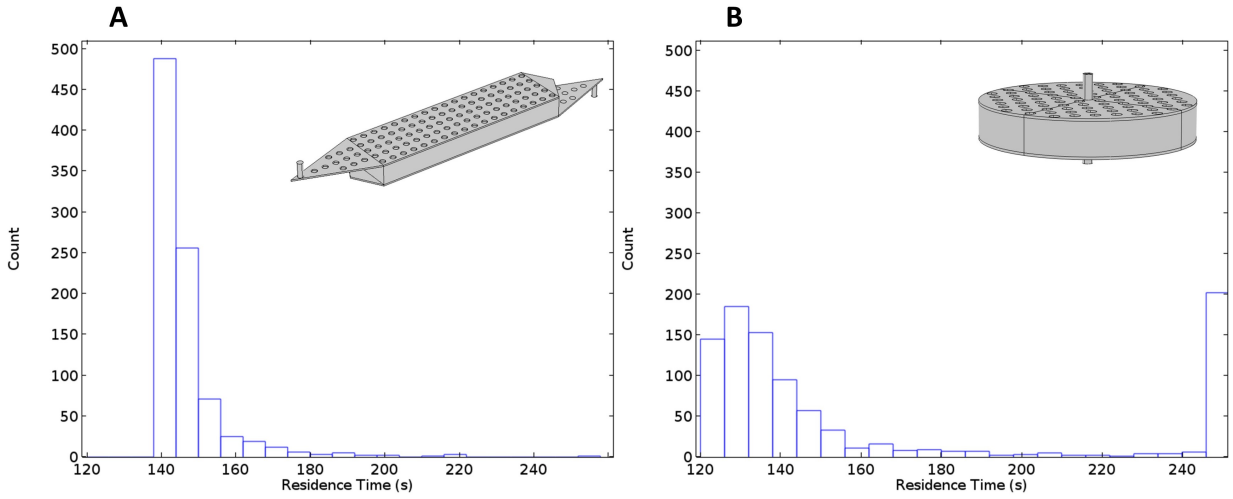


Figure 2.7: Residence time distribution of 1000 tracer particles at flowrate of 15 mL/min in the A) LFMC device and B) stacked disc device

bin corresponding to 250 s represents particles that were delayed within the device due to slow moving fluid in the peripheral regions and pillars of the device. This could have a significant influence on the resolution of separation when using the bind and elute mode of separation, i.e. resolution could be drastically reduced. Figure 2.8A and 8B show the residence time plot for the 1000 particles as a function of the lateral or radial location within the membrane stack in the LFMC and stacked disc devices respectively, through which they traverse. As can be seen from the figure, with the LFMC module the residence time was relatively independent of lateral location (i.e. x-axis). The slight variations in the residence time are probably due to stagnant regions generated behind the pillars. In the stacked disc device, the residence time increase very significantly in the radial direction due to a combination of longer path lengths and diminishing radial velocity. Once again, the jaggedness in the profile was caused by fluid stagnation behind pillars. The CFD model predictions on residence time corresponding to lateral and radial position shown in Figure 2.8 are consistent with those obtained by first principle mathematical models, and reported in a previous paper (Ghosh, 2016). In addition, particles also get retained longer due to flow disturbances caused where the inlet and outlet connectors meet the feed and permeate headers. The above results are consistent with the hypotheses and conclusions of our earlier paper (Ghosh et al., 2016).

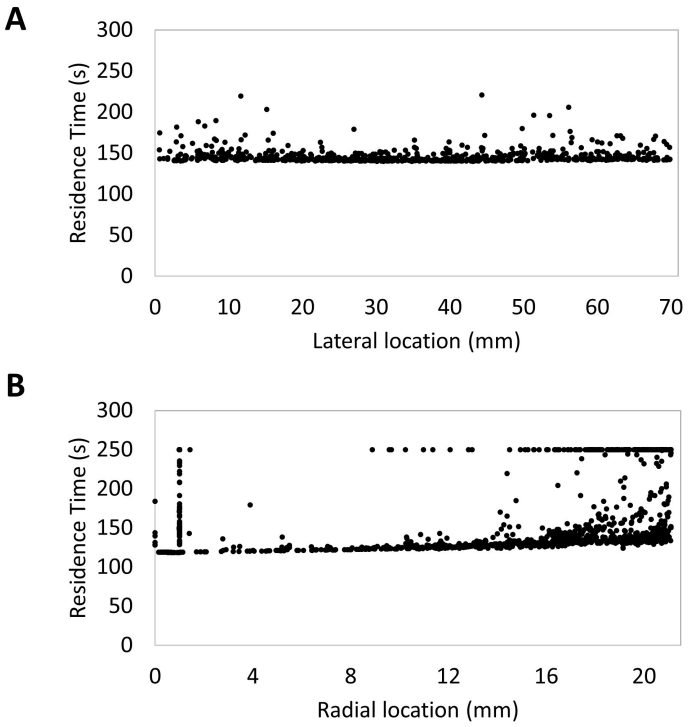


Figure 2.8: Residence time of particles entering different locations in the membrane stack in the A) LFMC device, and B) stacked disc device

Figure 2.9A and 2.9B show the movement of tracer particles in the LFMC and the stacked disc device respectively over the course of 160 s at a flow rate of 15 mL/min. The particles moved through the membrane bed within the LFMC device with a slight upward flection near the end of the device. This facilitated collimation, i.e. collection of the particles in a tight and concentrated fraction at the device outlet, thus ensuring a narrow RTD. In the stacked disc device, the upward flection at the peripheral regions was significant. However, in this case, it delayed the particles traversing the peripheral regions, resulting in broadening of the RTD. In a bind and elute type separation, a narrower RTD ensures elution of a component as a tight band, i.e. as a sharp peak. This results in higher resolution when multiple eluted components are being separated. The above results clearly explain why the LFMC device gives better resolution in multi-component separation than its equivalent stacked disc device. These results and explanations are consistent with the hypotheses, analysis, and conclusions of our earlier paper (Ghosh et al., 2016).

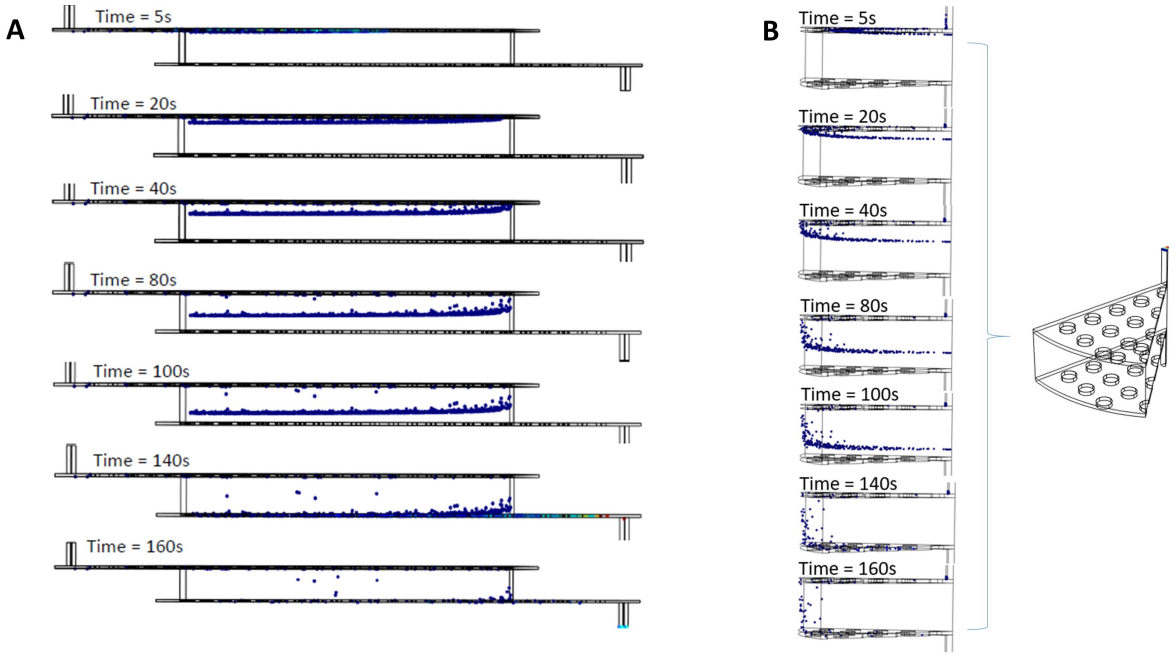


Figure 2.9: Movement of tracer particles at a flow rate of 15 mL/min in the A) LFMC device and B) one-eighth wedge of an equivalent stacked disc device

# Conclusion

Module design and thereby the nature of fluid flow within a separation device affects the efficiency of separation. The laterally-fed membrane chromatography (LFMC) class of devices were designed to address the design deficiencies of currently used commercial membrane chromatography devices which are suitable for fast separations but give extremely poor resolution in multi-component chromatographic separation. By doing so, membrane chromatography could be made suitable for high-speed, high-resolution bioseparation applications. The superiority of the LFMC device over a stacked disc device has been explained based on CFD simulation. The primary contributors for superior separation efficiency with the LFMC device were improved fluid flow distribution, the cuboid geometry of the channels and membrane stack, the low variability in the hydraulic path length and the nature of the velocity gradient in the top and bottom lateral channels, all of which resulted in a significantly narrower RTD. In bind and elute separations, a narrower RTD ensures elution of a component as a tight band, i.e. as a sharp peak, which results in higher resolution when multiple components are being separated. The simulated tracer data showed that with LFMC device, particles collimate into a tight and concentrated fraction at the device outlet. On the other hand, with the stacked disc device the particles get very widely dispersed. On account of the above reasons, the LFMC device gives better resolution in multi-component separation than its equivalent stacked disc device.

# Acknowledgements

We thank the Ontario Research Fund-Research Excellence (ORF-RE) program and the Natural Science and Engineering Research Council (NSERC) of Canada for funding this project.


## Nomenclature

| | |
|---|---|
| $\epsilon$ | Porosity (-) |
| $K_b$ | Permeability ($m^2$) |
| $P$ | Pressure (Pa) |
| $\mu$ | Fluid dynamic viscosity (Pa$\cdot s$) |
| $\rho$ | Fluid density ($kg/m^3$) |
| $\mathbf{I}$ | Identity matrix |
| $\mathbf{u}$ | Fluid velocity field (m/s) |
| $F$ | External Forces (Pa) |
| $f(R)$ | Arbitrary radial distance (m) |
| $L$ | Length of cuboid packed-bed (m) |
| $W$ | RWidth of cuboid packed-bed (m) |
| $h_c$ | Channel/header height (m) |
| $h_b$ | Packed-bed height (m) |
| $Q_{in}$ | Inlet flow rate ($m^3/s$) |
| $D$ | Diffusion coefficient ($m^2/s$) |

# References

Brinkman, H.C., 1949. A calculation of the viscous force exerted by a flowing fluid on a dense swarm of particles. Flow Turbul. Combust. 1, 27. https://doi.org/10.1007/BF02120313

Farkas, T., Chambers, J.Q., Guiochon, G., 1994. Column efficiency and radial homogeneity in liquid chromatography. J. Chromatogr. A 679, 231–245. https://doi.org/10.1016/0021-9673(94)80565-2

Farkas, T., Sepaniak, M.J., Guiochon, G., 1997. Radial distribution of the flow velocity, efficiency and concentration in a wide HPLC column. AIChE J. 43, 1964–1974. https://doi.org/10.1002/aic.690430806

Farkas, T., Sepaniak, M.J., Guiochon, G., 1996. Column radial homogeneity in high-performance liquid chromatography. J. Chromatogr. A 740, 169–181. https://doi.org/10.1016/0021-9673(96)00107-0

Ghosh, P., Vahedipour, K., Lin, M., Vogel, J.H., Haynes, C., von Lieres, E., 2013. Computational fluid dynamic simulation of axial and radial flow membrane chromatography: Mechanisms of non-ideality and validation of the zonal rate model. J. Chromatogr. A 1305, 114–122. https://doi.org/10.1016/j.chroma.2013.07.004

Ghosh, R., 2016. Using a box instead of a column for process chromatography. J. Chromatogr. A 1468, 164–172. https://doi.org/10.1016/j.chroma.2016.09.044

Ghosh, R., Madadkar, P., Wu, Q., 2016. On the workings of laterally-fed membrane chromatography. J. Membr. Sci. 516, 26–32. https://doi.org/10.1016/j.memsci.2016.05.064

Ghosh, R., Wong, T., 2006. Effect of module design on the efficiency of membrane chromatographic separation processes. J. Membr. Sci. 281, 532–540. https://doi.org/10.1016/j.memsci.2006.04.023

Joshi, J.B., Ranade, V.V., 2003. Computational Fluid Dynamics for Designing Process Equipment: Expectations, Current Status, and Path Forward. Ind. Eng. Chem. Res. 42, 1115–1128. https://doi.org/10.1021/ie0206608

Kremer, D.M., Hancock, B.C., 2006. Process Simulation in the Pharmaceutical Industry: A Review of Some Basic Physical Models. J. Pharm. Sci. 95, 517–529. https://doi.org/10.1002/jps.20583

Li, Y.-L., Tung, K.-L., 2008. The effect of curvature of a spacer-filled channel on fluid flow in spiral-wound membrane modules. J. Membr. Sci. 319, 286–297. https://doi.org/10.1016/j.memsci.2008.03.069

Madadkar, P., Ghosh, R., 2016. High-resolution protein separation using a laterally-fed membrane chromatography device. J. Membr. Sci. 499, 126–133. https://doi.org/10.1016/j.memsci.2015.10.041

Madadkar, P., Nino, S.L., Ghosh, R., 2016. High-resolution, preparative purification of PEGylated protein using a laterally-fed membrane chromatography device. J. Chromatogr. B 1035, 1–7. https://doi.org/10.1016/j.jchromb.2016.09.014

Madadkar, P., Umatheva, U., Hale, G., Durocher, Y., Ghosh, R., 2017. Ultrafast Separation and Analysis of Monoclonal Antibody Aggregates Using Membrane Chromatography. Anal. Chem. 89, 4716–4720. https://doi.org/10.1021/acs.analchem.7b00580

Madadkar, P., Wu, Q., Ghosh, R., 2015. A laterally-fed membrane chromatography module. J. Membr. Sci. 487, 173–179. https://doi.org/10.1016/j.memsci.2015.03.056

Marriott, J., Sorensen, E., 2003. A general approach to modelling membrane modules. Chem. Eng. Sci. 58, 4975–4990. https://doi.org/10.1016/j.ces.2003.07.005

Naveen Pathak, Carney Norman, Sourav Kundu, Suresh Nulu, Mark Durst, Zhiwu Fang, 2008. Modeling Flow Distribution in Large-Scale Chromatographic Columns with Computational Fluid Dynamics. BioProcess Int.

Orr, V., Zhong, L., Moo-Young, M., Chou, C.P., 2013. Recent advances in bioprocessing application of membrane chromatography. Biotechnol. Adv. 31, 450–465. https://doi.org/10.1016/ j.biotechadv.2013.01.007 Pordal, H.S., Matice, C.J., Fry, T.J., 2002. The role of computational fluid dynamics in the pharmaceutical industry. Pharm. Technol. 26, 72.

Przybycien, T.M., Pujar, N.S., Steele, L.M., 2004. Alternative bioseparation operations: life beyond packed-bed chromatography. Curr. Opin. Biotechnol. 15, 469–478. https://doi.org/10.1016/j.copbio.2004.08.008

Sadavarte, R., Madadkar, P., Filipe, C.D., Ghosh, R., 2018. Rapid preparative separation of monoclonal antibody charge variants using laterally-fed membrane chromatography. J. Chromatogr. B 1073, 27–33. https://doi.org/10.1016/j.jchromb.2017.12.003

Suen, S.-Y., Liu, Y.-C., Chang, C.-S., 2003. Exploiting immobilized metal affinity membranes for the isolation or purification of therapeutically relevant species. J. Chromatogr. B, Interactions in Biological Systems 797, 305–319. https://doi.org/10.1016/S1570-0232(03)00490-2

Teepakorn, C., Grenier, D., Fiaty, K., Charcosset, C., 2016. Characterization of hydrodynamics in membrane chromatography devices using magnetic resonance imaging and computational fluid dynamics. Chem. Eng. Res. Des. 113, 61–73. https://doi.org/10.1016/j.cherd.2016.06.027

van Reis, R., Zydney, A., 2007. Bioprocess membrane technology. J. Membr. Sci. 297, 16–50. https://doi.org/10.1016/j.memsci.2007.02.045

Yuan, Q.S., Rosenfeld, A., Root, T.W., Klingenberg, D.J., Lightfoot, E.N., 1999. Flow distribution in chromatographic columns1Presented at the 1998 International Symposium on Preparative Chromatography, Ion Exchange and Adsorption/Desorption Processes and Related Techniques, Washington, DC, 31 May–3 June 1998.1. J. Chromatogr. A 831, 149–165. https://doi.org/10.1016/S0021-9673(98)00924-8

# Chapter 3

# An evaluation of a radial flow membrane adsorber and a LFMC device

This mini-chapter is an evaluation of system fluidics between the LFMC device discussed in chapter 2 with another conventionally used membrane chromatography format, the radial flow geometry.

# An evaluation of a radial flow membrane adsorber and a laterally-fed membrane chromatography device

## Introduction

Many commercial biopharmaceutical production practices date back several decades and with these processes, the yield loss during purification of the target molecule is substantial (McRae et al., 2005; Reeve et al., 1985). For feed materials that contain impurities that have similar size, charge, pI, and hydrophobicity as the target molecule, laborious multistep processes are required to obtain the high purity required for clinical applications. Membrane chromatography (MC) is most commonly used as end-stage polishing steps in these purification process (Ghosh and Wong, 2006). Over the last couple of decades, membranes used for membrane chromatography have shown to have higher capture efficiency and higher productivity than column chromatography (Zeng and Ruckenstein, 1999). It is a fast and modularly scalable method and it is widely used to remove viruses, endotoxins, and host cell proteins from biopharmaceutical products; however, the primary drawback this method is it unsuitable for high resolution multi-component separations.

The main factors influencing the resolution of multicomponent-protein separations are (1) relative species interactions with the stationary media (based on size, hydrophobicity, affinity, ion charge, polarity) and (2) residence time distribution (RTD) of each species in the separation system. The target molecule interaction with the stationary media can be optimized with modifications to the pH and conductivity of the feed material, equilibrium and elution buffers in conjunction to the elution strategy (i.e. gradient or step elution), whereas the RTD of molecules is primarily a characteristic of the system fluidics of the chromatography device and desorption rates.

A narrow RTD improves elution peak resolution and consequently allows for the collection of a purer fraction during bind and elute mode operation. Many of the commercial MC device geometries (i.e radial flow, hollow fiber and stack disc) have significant flow deficiencies that make MC unsuitable for high resolution purification, which is more pronounced compared to other medias of separation such as resin-based chromatography as this technique relies heavily on convective mass transport (Ghosh and Wong, 2006). In stack disc absorbers, a stack of membrane sheets is housed within the device, whereas radial flow membrane absorbers contain a spirally wound flat membrane sheet over a porous central core. The primary problem with current MC formats is the differences in the feed and permeates side velocity fields of the devices. It was determined that for solute particles to reach the outlet at the same time, all streamlines need to the same average velocity (Chen et al., 2019; Umatheva et al., 2018). This means that if solute travels along a high-velocity path on the feed side, it needs to travel in a low-velocity path on the permeate side. Likewise, if the solute travels in slow velocity streamlines on the feed side, it will travel along a high-velocity path on the permeate side. There needs to be flow balancing by the device which gives rise to the characteristic crossing velocity magnitudes of the feed and permeate sides as shown in Figure 3.1 (Chen

et al., 2019; Umatheva et al., 2018).

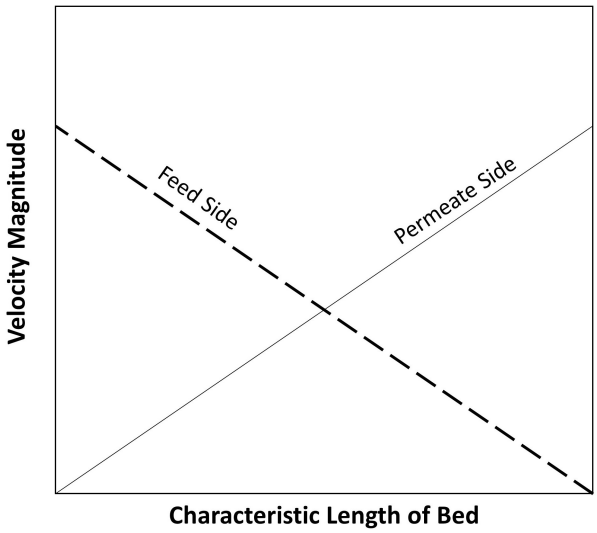


Figure 3.1: Velocity balancing profile of chromatography modules with narrow RTD

Laterally-fed membrane chromatography (LFMC) addresses the fluidic concerns by flow balancing and velocity compensation in the device feeding and collecting channels (Ghosh et al., 2016; Madadkar et al., 2015; Umatheva et al., 2018). This is achieved by a low dead-volume and minimal fluid back-mixing. In previously published papers, the LFMC has demonstrated high-resolution separations of complex multi-component samples such as PEGylated proteins, monoclonal antibody charge variants and adenovirus from infected cell lysates (Kawka et al., 2019; Madadkar et al., 2016). This paper is an examination of the system fluidics of LFMC and an equivalent radial flow membrane chromatography device (Figure 3.2) on quality and resolution of separation.

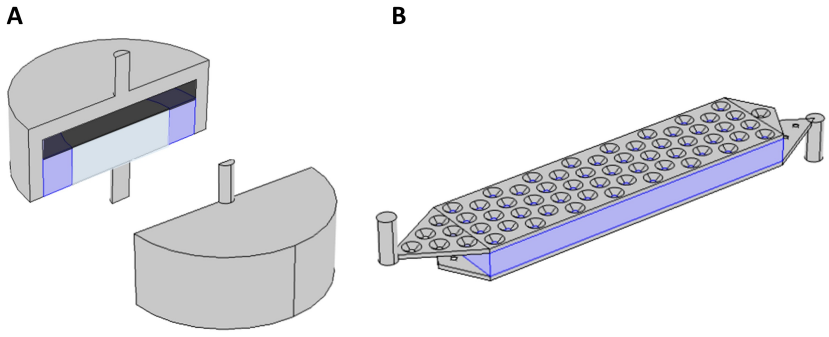


Figure 3.2: A schematic representation of the A) Radial flow device B) LFMC device

# CFD Model Setup

COMSOL Multiphysics 5.4 was used to model the radial flow and LFMC devices. The steady-state model was built using the *Brinkman Equations* physics package to determine the velocity fields that were responsible for the convective mass transport of the molecular species. The dynamic tracing of the NaCl tracer was simulated using the *Transport of Diluted Species in Porous Media* physics package.

The velocity fields within the MC devices are described by a numerical solution for the Navier–Stokes equation, continuity equation, and the Brinkman equations. Brinkman equations are an extension of the Navier–Stokes, and continuity equations to represent flow in porous media (Brinkman, 1949). Mass balances on molecular species were also solved in conjunction. The MC devices used in this work include the 1 mL Sartobind Q Nano capsule (Sartorius, Gottingen, Germany) and LFMC module containing ten sheets of 38 mm × 10 mm Sartobind Q membranes stacked to a bed height of 2.75 mm. Details of the construction of the LFMC module is outlined in (Kawka et al., 2019). The simulation and process parameters used to solve the CFD model are listed in Table 3.1.

Table 3.1: Flow-through simulation parameters

| Parameter | Value | |
|---|---|---|
| $Q_{in}$ | Inlet flow rate ($m^3/s$) | $8.333\times10^{-8}$ |
| $\epsilon$ | Sartobind Q/S media porosity (-) | 0.78 |
| $\epsilon_c$ | Central core porosity (-) | 0.9 |
| $K_b$ | Sartobind Q/S media permeability ($m^2$) | $1.18\times10^{-14}$ |
| $n_Q$ | Moles of Q functional groups ($mol/m^2$) | 0.5 |
| $D_{NaCl}$ | Diffusion coefficient of NaCl in water ($m^2/s$) | 2.9×10-9 |

# Results

The velocity profile within the membrane bed and channels within the LFMC device can be visualized in Figure 3.3. The device has a triangular feeding tapper that extends into the main channel space above the membrane stack. Due to the constant cross-sectional area and constant fluid flux to the bed below, the velocity decreases linearly in the feeding channel (Umatheva et al., 2018).

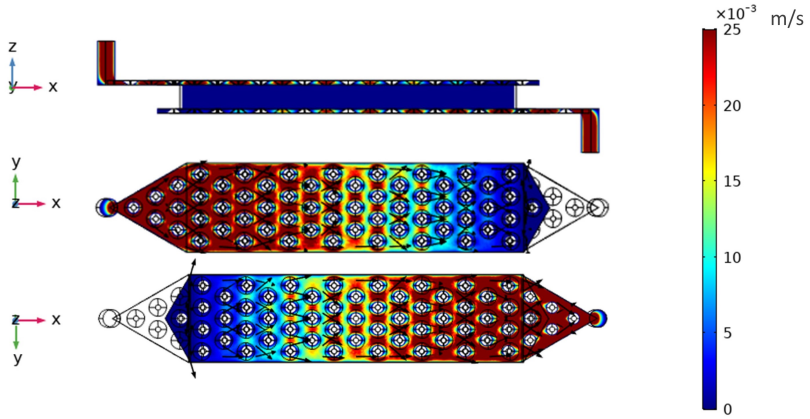


Figure 3.3: Velocity within the flow distributing channels and membrane bed when the volumetric flow rate is 5 mL/min

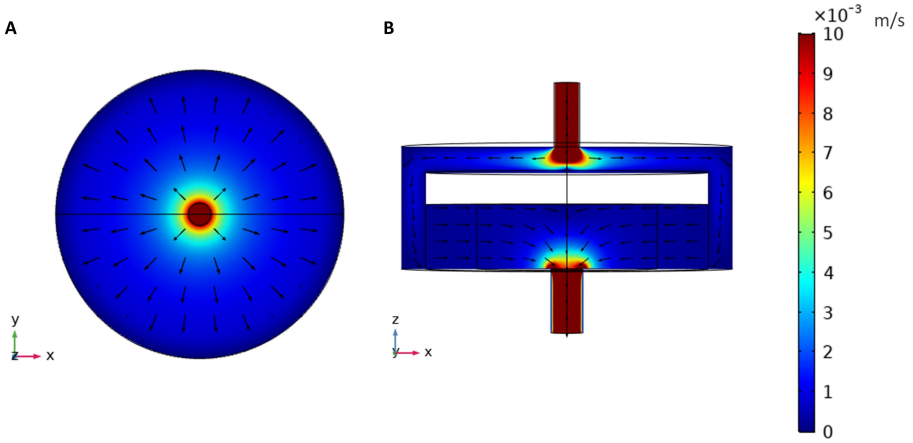


Figure 3.4: Velocity within the radial flow device at volumetric flow rate of 5 mL/min in A) the distributing header B) membrane bed

In the radial flow device, fluid is radially distributed upon entering the module as seen in Figure 3.4. In the studied device, there was a solid plug that was used to guide the fluid to the outer walls of the device and reduced the dead volume of the device. Once the fluid reached the periphery, the velocity magnitude had decreased due to the increase in cross-sectional area (i.e. $V \propto \frac{1}{r}$ ). The characteristic spirally wound membrane within the radial flow module resulted in decreasing membrane cross-sectional area, which would result in an increase in superficial velocity towards the core. In the radial flow device, the central core had a higher void fraction and as a result, considerably low resistance compared to the membrane. The outlet of the device was directly below the central core such that the fluid must flow through the center of the core and since the core was highly porous, fluid field bends towards the outlet.

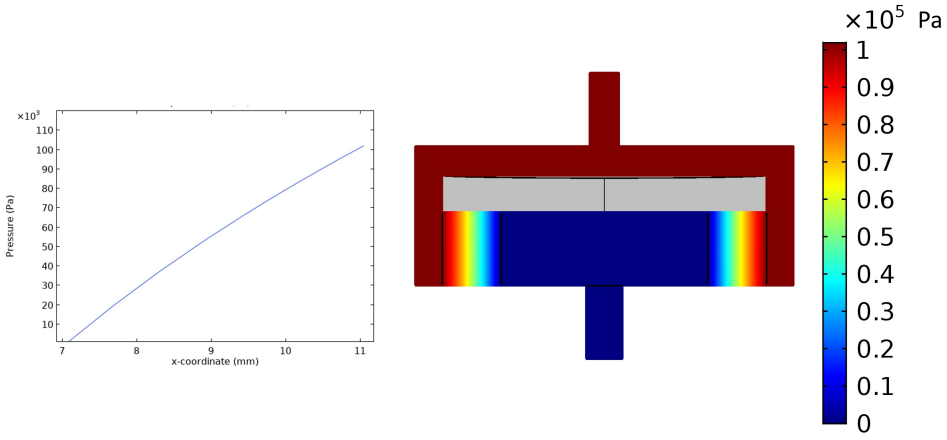


Figure 3.5: Pressure profile with a radial flow device at 5mL/min

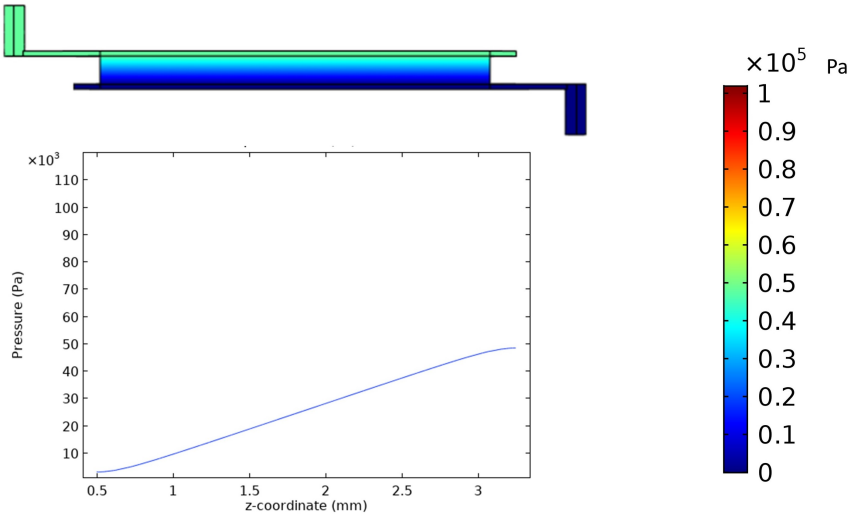


Figure 3.6: Pressure profile with in a LFMC device at 5mL/min

The pressure drops linearly through the membrane bed in both devices, as seen in Figure 3.5A and Figure 3.6A; however, the pressure drop across the bed LFMC device is about half of that of the radial flow device. The higher transmembrane pressure is due to the constant fluid flux and increasing superficial velocity through the bed as a function of radial location, as seen in Eq 3.1. For a bed with a constant permeability, the pressure drop will increase proportionally to the velocity, as seen in Eq 3.2 where $K_b$ is the permeability through the bed, $dh_b$ is the bed thickness and $\mu$ is the dynamic viscosity. $V(r)$, the superficial velocity is a function of radial location. Lower pressure separation is ideally preferred for the purification of biologics since at high pressure there is a risk of product aggregation (Chi et al., 2003; Wang et al., 2010).

$$\begin{aligned} V(r) &= \frac{Q}{A} \\ &= \frac{Q}{\pi D h_b} \\ &= \frac{Q}{2\pi h_b}\left(\frac{1}{r}\right) \end{aligned} \tag{3.1}$$

$$K_b = V(r)\mu\frac{dh_b}{dP} \tag{3.2}$$

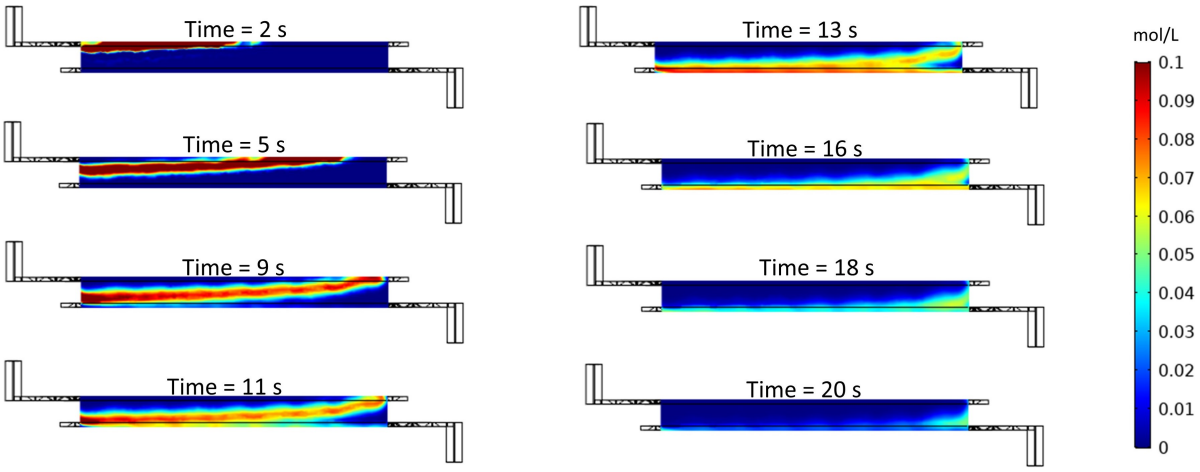


Figure 3.7: Movement of 25 µL of 2M NaCl through the LFMC device at 5 mL/min

Figure 3.7 shows the movement of a high diffusivity tracer molecule, NaCl, through the LFMC device. It can be seen that the solute front enters and propagates through the membrane bed at a slant, which is a characteristic flow pattern of the LFMC device design resulting from linear velocity change in the feeding channel (Umatheva et al., 2018). After the solute has reached the permeate side of the membrane, the solute will converge into a concentrated fraction at the outlet.

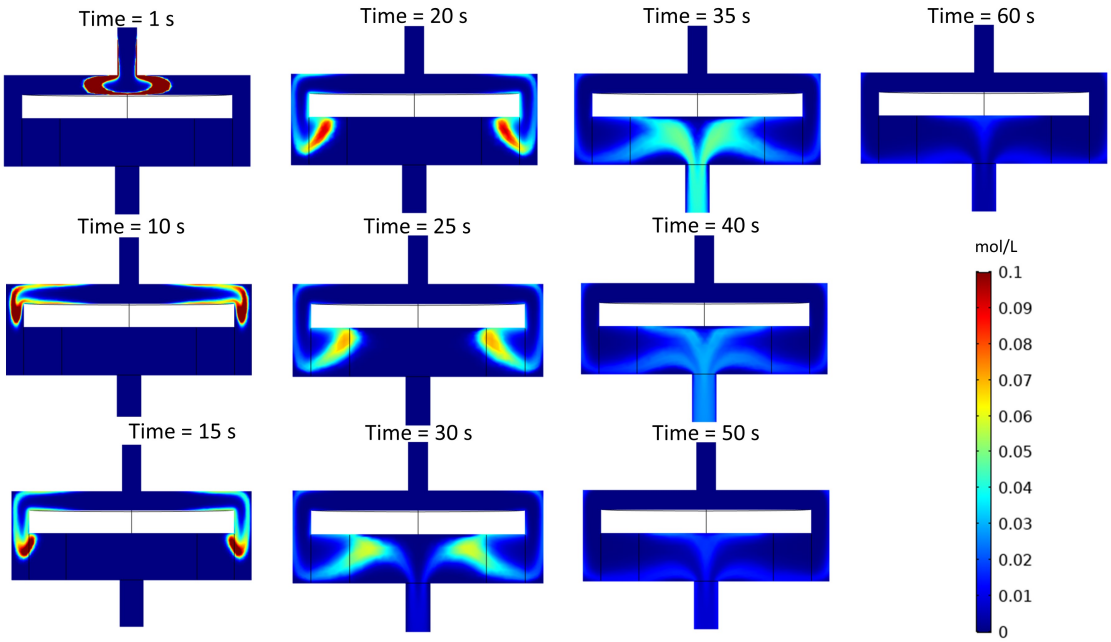


Figure 3.8: Movement of 25 µL of 2M NaCl through the radial flow device at 5 mL/min

Figure 3.8 shows the movement of NaCl through the equivalent radial flow module. It can be seen that by 15s from solute pulse injection, the solute had been diluted, due to the large dead volume in the header, before it reached the membrane bed. The solute enters the bed near the top of the device and will exit the membrane into the porous central core at the top. This region, furthest away from the outlet on the permeate side, corresponds to low-velocity fields as seen in Figure 3.4. Starting from t=50s there is residual solute remaining within the device as it was not cleared out the device by convective mass transport. As a result, the remaining solute will be cleared from the module slowly by diffusion, which could contribute to peak asymmetry and tailing.

Non-binding tracer peaks are shown in Figure 3.9. The radial flow device resulted in a shorter and wider flow-through peak compared to the LFMC device. The NaCl tracer, having high diffusivity, led to peak tailing in both devices; however, it was more pronounced in the radial flow module. Flow-through peak characteristics are tabulated in Table 3.2. The peak asymmetry was calculated with Eq 3.3 where $a$ and $b$ are the distances from the peak midpoint to leading and trailing edges of the peak respectively at 10% of peak height. The tailing factor was calculated using Eq 3.4 where $a$ and $b$ were determined at 5% of the peak height. Peak tailing in chromatographic separation is heavily attributed to different rates of mass transfer kinetics (Fornstedt et al., 1996; Giddings, 1963). With analytes that have high diffusivity or that have slow desorption from to the separation media, there would be longer retention of the solute and thus variability to residence time distribution. The peak tailing observed with the radial flow configuration could be attributed to different mass transfer rates at different locations in the membrane bed, as a result of the velocity profile in the device. In addition,

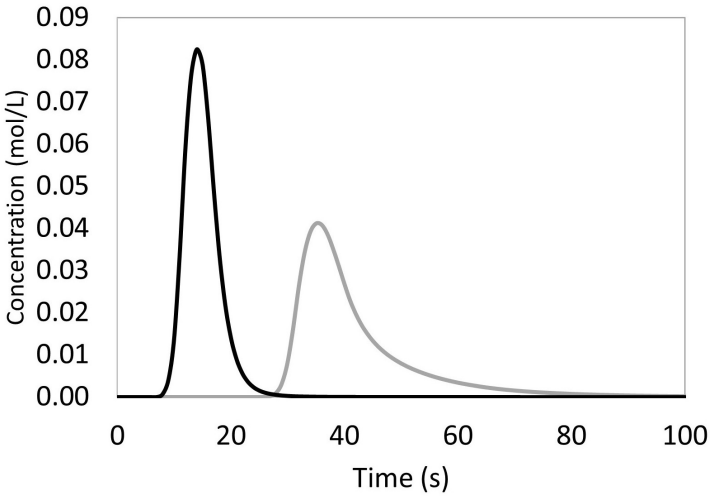


Figure 3.9: Simulated flow-through peaks of 25 uL of 2 M NaCl tracer (black line: LFMC device, grey line: radial flow device)

in the radial flow configuration, the high dead volume on both the feed and permeate side of the membrane cause sample dilution and consequently shallower peaks. The LFMC device design reduces the dead volume in the device and has a more uniform velocity profile (i.e. constant superficial velocity through the bed and balanced velocity pattern by the feed and permeate channels), which reduces the variability of local mass transfer rates within the device. Another contributor to the variability in solute residence time is introduced as some fluid will traverse paths within more porous regions (i.e. the entire height of central core) compared to paths that are in the free fluid space between the wall of the module and the membrane bed. The LFMC device has a narrower flow-through peak and it can be expected to obtain greater recovery of target molecules since narrower peaks imply greater resolution.

$$A_s = \frac{b}{a} \tag{3.3}$$

$$T_f = \frac{a+b}{2a} \tag{3.4}$$

Table 3.2: Peak attributes from simulated flow-through peaks

| | $W_{0.5h}$ (s) | $N(1/m)$ | $A_s$ | $T_f$ |
|---|---|---|---|---|
| Radial Flow | 10.33 | 324 | 3.03 | 2.90 |
| LFMC | 6.21 | 2552 | 1.67 | 1.38 |

# Conclusion

This computational fluid dynamic study identifies key design attributes of the radial flow device that limit its use from intermediate purification processes. An alternative membrane chromatography module, the LFMC device, has an improved design that allows it to be a suitable format for intermediate processing in addition to current MC applications of product polishing steps. The LFMC module results in taller, narrower and more symmetric flow-through peaks compared to the radial flow device. The poorer performance of the radial flow device, as evaluated by peak shape characteristics, was primarily due to the variability in solute residence time introduced by the radial feeding and collecting velocity profile. The number of theoretical plates per unit bed height obtained with the LFMC device was a magnitude higher than the radial flow module, which would suggest better resolution in chromatographic separation.

# References

Brinkman, H.C., 1949. A calculation of the viscous force exerted by a flowing fluid on a dense swarm of particles. Flow Turbul. Combust. 1, 27. https://doi.org/10.1007/BF02120313

Chen, G., Umatheva, U., Alforque, L., Shirataki, H., Ogawa, S., Kato, C., Ghosh, R., 2019. An annular-flow, hollow-fiber membrane chromatography device for fast, high-resolution protein separation at low pressure. J. Membr. Sci. 590, 117305. https://doi.org/10.1016/j.memsci.2019.117305

Chi, E.Y., Krishnan, S., Randolph, T.W., Carpenter, J.F., 2003. Physical Stability of Proteins in Aqueous Solution: Mechanism and Driving Forces in Nonnative Protein Aggregation. Pharm. Res. 20, 1325–1336. https://doi.org/10.1023/A:1025771421906

Fornstedt, T., Zhong, G., Guiochon, G., 1996. Peak tailing and mass transfer kinetics in linear chromatography. J. Chromatogr. A 741, 1–12. https://doi.org/10.1016/0021-9673(96)00152-5

Ghosh, R., Madadkar, P., Wu, Q., 2016. On the workings of laterally-fed membrane chromatography. J. Membr. Sci. 516, 26–32. https://doi.org/10.1016/j.memsci.2016.05.064

Ghosh, R., Wong, T., 2006. Effect of module design on the efficiency of membrane chromatographic separation processes. J. Membr. Sci. 281, 532–540. https://doi.org/10.1016/j.memsci.2006.04.023

Giddings, J.C., 1963. Kinetic Origin of Tailing in Chromatography. Anal. Chem. 35, 1999–2002. https://doi.org/10.1021/ac60206a008

Kawka, K., Madadkar, P., Umatheva, U., Shoaebargh, S., Medina, M.F.C., Lichty, B.D., Ghosh, R., Latulippe, D.R., 2019. Purification of therapeutic adenoviruses using laterally-fed membrane chromatography. J. Membr. Sci. 579, 351–358. https://doi.org/10.1016/j.memsci.2019.02.056

Madadkar, P., Nino, S.L., Ghosh, R., 2016. High-resolution, preparative purification of PEGylated protein using a laterally-fed membrane chromatography device. J. Chromatogr. B 1035, 1–7. https://doi.org/10.1016/j.jchromb.2016.09.014

Madadkar, P., Wu, Q., Ghosh, R., 2015. A laterally-fed membrane chromatography module. J. Membr. Sci. 487, 173–179. https://doi.org/10.1016/j.memsci.2015.03.056

McRae, S.R., Brown, C.L., Bushell, G.R., 2005. Rapid purification of EGFP, EYFP, and ECFP with high yield and purity. Protein Expr. Purif. 41, 121–127. https://doi.org/10.1016/j.pep.2004.12.030

Reeve, J.R., Ho, F.J., Walsh, J.H., Ben-Avram, C.M., Shively, J.E., 1985. Rapid high-yield purification of canine intestinal motilin and its complete sequence determination. J. Chromatogr. A 321, 421–432. https://doi.org/10.1016/S0021-9673(01)90460-1

Umatheva, U., Madadkar, P., Selvaganapathy, P.R., Ghosh, R., 2018. Computational fluid dynamic (CFD) simulation of laterally-fed membrane chromatography. Chem. Eng. Res. Des. https://doi.org/10.1016/j.cherd.2018.07.026

Wang, W., Nema, S., Teagarden, D., 2010. Protein aggregation—Pathways and influencing factors. Int. J. Pharm. 390, 89–99. https://doi.org/10.1016/j.ijpharm.2010.02.025

Zeng, X., Ruckenstein, E., 1999. Membrane Chromatography: Preparation and Applications to Protein Separation. Biotechnol. Prog. 15, 1003–1019. https://doi.org/10.1021/bp990120e

# Chapter 4

# CFD simulations of a cuboid packed-bed device

This chapter compares the traditional packed-bed column with the new packed-bed cuboid design. The cuboid configuration addresses some of the flow non-uniformity observed in the conventional geometry by facilitating flow balancing by the feeding and collecting channels.

In this work, I completed the CFD simulations and was the primary author of the manuscript. All non-binding tracer experiments were conducted by Dr. Guoqiang Chen. Dr. Raja Ghosh supervised the project and edited the manuscript. Revisions for this paper have been submitted to Chemical Engineering Research and Design.

# Computational fluid dynamic (CFD) simulation of a cuboid packed-bed chromatography device

Umatheny Umatheva, Guoqiang Chen, Raja Ghosh*

Department of Chemical Engineering, McMaster University
1280 Main Street West, Hamilton, ON, Canada L8S 4L7

*Corresponding Author
Email: rghosh@mcmaster.ca
Phone: +1 905−525 9140 ext 27415

**Abstract**
Flow non-uniformity is a major problem with process columns which typically have small bed height to diameter ratios. In recent publications, we have proposed box-shaped or cuboid packed-bed devices as efficient alternative to process columns for carrying out high-resolution chromatographic separations. Cuboid packed-bed devices show superior performance in terms of number of theoretical plates, peak width, and peak resolution in multicomponent separations. This paper attempts to explain this based on computational fluid dynamic (CFD) simulations of a cuboid packed-bed device and its equivalent column, i.e. having the same bed height and area of cross-section, and packed with the same chromatographic media. The radial velocity in the column headers decreased very rapidly from the axis to the periphery resulting in significant variation in average velocity along the different flow paths within the column. By contrast, the velocity decreased linearly in the top channel and increased linearly in the bottom channel of a cuboid packed-bed device, resulting in significantly lower variation in the average velocity. Simulated flow-through peaks obtained with the cuboid packed-bed device using dextran as a macromolecular and sodium chloride as a low molecular weight tracer were significantly sharper and more symmetric. Experimental results were in good agreement with those obtained by simulation. Overall, the superior performance of the cuboid packed-bed device could be primarily attributed to the narrower solute residence time distribution resulting from greater flow uniformity.

**Keywords:** Cuboid packed-bed; column; chromatography; computational fluid dynamics; simulation; flow distribution

# Introduction

Column chromatography is the gold standard technique for conducting high-resolution bioseparation (Low et al., 2007; Przybycien et al., 2004; Shukla and Thömmes, 2010). However, the performance of a column could potentially be affected by two major limitations: (1) inhomogeneous resin packing, and (2) non-uniform flow within column (Knox et al., 1976; Lightfoot and Moscariello, 2004; Yuan et al., 1999). Within a typical column, the resin packing density is usually higher closer to the wall of the column and decreases toward the centre (Baur et al., 1988; Moscariello et al., 2001; Tallarek et al., 1998). Additionally, the resins used in bioseparation processes are more compressible compared to resins used in other separation applications. Resin compaction could adversely affect efficiency of separation (Stickel and Fotopoulos, 2001). Therefore, shorter columns are more commonly used. Consequently, in biological separations, radial variations in flow through the column has a more significant effect than axial variations on column performance (Lightfoot and Moscariello, 2004; Roblee et al., 1958; Yuan et al., 1999).

The cylindrical geometry of a column requires radial flow distribution of the feed in the top header and radial collection of effluent in the bottom header (Eon, 1978; Farkas et al., 1996; Knox et al., 1976). This is the primary reason for flow non-uniformity in columns having high diameter to bed height ratios (Farkas et al., 1996; Knox et al., 1976; Yuan et al., 1999). The cylindrical geometry of the column implies that the fluid flow paths closer to the column periphery are significantly longer than those closer to the axis. In short columns, the local separation efficiency, as indicated by the height equivalent to a theoretical plate (or HETP), is higher at the centre of the column compared to regions nearer the wall (Baur et al., 1988; Eon, 1978; Farkas et al., 1997, 1996; Knox et al., 1976; Moscariello et al., 2001; Tallarek et al., 1998). Attempts to minimize flow non-uniformity within columns have been focused on improvements in header design (Camenzuli et al., 2011; Shalliker and Ritchie, 2014; Vangelooven et al., 2010). Yuan et al. (Yuan et al., 1999) have identified two criteria for an ideal header: (1) flat velocity profile at the exit of the header, and (2) identical residence time for all streamlines. These are very difficult to achieve in short columns having relatively large diameters.

In our group, we have attempted to address the problem of flow non-uniformity in chromatography devices by designing and developing box-shaped or cuboid packed-bed devices (Chen et al., 2018; Chen and Ghosh, 2018; Ghosh, 2016; Ghosh and Chen, 2017). The design features of these devices were adopted and adapted from laterally- fed membrane chromatography (or LFMC) modules, also developed in our research group over the past few years (Ghosh et al., 2016; Madadkar et al., 2017, 2016, 2015; Madadkar and Ghosh, 2016; Sadavarte et al., 2018). Schematic diagrams of a column and a cuboid packed-bed with idealized flow paths within these are shown in Figure 4.1. In the latter, the feed enters the device from one side and is distributed along the top lateral channel, from where it penetrates the cuboid resin bed at various locations, flows through it, and collects in the bottom lateral channel on the other side. The collected fluid then exits the device from the opposite end, relative to the inlet. Our earlier studies (Chen et al., 2018; Chen and Ghosh,

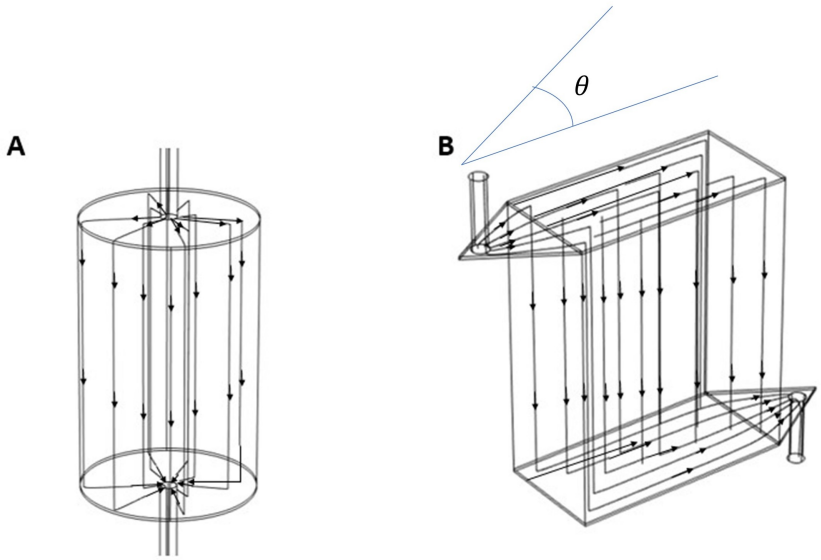


Figure 4.1: Idealized fluid flow paths in a A) column, and B) cuboid packed-bed device.

2018; Ghosh, 2016; Ghosh and Chen, 2017) have demonstrated that cuboid packed-bed devices outperformed equivalent columns (i.e. having the same bed-height, area of cross-section, and packed with same resin) in terms of experimentally measurable performance efficiency metrics such as the number of theoretical plates, peak attributes such as width and symmetry, and resolution in multi-protein separation. We feel that the cuboid packed-bed device has significant potential for application in biopharmaceutical purification processes and its fluidics should be carefully studied. This paper examines the hydrodynamics differences between columns and cuboid packed-beds based on computational fluid dynamics (CFD). Using this, we attempt to explain the reasons for the superior separation attributes observed with cuboid packed-bed devices. The results of the CFD simulations are validated by comparison with experimental results.

# CFD Model Setup

COMSOL Multiphysics 5.4 was used to model the column and cuboid packed-bed device. The steady-state model was built using the *Brinkman Equations* physics package and the residence time and tracer studies were conducted using *Transport of Diluted Species in Porous Media* physics package. The CFD models were solved using the finite element method (FEM) at mesh nodes using iterative solvers.

## Fluid Flow

The CFD models used to describe the fluid flow within the column and the cuboid packed-bed device are based on numerical solution of the Navier–Stokes equation (Eq 4.1), and the Brinkman equation (Eq 4.2). The Brinkman equation is an extension of the Navier–Stokes equation for use in porous media (Brinkman, 1949). The Navier-Stokes equation could be simplified (Eq 4.1b), in these models, since the fluid flowing within the column and the

cuboid packed-bed was incompressible. The Navier-Stokes and Brinkman equations are typically solved together with the continuity equation (Eq 4.3), more specifically using Eq 4.3b (for incompressible fluids). In the overall scheme, the conservation of momentum is represented by the Navier-Stokes equation and the Brinkman equation, while the conservation of mass is represented by the continuity equation.

$$\rho\left(\frac{\partial u}{\partial t} + u \cdot \nabla u\right) = \nabla P + \nabla \cdot (\mu(\nabla u + (\nabla u)^T) - \frac{2}{3}\mu(\nabla u)) + F \tag{4.1a}$$

$$\rho\left(\frac{\partial u}{\partial t} + u \cdot \nabla u\right) = \nabla P + \nabla \cdot (\mu(\nabla u + (\nabla u)^T)) + F \tag{4.1b}$$

$$\frac{\rho}{\epsilon}\left(\frac{\partial u}{\partial t} + (\nabla u)\frac{u}{\epsilon}\right) = -\nabla P + \nabla \cdot \left(\frac{1}{\epsilon}(\mu(\nabla u + (\nabla u)^T))\right) + \left(\frac{\mu}{K_b} + Q_{in}\right) u \tag{4.2}$$

$$\frac{\partial \rho}{\partial t} + \nabla \cdot (\rho u) = 0 \tag{4.3a}$$

$$\nabla \cdot u = 0 \tag{4.3b}$$

The key device and process inputs used to solve the CFD models (listed in Table 4.1) were obtained from an experimental study (Ghosh and Chen, 2017). The primary purpose for selecting these specific inputs was to be able to compare simulated and experimental data, and thereby achieve model validation.

Table 4.1: Device and process inputs used in the CFD simulation (Ghosh and Chen, 2017).

| Parameter | Value | |
|---|---|---|
| $L$ | Length of cuboid packed-bed (m) | 0.02 |
| $W$ | Width of cuboid packed-bed (m) | 0.01 |
| $R$ | Radius of column (m) | $7.979\times10^{-3}$ |
| $h_c$ | Channel/header height (m) | $2.5\times10^{-4}$ |
| $h_b$ | Packed-bed height (m) | 0.025 |
| $t$ | Taper length of cuboid device (m) | $8.0\times10^{-3}$ |
| $\theta$ | Taper angle | $32^o$ |
| $Q_{in}$ | Inlet flow rate ($m^3/s$) | $8.333\times10^{-8}$ |
| $\epsilon$ | Capto Q/S media porosity (-) | 0.37 |
| $Kb$ | Capto Q/S media permeability ($m^2$) | $1.296\times10^{-12}$ |
| $T$ | Temperature (K) | 298.15 |
| $D_{Dextran}$ | Diffusion coefficient of Blue Dextran in water ($m^2/s$) | $2.3\times10^{-11}$ |
| $D_{NaCl}$ | Diffusion coefficient of NaCl in water ($m^2/s$) | $2.9\times10^{-9}$ |

### Solute Tracking and Residence Time Distribution

Tracer tracking and residence time distribution (RTD) study were carried out using the *Transport of Diluted Species in Porous Media* physics package. In this study, small volume of NaCl or blue dextran (2000 kDa) tracer was introduced in the flow going into the device via a rectangular function, starting at time = 0 at the inlet of the device. The movement of the tracer solutes were tracked through each of these separation devices. The velocity field was calculated at steady state and was used to determine the convective transport of the solute in these devices.

## Experimental

Sodium chloride (SOD002.205) was purchased from Bioshop (Burlington, ON, Canada). Blue dextran (MW: 2000 kDa, D5751) was purchased from Sigma Chemicals, Oakville, ON, Canada. Ultrapure water was obtained from a SIMPLICITY 185 water purification unit (Millipore, Molsheim, France). Sodium chloride solutions (0.4 M and 0.8 M) were prepared and utilized as mobile phase and tracer respectively. These solutions were micro-filtered and degassed prior to use. HiTrap Capto Q strong anion exchange column (bed volume: 5 mL, diameter: 16 mm, bed height: 25 mm, 11-0013-03) and strong anion exchange Capto Q media (17-5316-03) were purchased from GE Healthcare Biosciences, QC, Canada. The 5 mL cuboid packed-bed device was designed and fabricated in-house [22]. The dimensions of the packed-bed were 20 mm length, 10 mm width, and 25 mm height. More details, including detailed device design, media packing methods, and performance assessment in terms of efficiency metrics can be found in our previous papers (Chen et al., 2018; Chen and Ghosh, 2018; Ghosh, 2016; Ghosh and Chen, 2017).

The device being tested, i.e. cuboid packed-bed or column, was connected to an AKTA Prime Plus liquid chromatography system (GE Healthcare Biosciences, QC, Canada). The blue dextran peaks were obtained by (1) equilibration of the column or the cuboid packed-bed device using 20 mM Tris-HCl + 1 M NaCl (pH 8), (2) injection of appropriate volume blue dextran solution, and (3) monitoring and recording of UV absorbance at 280 nm wavelength as the peaks emerge from these devices. The experimental procedure for obtaining salt peaks consisted of: (1) equilibration of the system with 0.4 M NaCl solution at an appropriate flow rate until the conductivity baseline was stable, (2) injecting of tracer (0.8 M NaCl solution) into the system, and (3) monitoring and recording of conductivity as the salt peaks emerge from these devices. A 100 µL loop (2% of bed volume) was used for salt tracer injection. Retention time ($t_R$) and peak width at half height ($w_{0.5}$) of the salt peaks were determined and the number of theoretical plates (N) was determined using the following equation:

$$N = 5.545 \left( \frac{t_R}{w_{0.5}} \right)^2 \tag{4.4}$$

# Results and Discussion

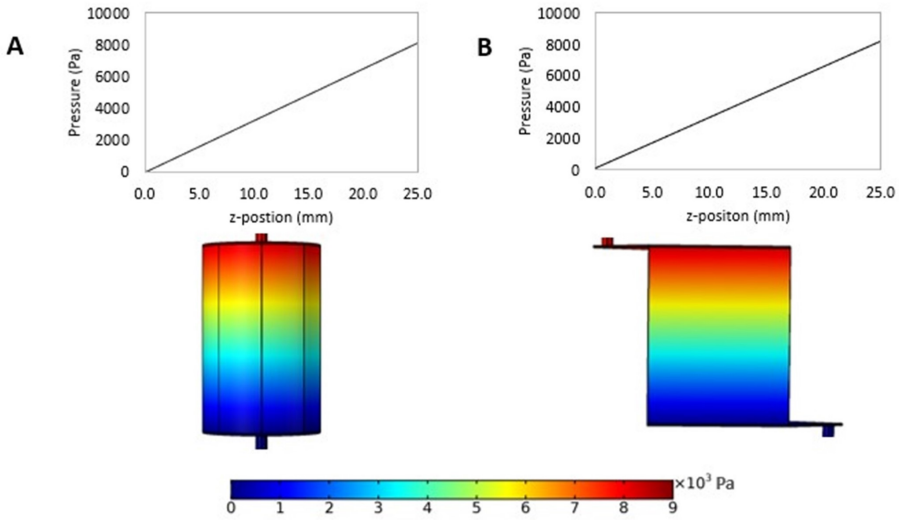


Figure 4.2: Pressure in the resin-beds housed of A) the column and B) the cuboid packed-bed device.

Figure 4.2 shows the pressure distribution in the resin-beds housed within the column and the cuboid packed-bed device. For both devices, the pressure changed uniformly and linearly in the direction of flow. With low resistance (or high permeability) media such as Capto S/Q packed in a relatively small device (5 mL), resin packing could be expected to be largely homogeneous and therefore inhomogeneity was not factored in the CFD model. The pressure drop observed during equivalent chromatographic experiments carried out with the column and cuboid packed-bed devices using the same AKTA Prime liquid chromatography system in the current study varied in the 20-30 kPa range. However, this experimental pressure data included in addition to the pressure drop across the resin-beds, the pressure drops associated with the tubing, fittings, connectors, and the UV and conductivity monitors of the AKTA system. A blank experiment (i.e. without the chromatographic device attached) carried out using the AKTA Prime system at a flow rate of $8.333 \times 10^{-8}$ $m^3/s$ showed the system pressure to be about 10-15 kPa. Therefore, the pressure drop across the resin-beds housed within the column and the cuboid packed-bed device obtained by CFD simulation (i.e. 8.1 kPa) seems reasonable. The pressure data shown in Figure 4.2 would indicate that for both devices, the superficial (or linear) velocity in the resin bed housed within both devices would be uniform, i.e. independent of location. Therefore, by elimination, any difference in RTD between the two devices would have to be attribute to the difference if flow behavior outside the resin bed, i.e. in the column headers and in the channels present in the cuboid packed-bed device.

A solute molecule travelling closer to the axis of a column would have a shorter flow path

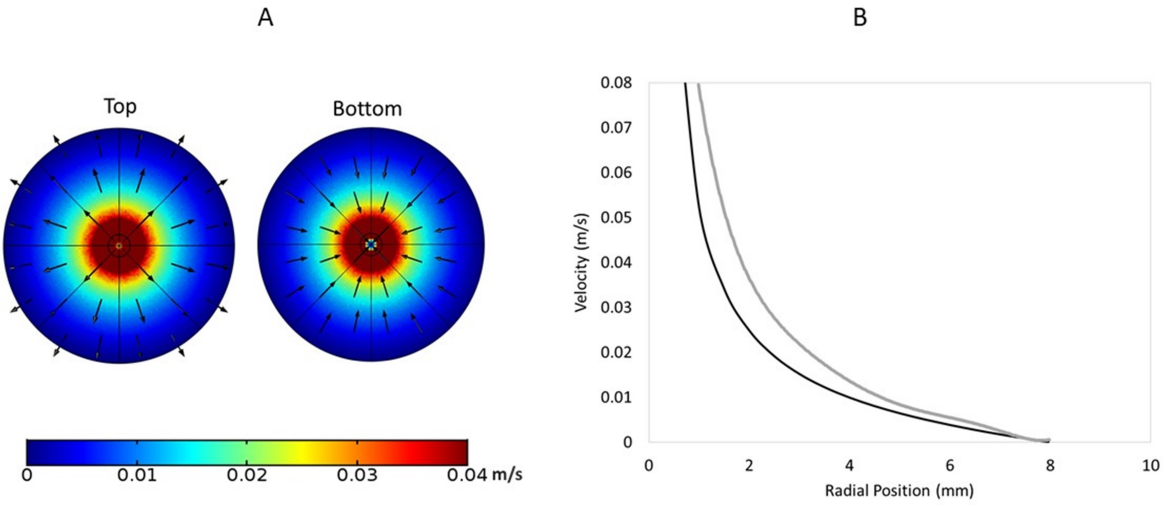


Figure 4.3: A) Velocity profiles in the column headers (volumetric flow rate = 5 mL/min). B) Magnitude of radial velocity as function of radial position in the column headers (Grey line: CFD simulation, black line: mathematical model (Ghosh et al., 2016; Ghosh and Chen, 2017)).

compared to that travelling closer to the periphery. This is due to a shorter distance travelled within the header (see Figure 4.1A). The length of any flow path through the column could be expressed as $2h_c+h_b+2r$ where $h_c$ is the height of the column header, $h_b$ is the bed height and $r$ is the radial location of the flow path. Based on this, the minimum flow path length in a column is $2h_c+h_b$, i.e. when $r = 0$, and the maximum flow path length is $2h_c+h_b+2R$, i.e. at the periphery ($r = R$), $R$ being the column radius. For process columns, where the radius is comparable to the bed height, this difference in path length could be quite significant. In the 5 mL column simulated in this study, the maximum difference in flow path length was 15.96 mm. Any solute molecule flowing through a cuboid packed-bed device needs to traverse its full length during its transit (see Figure 4.1B). For instance, a solute molecule could travel entirely along the top or the bottom channels, or partly along the top and the bottom channels. As can be seen from Figure 4.1B, all the flow paths within the cuboid packed-bed device are fairly similar in length. If the tapering at the inlet and the outlet of the lateral channels were factored in, the longest flow path length within the cuboid packed-bed device could be written as $2h_c+h_b+L+2(t/cos\theta)$, where $L$ is the length of the packed-bed, $t$ is the taper length and $\theta$ is the taper angle (see Figure 4.1A). Therefore, the difference between the maximum and minimum flow path lengths would be equal to $2t((1/cos\theta)-1)$, i.e. it would depend on the taper length and the taper angle. For the 5 mL cuboid packed-bed device simulated in this study, the maximum difference in flow path length was only 2.87 mm.

One of the advantages of CFD modelling is that it allows computation and visualization of local velocity profiles. In both devices, the fluid moved uniformly through the resin-bed, in

a laminar fashion, without any channeling, at uniform superficial (or linear) velocity. Figure 4.3A, shows the velocities in the top and bottom column headers. The magnitude of velocity at corresponding radial locations in the two headers were identical with the direction of flow being opposite, i.e. outward in the top header and inward in the bottom header. Figure 4.3B shows the radial velocity profiles in the column headers obtained by CFD simulation as well by using the first principle based mathematical model discussed in our previous papers (Ghosh et al., 2016; Ghosh and Chen, 2017). As can be seen from both sets of data, the radial velocity was higher closer to the centre and decreased very drastically towards the periphery. The velocity profiles obtained by CFD were in excellent agreement with those obtained using the mathematical model (Ghosh, 2016). The outward decrease in radial velocity in the top header could be attributed to the increase in available cross-sectional flow area, as well as due to the continual ingress of liquid into the resin-bed. Conversely, the inward increase in radial velocity in the bottom header was due to the decrease the in flow area coupled with cumulative collection of fluid from the resin-bed. Such change in the radial velocity in the headers has been identified as being the principal cause of significant variability in the RTD within a column (Ghosh and Chen, 2017; Umatheva et al., 2018).

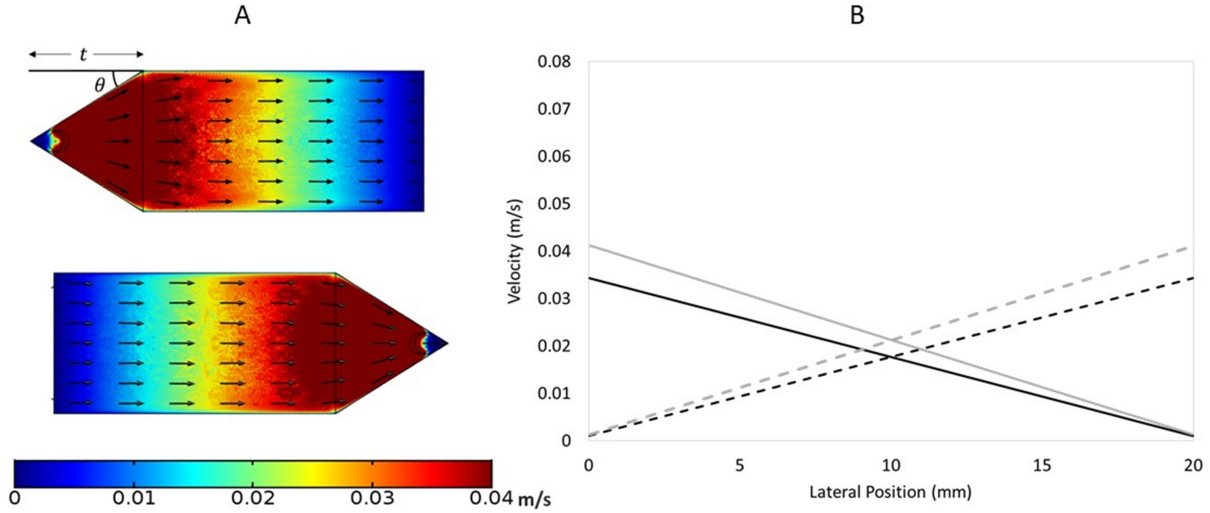


Figure 4.4: A) Velocity profiles in the lateral channels of the cuboid packed-bed device (volumetric flow rate = 5 mL/min). B) Magnitude of velocity in lateral channels of the cuboid packed-bed device (grey lines: CFD, black lines: mathematical model (Ghosh et al., 2016; Ghosh and Chen, 2017), solid lines: top channel, dashed lines: bottom channel).

Figure 4.4A shows the velocities in the top and bottom lateral channels of the cuboid packed-bed device. Figure 4.4B shows the calculated average velocity corresponding to the different lateral locations in the top and bottom channels. Figure 4.4B also shows the lateral velocity data obtained using the first principle based mathematical model discussed in our previous papers (Ghosh et al., 2016; Ghosh and Chen, 2017). In the top channel, the velocity decreased in a linear manner from the inlet side to the outlet side, while in the bottom channel, the velocity increased in a linear fashion from the inlet side to the outlet side. The magnitude of the rate of change in velocity in the two channels were identical, with the signs being opposite. The channel velocity profiles obtained by CFD were consistent with those obtained using the mathematical model (Ghosh, 2016; Ghosh and Chen, 2017). This complimentary nature of change in velocity in the two lateral channels contributes in a significant way towards the narrowing of the RTD within the cuboid packed-bed device.

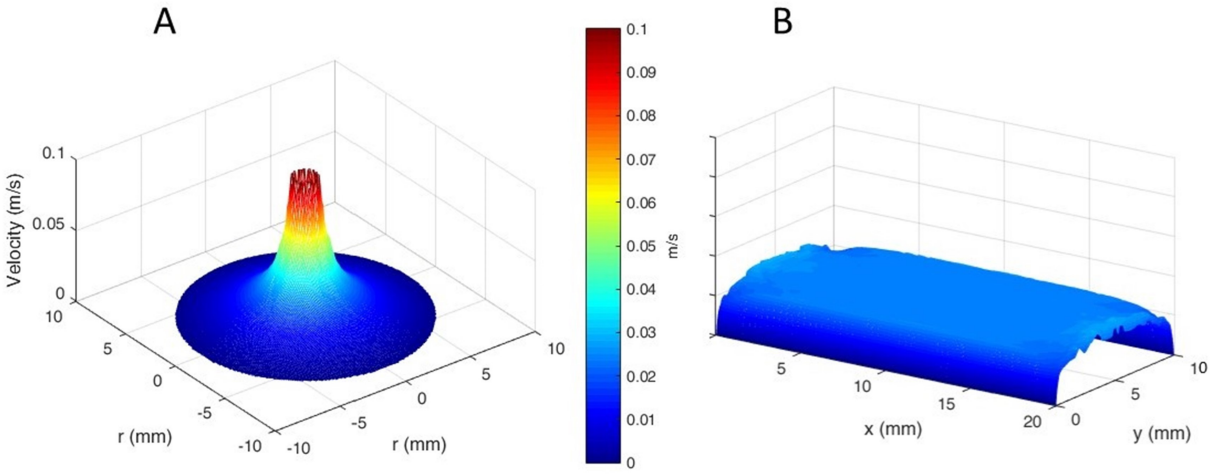


Figure 4.5: Average velocity (volumetric flow rate = 5 mL/min) A) column header B) cuboid channel.

Figure 4.5A shows the overall average header velocity (taking into consideration path lengths traversed in both headers) for flow paths corresponding to different radial locations in the column. The data clearly indicates that there was more than an order of magnitude difference in overall average velocity between flow paths travelling closer to the centre and those travelling closer to the periphery. The reason for this is that the velocity decrease in the top header was further exacerbated in the bottom header, i.e. flow paths traversing closer to the periphery faced a double hinderance in terms of decrease in average velocity. Figure 4.5B shows the overall average channel velocity (taking into consideration path lengths traversed in both top and bottom channel) for flow paths corresponding to different lateral locations in the cuboid packed-bed device. While the overall average velocity in the channel component of the path length did vary to some extent along the width of the channel, i.e. the velocity on the sides of the channel was lower than in the rest of the channel, it was significantly

more uniform than in the column header. The main reason for this is that in the cuboid packed-bed device, the decrease in velocity along a given flow path in the top channel due to the linear drop in channel velocity is compensated by the linear increase in velocity along the portion of the flow path traversed in the bottom channels. In our previous study (Ghosh and Chen, 2017) it was shown that the maximum average velocity in the lateral channels corresponded to the flow path travelling down the middle of the cuboid packed-bed, i.e. travelling half the distance along the top channel and half the distance along the bottom channel. The minimum average velocity in the lateral channels corresponded to the flow path travelling entirely along the edge of the top or the bottom channel (Ghosh and Chen, 2017).

The results of CFD simulation discussed in the preceding paragraphs showed that there is a significant difference in flow behavior between the two devices, i.e. the flow in the cuboid packed-bed device was more uniform. Based on this, it could be predicted that the RTD within the cuboid packed-bed device would be narrower than that in the column. Therefore, sharper flow-through and eluted peaks could be expected when using the cuboid packed-bed device. However, the above analysis is based purely on the differences in path lengths and the theoretical velocities along these, and do not take into consideration the so-called wall effects (Atmakidis and Kenig, 2009; Shalliker et al., 2000) which are known to influence the manner in which solute and solvent molecules are transported within any packed-bed system. To factor in these effects, CFD simulations were carried out to track the movement of tracer solutes within the column and the cuboid packed-bed.

Figures 4.6A and 4.6B show the movement of a 10 µL blue dextran (MW = 2000 kDa, conc. $= 5 \times 10^{-6}$M) tracer pulse, at different times during its transit through the column. As the solute band moved though the bed, there was some broadening in the axial direction due to convective dispersion at the inlet (due to flow within the top header), as well as due to diffusion. There was a noticeable upward flection of the tracer solute near the peripheral regions of the column as it moved though the resin-bed. Also, the outlet of a column is located along the column axis. Therefore, solute molecules moving closer to the axis spend significantly lower amount of time in the lower header when compared to those moving along the periphery. Consequently, the solute molecules travelling closer to the axis exited the column much earlier than those traveling through the periphery. The impact of this phenomenon on column performance could be expected to be quite significant because 50% of the chromatographic resin is located in the outer 29% of the column.

Figures 4.7A and 4.7B show the movement of a 10 µL blue dextran (MW = 2000 kDa, conc. $= 5 \times 10^{-6}$ M) pulse tracer pulse during its transit in the cuboid packed-bed device. The mobile phase considered in this simulation was water. Due to the lateral flow distribution and consequent linear velocity changes in the top channel, the tracer front has a slight backward tilt and an upward flection at the leading end. As the solute band reached the bottom of the packed-bed, the geometry of this device ensured that the slightly backward tilted solute band was collimated at the outlet resulting in the effluent solute molecules being concentrated into a tight fraction. It could therefore be anticipated that the difference in time spent by the

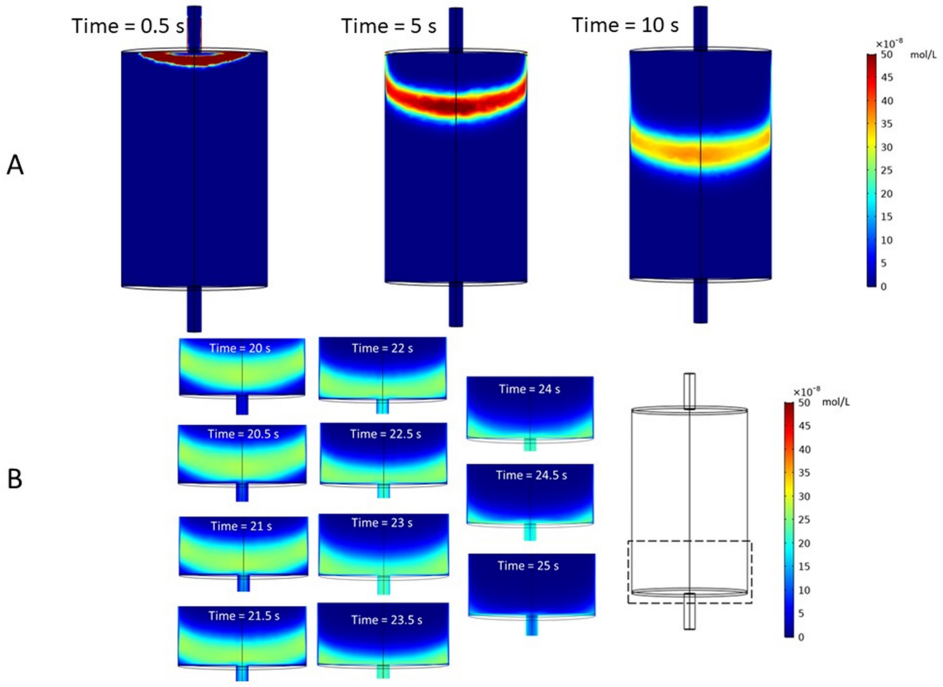


Figure 4.6: Movement of dextran (high molecular weight tracer) through a packed-bed column showing A) solute front B) solute collection at the outlet.

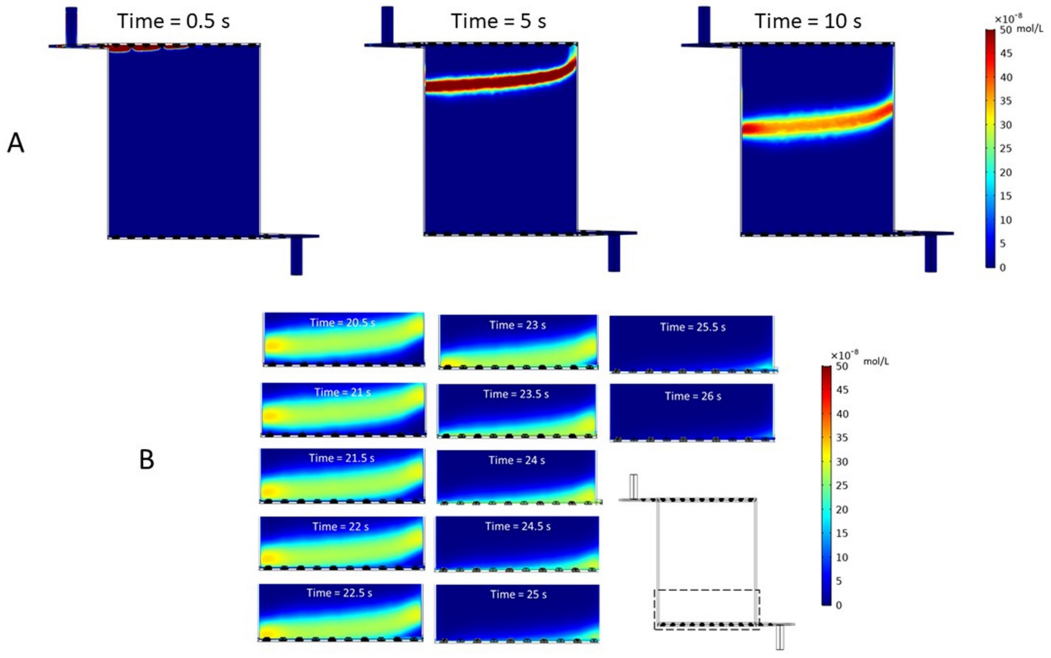


Figure 4.7: Movement of blue dextran tracer through a packed-bed cuboid showing A) solute front B) solute collection at the outlet.

fastest and the slowest blue dextran molecules within the cuboid packed-bed device. Would be significantly lower than that in the column. In our previous papers (Ghosh, 2016; Ghosh and Chen, 2017), our primary reasoning for the superior separation attributes of the cuboid packed-bed device was that species travelling through it had a narrower RTD than in its equivalent column. In chromatographic separation, a narrower RTD implies sharper flow-through and eluted peaks, which consequently result in purer product fractions and greater recovery of product in these fractions (Madadkar et al., 2016; Moscariello et al., 2001).

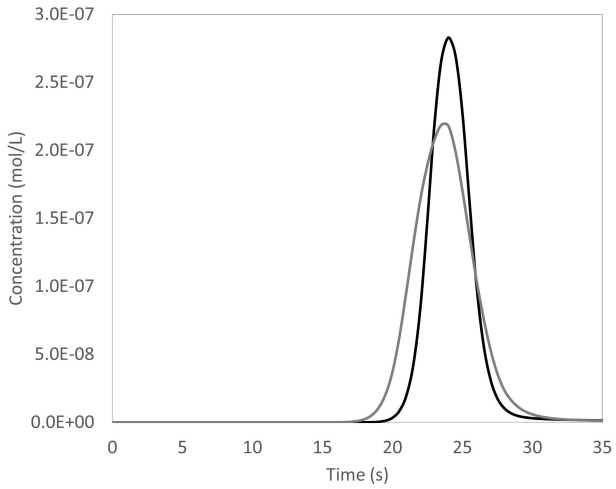


Figure 4.8: Simulated flow-through tracer peak obtained using the cuboid packed-bed device and the column (media: Capto S/Q resin, bed volume: 5 mL, flow rate: 5 mL/min, loop: 10 L, load: $5 \times 10^{-6}$ M blue dextran solution), thin line: column, thick line: cuboid packed-bed).

Figure 4.8 shows the simulated blue dextran (2000 kDa) flow-through peaks obtained for the 5 mL cuboid packed-bed device and the column at 5 mL/min flow rate. The volume of blue dextran solution injected was 10 L, the concentration being $5 \times 10^{-6}$ M, and the mobile phase being water. Consistent with the CFD results discussed in the previous paragraphs, the simulated blue dextran flow-through peak obtained with the cuboid packed-bed device was significantly sharper and narrower than that obtained with the column. Figure 4.9 show the blue dextran flow-through peaks obtained by carrying out experiments using the cuboid packed-bed device and the column. Two sets of experiments were carried out at the same flow rate, i.e. 5 mL/min and same mobile phase, i.e. 20 mM Tris-HCl + 1 M NaCl (pH 8.0). The sodium chloride was added to the mobile phase to inhibit any ionic interaction between the Capto Q anion exchange resin and blue dextran. Incidentally, blue dextran was found to bind weakly with the resin at low salt concentration. Figure 4.9A shows the results obtained by injecting 100 L of 2000 kDa blue dextran (concentration = $5 \times 10^{-6}$ M), while Figure 4.9B shows results obtained by injecting 10 L loop of the same solution. The peaks obtained with the cuboid packed-bed device were shaper and narrower than those obtained with the column and were consistent with those obtained by CFD simulation (see Figure 4.8).

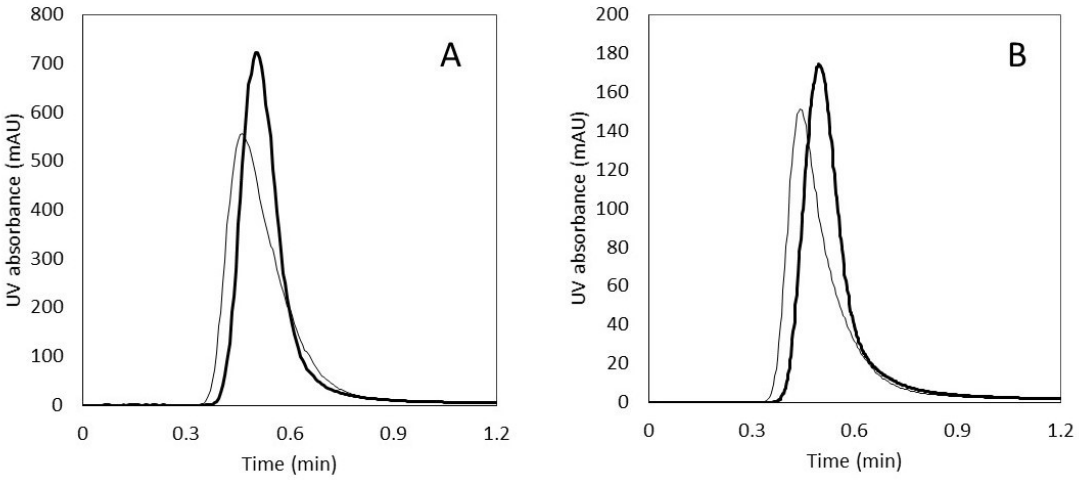


Figure 4.9: Experimental flow-through blue dextran peak obtained using the cuboid packed-bed device and the column (media: Capto Q resin; bed volume: 5 mL; flow rate: 5 mL/min; A: 100 L loop; B: 10 L loop, mobile phase: 20 mM Tris-HCl, 1 M NaCl, pH 8; tracer: $5 \times 10^{-6}$ M, 2000 kDa blue dextran; grey line: column, black line: cuboid packed-bed)

Figure 4.10A shows the simulated flow-through peaks obtained with salt tracer using the cuboid packed-bed device and the column. The simulated tracer used was 100 µL of 0.4 M NaCl solution, and the mobile phase was water. Consistent with the simulated blue dextran tracer peaks shown in Figure 4.8, the salt peak obtained with the cuboid packed-bed device was significantly sharper and narrower than that obtained with the column. Based on these results, it could be concluded that the cuboid packed-bed device would give superior separation performance than its equivalent column for separation of both small and large molecules. Figure 4.10B show the salt flow-through peaks obtained by carrying out experiments using the cuboid packed-bed device and the column, at a flow rate of 5 mL/min, using 0.4 M NaCl as mobile phase, and 10 L of 0.8 M NaCl solution as the tracer. These results are the direct experimental equivalents of the salt tracer simulation results shown in Figure 4.10A. Consistent with the simulation results, the salt peaks obtained using the cuboid packed-bed device were shaper and narrower than those obtained with the column, this being consistent with results obtained by CFD simulation (see Figure 4.8). However, the actual retention times of the peaks obtained by carrying out the salt tracer experiments were greater than those of the simulated salt peaks. Also, the width of the experimental salt peaks was greater than those obtained by the CFD simulation. The primary reason for this is that the Capto Q resin used in the experiments was porous in nature. In the CFD simulations, the resin particles were assumed to be solid spheres and do not allow for pore diffusion of solutes . However, sodium chloride being a small and diffusible molecule would have easy access to the pores present in the Capto Q media, and this would increase its retention time in the column and the cuboid packed-bed device. Pore diffusion would also lead to broadening of the salt peaks as observed in the chromatograms obtained by experiments. The closeness of

the simulated and experimental blue dextran retention times was due to the fact that this 2000 kDa blue dextran being very large molecule, did not have access to the pores present in the Capto Q media.

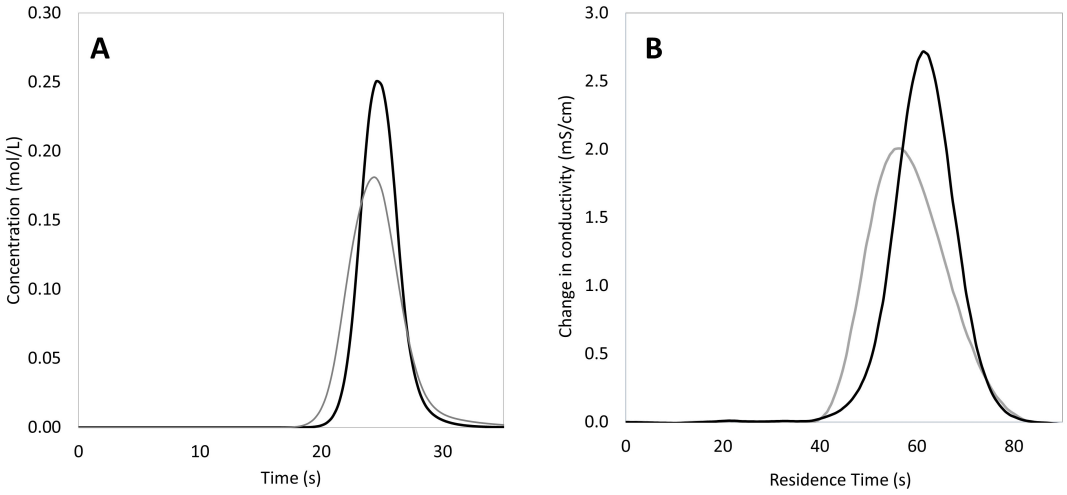


Figure 4.10: Flow-through salt peak obtained using the cuboid packed-bed device and the column (media: Capto Q resin, bed volume: 5 mL, flow rate: 5 mL/min, loop: 100 L, mobile phase: 0.4 M NaCl solution, tracer: 0.8 M NaCl solution ), grey line: column, black line: cuboid packed-bed) A) CFD Simulated B) Experimental.

The peak attributes of simulated and experimental flow-through sodium chloride peaks obtained with the cuboid packed-bed device and its equivalent column are found in Table 4.2 . In both sets of data, the width at half height and the variance of the salt peak obtained with the cuboid packed-bed device were consistently lower than that obtained using the column. Also, the number of theoretical plates in the cuboid packed-bed device, calculated based on the simulated and the experimental peaks was significantly higher. These results confirm the superior separation efficiency of the cuboid packed-bed device when compared to the column. Future studies will focus on simulation of eluted protein peaks to further examine the differences in performance between a cuboid packed-bed device and its equivalent column.

Table 4.2: Peak attributes of flow-through peaks in the cuboid packed-bed device and its equivalent column Simulation - flow rate of 5 mL/min, packed-bed: 5 mL, loop: 100 L, tracer: 0.4 M NaCl. Experimental - flow rate of 5 mL/min, resin: anion exchange Capto Q, packed-bed: 5 mL, loop: 100 L, mobile phase: 0.4 M NaCl, tracer: 0.8 M NaCl).

| | **Device** | $w_{0.5}$ **(s)** | $\sigma$ **(s)** | $N(1/m)$ |
|---|---|---|---|---|
| Simulation | Column | 4.78 | 4.59 | 5724 |
| | Cuboid | 3.45 | 4.02 | 11225 |
| Experimental | Column | - | - | 1899 |
| | Cuboid | - | - | 4537 |

# Conclusion

The efficiency of chromatographic separation is significantly influenced by device hydrodynamics, which in turn is critically dependent on device design. This computational fluid dynamic study provided insight into the workings of a cuboid packed-bed and its equivalent column. It also explains the reasons for the superior separation performance of the cuboid packed-bed device. Flow non-uniformity in column headers was found to be the key factor responsible for low separation efficiency obtained with wide preparative columns. The CFD simulation showed that radial velocity in the headers decreased very drastically from the axis towards the periphery, resulting in significant radial location-based variability in residence time. The significant increase in residence time along the fluid flow paths closer to the periphery had a profound impact on the column performance. Consistent with this finding, simulation of a pulse of salt and blue dextran tracer injected in a cuboid packed-bed device and its equivalent column revealed differences in time spent by the solute molecules within the two devices. The number of theoretical plates per unit bed height obtained with the cuboid packed-bed device was significantly higher. Consequently, better resolution in chromatographic separation could be expected with this device.

# Acknowledgements

We thank the Natural Science and Engineering Research Council (NSERC) of Canada and the Ontario Research Fund, Research Excellence (ORF RE) program and Mitacs for funding this project. We thank Paul Gatt for the fabrication of the cuboid packed-bed device based on design provided by RG.

## Nomenclature

| | |
|---|---|
| $\epsilon$ | Porosity (-) |
| $K_b$ | Permeability ($m^2$) |
| $P$ | Pressure (Pa) |
| $\mu$ | Fluid dynamic viscosity (Pa$\cdot s$) |
| $\rho$ | Fluid density ($kg/m^3$) |
| $\mathbf{I}$ | Identity matrix |
| $\mathbf{u}$ | Fluid velocity field (m/s) |
| $F$ | External Forces (Pa) |
| $t_R$ | Retention volume ($m^3$) |
| $R$ | Radius of column (m) |
| $r$ | Radial location (m) |
| $L$ | Length of cuboid packed-bed (m) |
| $W$ | Width of cuboid packed-bed (m) |
| $w_{0.5}$ | Width at half height ($m^3$)$or(s)$ |
| $\sigma$ | Standard deviation (s) |
| $t$ | Taper length of cuboid device (m) |
| $\theta$ | Taper angle |
| $h_c$ | Channel/header height (m) |
| $h_b$ | Packed-bed height (m) |
| $Q_{in}$ | Inlet flow rate ($m^3/s$) |
| $D$ | Diffusion coefficient ($m^2/s$) |

# References

Atmakidis, T., Kenig, E.Y., 2009. CFD-based analysis of the wall effect on the pressure drop in packed beds with moderate tube/particle diameter ratios in the laminar flow regime. Chem. Eng. J. 155, 404–410. https://doi.org/10.1016/j.cej.2009.07.057

Baur, J.E., Kristensen, E.W., Wightman, R.M., 1988. Radial Dispersion from Commercial High-Performance Liquid Chromatography Columns Investigated with Microvoltammetric Electrodes. Anal. Chem. 60, 2334–2338. https://doi.org/10.1021/ac00172a005

Brinkman, H.C., 1949. A calculation of the viscous force exerted by a flowing fluid on a dense swarm of particles. Flow Turbul. Combust. 1, 27. https://doi.org/10.1007/BF02120313

Camenzuli, M., J. Ritchie, H., R. Ladine, J., Andrew Shalliker, R., 2011. The design of a new concept chromatography column. Analyst 136, 5127–5130. https://doi.org/10.1039/C1AN15681K

Chen, G., Gerrior, A., Ghosh, R., 2018. Feasibility study for high-resolution multi-component separation of protein mixture using a cation-exchange cuboid packed-bed device. J. Chromatogr. A 1549, 25–30. https://doi.org/10.1016/j.chroma.2018.03.029

Chen, G., Ghosh, R., 2018. Effects of process parameters on the efficiency of chromatographic separations using a cuboid packed-bed device. J. Chromatogr. B 1086, 23–28. https://doi.org/10.1016/j.jchromb.2018.04.002

Eon, C.H., 1978. Comparison of broadening patterns in regular and radially compressed large-diameter columns. J. Chromatogr. A, Third International Symposium on Column Liquid Chromatography 149, 29–42. https://doi.org/10.1016/S0021-9673(00)80977-2

Farkas, T., Sepaniak, M.J., Guiochon, G., 1997. Radial distribution of the flow velocity, efficiency and concentration in a wide HPLC column. AIChE J. 43, 1964–1974. https://doi.org/10.1002/aic.690430806

Farkas, T., Sepaniak, M.J., Guiochon, G., 1996. Column radial homogeneity in high-performance liquid chromatography. J. Chromatogr. A 740, 169–181. https://doi.org/10.1016/0021-9673(96)00107-0

Ghosh, R., 2016. Using a box instead of a column for process chromatography. J. Chromatogr. A 1468, 164–172. https://doi.org/10.1016/j.chroma.2016.09.044

Ghosh, R., Chen, G., 2017. Mathematical modelling and evaluation of performance of cuboid packed-bed devices for chromatographic separations. J. Chromatogr. A 1515, 138–145. https://doi.org/10.1016/j.chroma.2017.07.088

Ghosh, R., Madadkar, P., Wu, Q., 2016. On the workings of laterally-fed membrane chromatography. J. Membr. Sci. 516, 26–32. https://doi.org/10.1016/j.memsci.2016.05.064

Knox, J.H., Laird, G.R., Raven, P.A., 1976. Interaction of radial and axial dispersion in liquid chromatography in relation to the "infinite diameter effect." J. Chromatogr. A 122, 129–145. https://doi.org/10.1016/S0021-9673(00)82240-2

Lightfoot, E. n., Moscariello, J. s., 2004. Bioseparations. Biotechnol. Bioeng. 87, 259–273. https://doi.org/10.1002/bit.20111

Low, D., O'Leary, R., Pujar, N.S., 2007. Future of antibody purification. J. Chromatogr. B, Polyclonal and Monoclonal Antibody Production, Purification, Process and Product Analytics 848, 48–63. https://doi.org/10.1016/j.jchromb.2006.10.033

Madadkar, P., Ghosh, R., 2016. High-resolution protein separation using a laterally-fed membrane chromatography device. J. Membr. Sci. 499, 126–133. https://doi.org/10.1016/j.memsci.2015.10.041

Madadkar, P., Nino, S.L., Ghosh, R., 2016. High-resolution, preparative purification of PEGylated protein using a laterally-fed membrane chromatography device. J. Chromatogr. B 1035, 1–7. https://doi.org/10.1016/j.jchromb.2016.09.014

Madadkar, P., Umatheva, U., Hale, G., Durocher, Y., Ghosh, R., 2017. Ultrafast Separation and Analysis of Monoclonal Antibody Aggregates Using Membrane Chromatography. Anal. Chem. 89, 4716–4720. https://doi.org/10.1021/acs.analchem.7b00580

Madadkar, P., Wu, Q., Ghosh, R., 2015. A laterally-fed membrane chromatography module. J. Membr. Sci. 487, 173–179. https://doi.org/10.1016/j.memsci.2015.03.056

Moscariello, J., Purdom, G., Coffman, J., Root, T.W., Lightfoot, E.N., 2001. Characterizing the performance of industrial-scale columns. J. Chromatogr. A, 13th International Symposium on Preparative and Process Chromatography 908, 131–141. https://doi.org/10.1016/S0021-9673(00)01062-1

Przybycien, T.M., Pujar, N.S., Steele, L.M., 2004. Alternative bioseparation operations: life beyond packed-bed chromatography. Curr. Opin. Biotechnol. 15, 469–478. https://doi.org/10.1016/j.copbio.2004.08.008 Roblee, L.H.S., Baird, R.M., Tierney, J.W., 1958. Radial porosity variations in packed beds. AIChE J. 4, 460–464. https://doi.org/10.1002/aic.690040415

Sadavarte, R., Madadkar, P., Filipe, C.D., Ghosh, R., 2018. Rapid preparative separation of monoclonal antibody charge variants using laterally-fed membrane chromatography. J. Chromatogr. B 1073, 27–33. https://doi.org/10.1016/j.jchromb.2017.12.003

Shalliker, R.A., Broyles, B.S., Guiochon, G., 2000. Physical evidence of two wall effects

in liquid chromatography. J. Chromatogr. A 888, 1–12. https://doi.org/10.1016/S0021-9673(00)00517-3 Shalliker, R.A., Ritchie, H., 2014. Segmented flow and curtain flow chromatography: Overcoming the wall effect and heterogeneous bed structures. J. Chromatogr. A, Editors' Choice VIII 1335, 122–135. https://doi.org/10.1016/j.chroma.2013.08.004

Shukla, A.A., Thömmes, J., 2010. Recent advances in large-scale production of monoclonal antibodies and related proteins. Trends Biotechnol. 28, 253–261. https://doi.org/10.1016/j.tibtech.2010.02.001 Stickel, J.J., Fotopoulos, A., 2001. Pressure-flow relationships for packed beds of compressible chromatography media at laboratory and production scale. Biotechnol. Prog. 17, 744–751. https://doi.org/10.1021/bp010060o

Tallarek, U., Bayer, E., Guiochon, G., 1998. Study of Dispersion in Packed Chromatographic Columns by Pulsed Field Gradient Nuclear Magnetic Resonance. J. Am. Chem. Soc. 120, 1494–1505. https://doi.org/10.1021/ja9726623

Umatheva, U., Madadkar, P., Selvaganapathy, P.R., Ghosh, R., 2018. Computational fluid dynamic (CFD) simulation of laterally-fed membrane chromatography. Chem. Eng. Res. Des. https://doi.org/10.1016/j.cherd.2018.07.026

Vangelooven, J., Malsche, W.D., Beeck, J.O.D., Eghbali, H., Gardeniers, H., Desmet, G., 2010. Design and evaluation of flow distributors for microfabricated pillar array columns. Lab. Chip 10, 349–356. https://doi.org/10.1039/B916126K

Yuan, Q.S., Rosenfeld, A., Root, T.W., Klingenberg, D.J., Lightfoot, E.N., 1999. Flow distribution in chromatographic columns. J. Chromatogr. A 831, 149–165. https://doi.org/10.1016/S0021-9673(98)00924-8

# Chapter 5

# Purification of bacterial virulence factor pertactin using high affinity ligands

This chapter outlines a collaboration with Sanofi Pasteur, a vaccine manufacturing company located in Toronto, ON, Canada. This project demonstrates the feasibility of purifying pertactin from a concentrated feed material using short chained, high-affinity peptides. The work comprises of a design space exploration for maximizing purity and recovery of pertactin.

In this work, I executed the experiments and was the primary author of the manuscript. My project at Sanofi Pasteur was supervised by Dr. Melih Tamer and Dr. John Riley. Léo Sauvaget and Dr. Braden Sweeting provided me with practical and technical advice when I was planning my experiments. Nerissa Dela Rosa aided me with in-lab training and execution of experiments. Dr. Raja Ghosh supervised the project and edited the manuscript. This chapter is being prepared to be submitted to a peer-reviewed journal.

# Purification of bacterial virulence factor pertactin using high affinity ligands

Umatheny Umatheva[a], Braden Sweeting[b], Léo Sauvaget[b], Nerissa Dela Rosa[c], John Riley[c], Melih Tamer[b], Raja Ghosh[a*]

[a] Department of Chemical Engineering, McMaster University
1280 Main Street West, Hamilton, ON, Canada L8S 4L7

[b] Manufacturing Technology, Sanofi Pasteur, Toronto
1755 Steeles Ave W, North York, ON, Canada M2R 3T4

[c] Bioprocess Research and Development, Sanofi Pasteur, Toronto
1755 Steeles Ave W, North York, ON, Canada M2R 3T4

[*]Corresponding Author
Email: rghosh@mcmaster.ca
Phone: +1 905−525 9140 ext 27415

**Abstract**
Pertussis, also known as whooping cough, is a contagious bacterial disease, caused by *Bordetella pertussis*. It is an airborne disease that causes coughing fits, difficulty in breathing, and in more severe cases death. Whooping cough is a life-threatening disease which could be prevented by proper immunization. One of the common formats of the acellular vaccine comprises a mixture of pertussis toxin (PT), fimbriae (FIM), filamentous hemagglutinin (FHA) and the virulence factor pertactin (PRN). The purification of PRN is challenging due to its low abundance in the fermentation broth. A typical purification process for PRN requires multiple laborious unit operations, and the final product recovery being less than 20%. This paper presents a purification scheme for PRN, using affinity ligands produced by mRNA display technology, which results in a purity of 90% and a recovery of about 100%.

**Keywords:** Pertactin, PRN, vaccine, affinity chromatography, affinity ligand, DoE

# Introduction

*Bordetella pertussis* is a human pathogen that affects people of all ages (Guiso, 2009). While adolescents and adults tend to display mild symptoms, infants and young children, especially those who have not been immunized, are the most vulnerable to the wide spectrum of toxins and pharmacologically active entities produced by *B. pertussis*. Children under the age of six months make up the majority of the hospitalized cases relating to *B. pertussis* infections (Guiso, 2009). *B. pertussis* infection causes whooping cough, a highly contagious disease that infects the human respiratory tract. Whooping cough is characterized by violent coughing fits leading to breathing complications, and often results in death due to the lack of oxygen intake. Whooping cough has been substantially controlled through large-scale immunization programs spanning over 70 years (Jackson et al., 1995).

In the past, a "whole cell" vaccine was used in North America for preventing *B. pertussis* infections. This vaccine was prepared by culturing the organism in a fermenter, followed by killing the cells and inactivating the bacterial toxins using chemical agents, such as formaldehyde (Jackson et al., 1995). The killed cells were then re-suspended and used directly or in combination with other antigens. This vaccine formulation, although extremely efficacious, was associated with side effects such as fever, local reactions, and convulsions (Guiso, 2009; Jackson et al., 1995). Many of these symptoms were attributed to lipopolysaccharides (LPS) and other active toxins (Cherry, 1996; Zorzeto et al., 2009). As a result, there had been a decreased public acceptance of this vaccine in a number of countries such as; Japan, Sweden and the U.K. (Guiso, 2009), (Jackson et al., 1995). The decrease in immunization has led to several outbreaks of the disease. In response to this, several manufacturers and researchers have developed efficacious acellular pertussis vaccines that consist of a cocktail of highly purified protein antigens from *B. pertussis* (Edwards, 1993; Edwards et al., 1995; Guiso, 2009). The pertussis antigens used to formulate commercial acellular vaccines may include pertactin (PRN), pertussis toxin (PT), fimbriae (FIM), and filamentous hemagglutinin (FHA) (Edwards, 1993; Edwards et al., 1995; Guiso, 2009). Industrial scale purification of antigens from *B. pertussis* cells for producing the acellular vaccine is challenging. This is particularly the case with PRN which is an outer membrane protein, with a molecular weight of approximately 69 kDa, found on all virulent strains of *B. pertussis* (Emsley et al., 1996). With many of the current production methods, which are decades old, the loss in yield of PRN during purification is substantial. The purification of PRN requires a laborious multistep process that typically yields less than 20% of the initial levels of the target protein from the *Bordetella pertussis* cells (Camper and Viola, 2009). PRN being the limiting antigen in Pertussis vaccine manufacturing, vaccine manufactures are looking to improve PRN yield by process modification, or by adoption of new purification processes.

The main methods for PRN purification used by manufactures and reported in the literature use ion-exchange chromatography (IEC) and hydrophobic interaction chromatography (HIC) (Jackson et al., 1995; Li et al., 2016; Suehara et al., 2009). The primary challenge with these methods is that it is difficult to get high recovery of the target protein without compromising on the purity. This is because of non-specific binding of proteins onto the col-

umn, which necessitates the use of multiple unit operations and intermediate concentration and conditioning steps, which leads to considerable product loss.

Purification of PRN by affinity chromatography could potentially be a suitable solution and alternative to current methods and techniques. The use of biological ligands for affinity chromatographic purification began in the 1960s (Cuatrecasas et al., 1968; Sonenberg et al., 1979; Wofsy and Burr, 1969), the main advantages being high binding capacities, and a significant reduction in non-specific binding, both of which could potentially lead to high recovery and high purity of the target molecule. Developments in methods for affinity ligand design has made it possible to synthesize high affinity ligands for the purification of target molecules such as PRN (Huang et al., 2016; Irving et al., 2001; Lipovsek and Plückthun, 2004; Tinberg et al., 2013). The affinity ligands used in this work were produced using mRNA display technology, which involves covalently binding the mRNA to the peptide it encodes. The mRNA – peptide complex is then purified from the ribosome and the functional peptides are isolated by *in-vitro* selection (Lipovsek and Plückthun, 2004). This paper explores the feasibility of using such ligands for development of affinity chromatography-based processes for the purification of PRN.

# Methods

## Design of experiments

A 3-factors, full factorial design of experiments was used to explore the effects of ligand type and process parameters on affinity chromatography of PRN. The specific objective of the experiments was to determine conditions for maximum PRN purity and recovery, and LPS (or endotoxin) removal. The factors that were investigated are tabulated in Table 5.1.

Table 5.1: DoE Factors tested

| Factor | Low | High |
|---|---|---|
| Elution buffer pH | 3 | 4 |
| Affinity ligand (peptide) | Peptide 1 (P1) | Peptide 3 (P3) |
| Wash sequence | 0.5% Tween 20 wash | 0.5% Tween 20 wash + 1 M NaCl wash |

## Ligand coupling reaction

The affinity ligand (obtained from Bachem, Torrance, CA, USA) solution (10 mg/mL) was prepared in DMSO (A13280, Alfa Asear, Haverhill, MA, USA), 20 mM HEPES (PHG001-110G, Sigma Aldrich, Oakville, ON, Canada), 150 mM NaCl (1.16224.9029, Emprove Millipore, Oakville, ON, Canada), 0.1% (v/v) Tween 80 (P5188-100mL, Sigma Life Sciences, Oakville, ON, Canada), and the pH values was adjusted to 7.4. Specific details on the affinity ligands can not be disclosed. The primary amine (–NH2) of the ligands were coupled to N-hydroxysuccinimide (NHS) activated resin housed in a 1 mL prepacked NHS-activated

HP column (17090601, GE Healthcare, Mississauga, ON, Canada) according to the manufacturer's instructions. The column was washed with 6 column volumes (CVs) of 1 mM cold HCl (SA56-1, Fisher Scientific, Waltham, MA, USA), using a syringe at flow rate of 0.5 drops/sec, followed by passage of the peptide solution. The unreacted groups on the column were blocked by three cycles of 6 CVs of 0.5 M ethanolamine (A11697, Alfa Aesar, Haverhill, MA, USA) prepared in 0.5 M NaCl (pH 8.3) followed by 6 CVs of sodium acetate (32318-1KG-R, Sigma Aldrich, Oakville, ON, Canada) in 0.5 M NaCl (pH 4.0), both at 1 mL/min flow rate. The coupling efficiency of the affinity ligand to the resin was determined using a mass balance by tracking the UV absorbance on the SoloVPE at 280 nm (C Technologies, Bridgewater, NJ, USA) of the peptide. A larger affinity column (GE XK 16/20 column) was prepared by packing affinity resin prepared by coupling the peptide to NHS-Activated Sepharose (17090601, GE Healthcare, Mississauga, ON, Canada) according to the manufacturer's instructions. A 15 mL aliquot of NHS-activated Sepharose was washed with 150 mL of 1 mM HCl. Once the resin had settled, the HCl was pipetted out and peptide solution was added. The affinity media was then packed in the column and unreacted groups were blocked by three cycles of 6CVs of 0.5 M ethanolamine prepared in 0.5 M NaCl (pH 8.3) and 6 CVs of sodium acetate in 0.5 M NaCl (pH 4.0), at 5.22 mL/min flow rate. The effective bed volume of the larger affinity column was 15 mL.

## Chromatographic purification

Chromatographic purification of PRN was carried out using an AKTA Pure liquid chromatography system (GE Healthcare, Mississauga, ON, Canada). The 1 mL affinity column was operated at a flow rate of 1.0 mL/min, while the 15 mL column was operated at 5.22 mL/min. The respective column was equilibrated with buffer A: 50 mM Tris-HCl (4102-05, J.T Baker, Phillipsburg, NJ, USA), containing 0.1% (v/v) Tween 20 (P7949-100mL, Sigma Life Science, Oakville, ON, Canada), pH value adjusted to 8.0. The column was loaded with 100x concentrated fermentation broth (containing 0.1% v/v Tween 20 and micro-filtered through 0.45 $\mu$m membrane filter). After a chase using buffer A, the columns were then either washed with a high detergent wash consisting of buffer A + 0.5% (v/v) Tween 20, or with a high detergent and salt combination wash consisting of buffer A + 0.5% (v/v) Tween 20 followed by buffer A + 1 M NaCl. Elution of PRN was achieved by step change to the eluting buffer (buffer B) which was either 100 mM Na-citrate (pH 3.0), or 100 mM Na-citrate (pH 4.0). The flow-through and wash was collected as 2 mL fractions, while the 1 mL eluate fractions were collected into 10% of the collection volume of 1 M Tris-HCl pH 8.0 to prevent PRN denaturation.

Prior to the first use of the columns, the height equivalent to the theoretical plate (HETP) of each affinity column was evaluated after the peptide coupling step to assess the quality of resin packing, as there was a risk of compressing the resin during the coupling reaction. A 25 $\mu$L and 300 $\mu$L pulse injection of 1M NaCl, 50mM Tris-HCL in 50mM Tris-HCl was used in the 1 mL and 15 mL columns respectively.

## Analytical methods

### Total protein assay

The total protein concentration of eluate fractions and starting feed material was determined in duplicate using the microBCA method. The bovine serum albumin standard (23209), microBCA reagents A (23231), B (23232) and C (23234) were obtained from Thermo Scientific (Waltham, MA, USA). Samples were diluted to less than 300 $\mu$g/mL using PBS. A 50 $\mu$L aliquot of each sample was mixed with 200 $\mu$L of working reagent in a 96-well transparent microplate and incubated at 60 ℃ for 25 min. The absorbance at 570 nm was measured using a VersaMax plate reader (Molecular Devices, San Jose, CA, USA) and the concentration was calculated from a BSA calibration curves in the concentration range from 0 to 300 $\mu$g/mL.

### LAL assay

The limulus amoebocyte lysate (LAL) assay was conducted using the Charles River Endosafe Nexgen-PTS system (Wilmington, MA, USA). The eluate fractions were diluted with LAL reagent water (W130, Charles River, Wilmington, MA, USA) until a valid test result was obtained (i.e. the spike recovery value was in the range of 50-200% ). Endotoxin activity was measured in terms of Endotoxin Units (EU/mL). The reduction of endotoxin, typically reported as a log reduction value (LRV), was calculated using the equation below, based on endotoxin concentration of the sample and the feed material.

$$LRV = log\left(\frac{C_{feedmaterial}}{C_{sample}}\right)$$

### SDS PAGE

Collected fractions were analyzed on 4-12% Bis-Tris SDS protein gels (NP0322BOX, ThermoFisher, Waltham, MA, USA) under reducing conditions (in presence of -mercaptoethanol). Elution pools (EP) were loaded with 2, 4, and 6 g total protein per lane for purity estimations. The gels were stained with Coomassie blue stain (InstantBlue™, Expedeon, Cambridgeshire, UK) and destained with water before densitometric analysis. Densitometry was performed using Bio-Rad's GS-900 densitometer and Image Lab software (Hercules, CA, USA).

### PRN samples ELISA

The PRN concentration determined by enzyme-linked immunosorbent assay (ELISA) method was conducted by the QC Immunochemistry Department at Sanofi Pasteur (North York, ON, Canada). PRN was captured on microtiter plates coated with a PRN antibody and detected through subsequent incubations with a Guinea Pig anti-PRN antibody. The absorbance was measured using a SpectraMax ELISA plate reader (Molecular Devices, San Jose, CA, USA) at 450 nm. Sample concentrations were determined based on a standard curve generated by plotting the absorbance versus PRN concentrations.

# Results and Discussion

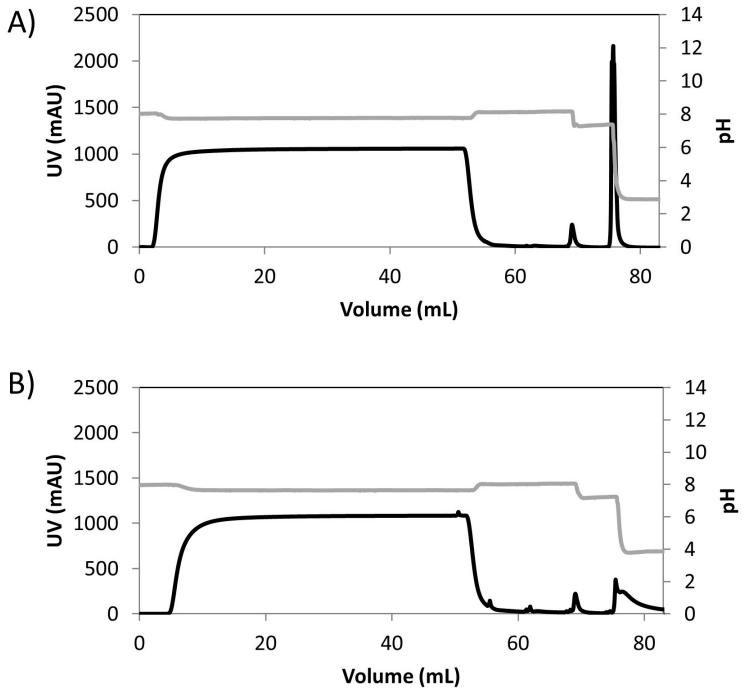


Figure 5.1: Purification of concentrated fermentation broth by affinity chromatography column coupled with P1; column bed volume: 1 mL; load volume: 50 mL; binding buffer: 50 mM Tris-HCl, 0.1% (v/v) Tween 20, pH 8.0; washing buffers: 50 mM Tris-HCl, 0.5% (v/v) Tween 20, pH 8.0 followed by 50 mM Tris-HCl, 0.1% (v/v) Tween 20, 1 M NaCl, pH 8.0; eluting buffer: (A) 100 mM NaCitrate pH 3 and (B) 100 mM NaCitrate pH 4; flow rate: 1 mL/min; black line: UV absorbance; grey line: pH.

In order to demonstrate the effectiveness of the AC method and screen processing parameters, a design of experiments was used. 1 mL activated Sepharose columns were coupled with P1 and P3 affinity peptides and were used to investigate the effects of the pH of the elution buffer and types of washing buffers on the purity and recovery of the PRN eluate. The purification scheme for the AC method was equilibration, loading, equilibration buffer chase, washing with (1) 0.5% (v/v) Tween 20 or (2) 0.5% (v/v) Tween 20 and 1 M NaCl buffers and elution. The different on-column washing steps were included in the scheme with the objective of maximizing endotoxin removal. Detergents and salt solutions are used to solubilize the endotoxin, which would help clear them from the column before the PRN was eluted from the column. A step change to 100% eluting buffer was chosen since, the affinity ligands have specific binding to PRN and AC column was intended to capture and concentrate the PRN in the feed material; a gradient strategy would unnecessarily dilute the eluate fraction. Figure 5.1 and Figure 5.2 show the chromatogram of the purification of PRN using the column coupled with P1 and P3 affinity peptide respectively. For both ligand types, the amount of eluted protein was lower, when 100 mM NaCitrate pH 4 was used to elute the

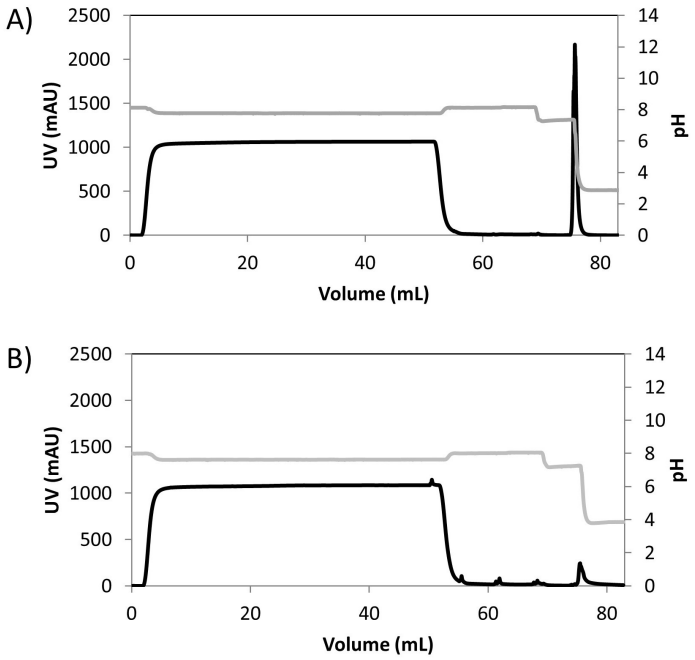


Figure 5.2: Purification of concentrated fermentation broth by affinity chromatography column coupled with P3; column bed volume: 1 mL; load volume: 50 mL; binding buffer: 50 mM Tris-HCl, 0.1% (v/v) Tween 20, pH 8.0; washing buffers: 50 mM Tris-HCl, 0.5% (v/v) Tween 20, pH 8.0 followed by 50 mM Tris-HCl, 0.1% (v/v) Tween 20, 1 M NaCl, pH 8.0; eluting buffer: (A) 100 mM NaCitrate pH 3 and (B) 100 mM NaCitrate pH 4; flow rate: 1 mL/min; black line: UV absorbance; grey line: pH.

protein compared to 100 mM NaCitrate pH 3. The flow-through contains FHA, PT and other host cell proteins. Total protein yields were 3.22 ± 0.01 mg (P1-column) and 0.766 ± 0.008 mg (P3-column) for runs that used pH 4 elution buffer compared to yields of 7.5 ± 0.8 mg (P1-column) and 5.6 ± 0.6 mg (P3-column) for runs that used pH 3 elution buffer. The lower total protein yields in the eluate when the column was eluted with pH 4 buffer showed that the ligands have a high binding affinity to PRN and only under very acidic conditions the protein will be released from the ligand sites. The eluate was collected in 1 M Tris-HCl pH 8.0 to neutralize the eluate and to reduce the risk of PRN denaturation. In addition, the wider and tailed peak observed at pH 4 condition showed that at there was slower dissociation kinetics.

The experimental run order was blocked by pH such that runs 1-4 used pH 3 elution buffer (grey bars) and runs 5-8 used pH 4 elution buffer (black bars). Figure 5.3A shows the PRN recovery for each of the runs by multiplying total protein with PRN purity determined by the densitometer and Figure 5.3B shows the purity of the eluate. As previously observed in Figure 5.1 and Figure 5.2, the pH of the elution buffer effects the PRN recovery. Typically,

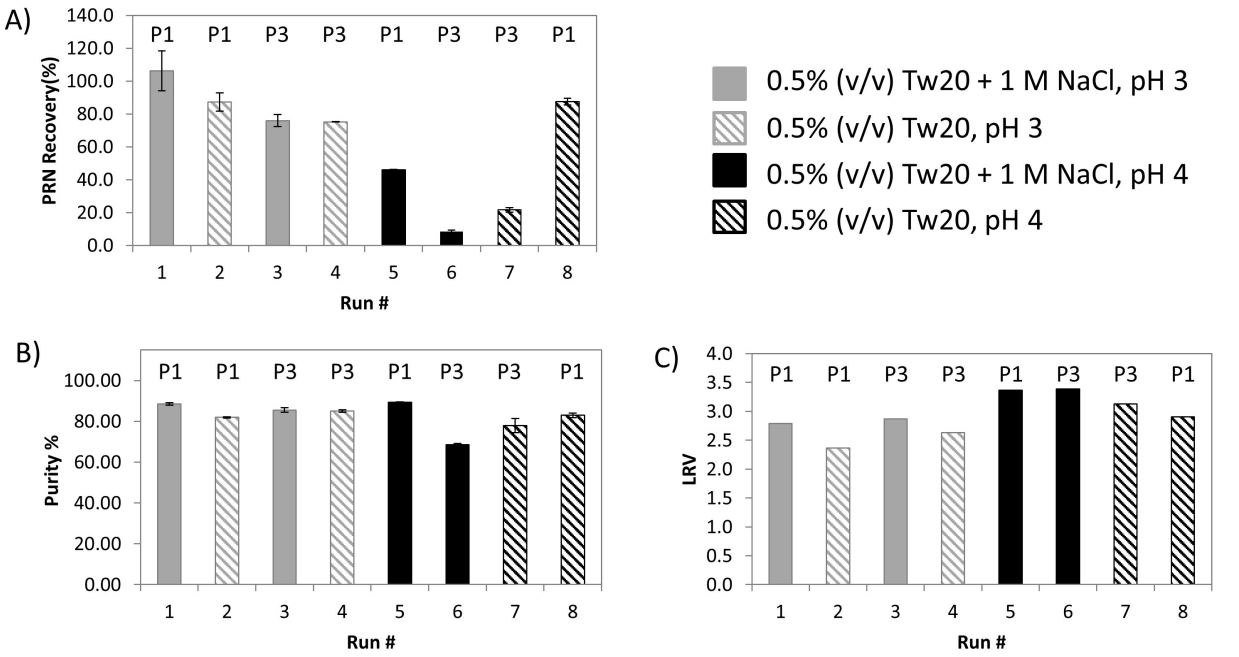


Figure 5.3: The comparison of response values for each DoE run. The error bars in A) and B) are based on propagation of error from triplicate tests. A) PRN recovery in eluate samples B) PRN purity determined by densitometry C) Log reduction value of endotoxin comparing eluate to feed material.

the loss of protein is associated with incomplete protein capture by the column; however, in this case, it was due to incomplete stripping of the column of bound protein. In Figure 5.3A, runs 7 and 8 have an over estimated PRN recovery because there was residual protein from runs 5 and 6 that was eluted during runs 7 and 8. The purity of the elute samples were in the range of 70-90% after a single pass through the AC columns. Figure 5.3C shows the LRV for each run comparing the endotoxin concentrations, determined by the LAL assay, of the eluate to the feed material. The best reduction of endotoxin activity was in the order of $10^5$ EU/100 $\mu$g total protein (1000-fold reduction), and consequently polishing steps for targeted removal of endotoxin will be needed following the AC column to meet the target limit of 15 EU/100 $\mu$g total protein.

To evaluate the effects of the factors mentioned in Table 5.1 on the response variables (i.e. purification efficiency as evaluated in terms of endotoxin LRV, PRN recovery and purity), an ANOVA was conducted, and backward stepwise regression approach was used, keeping only significant terms in the models (i.e. p-value greater than 0.5) (Amadeo et al., 2014; Roy and Roy, 2008). Models for PRN recovery and purity had low model confidence due to a small sample size and variability in the data. However, based on the chromatograms, there is a strong indication that the pH of the elution buffer affects the recovery of PRN as seen in Figure 5.1 and Figure 5.2. A statistically fit model, in terms of indicators such as

$R^2$, $Q^2$ and $R^2 - Q^2$, was formulated for endotoxin LRV prediction. The LRV of endotoxin is modeled by the following equation for coded values for each factor:

$$LRV = 2.92875 + 0.26625pH + 0.17375Wash + 0.07375Peptide - 0.05125(Peptide \times Wash)$$

Maximum LRV was achieved by using pH 4 elution buffer, washing with both detergent and salt washes and affinity peptide, P3. The use of 0.5% (v/v) Tween 20 wash and 1 M NaCl wash was intended for on-column reduction of endotoxin by increasing the hydrophobicity and to promote micellar aggregation of the lipopolysaccharides (LPS). Based on the LRV predictive model, the pH of elution buffer had the greatest influence on endotoxin removal. A less acidic pH (pH = 4) resulted in lower endotoxin activity levels in the elution pools. This is likely due to the slower dissociation of PRN from the affinity peptides and low total protein yields in these runs. The LPS that were bound to the PRN that remained on the column, when eluted with pH 4 buffer, may have also remained on the column with the PRN. There are strong electrostatic and hydrophobic interactions between endotoxin and protein stabilized by calcium bridges (Chen et al., 2009; Ongkudon et al., 2012; Ritzén et al., 2007). The LRV model suggests that the performance of P1 was better with both detergent and salt washes and that P3 was better with detergent wash alone, in terms of endotoxin removal. This could indicate the column that had P1 ligands had a stronger electrostatic interaction to endotoxin molecules, compared to P3 ligands, and required more stringent on-column washing.

Based on the results of the DoE, an intermediate-scale column was used to verify the scalability of the AC method in terms of PRN recovery and purity at the best run conditions observed at the 1mL scale. A 15mL bed volume column coupled with 33.7 mg of P1 was compared to the 1 mL bed column coupled with 1.9 mg of P1. A comparison of the small and intermediate scale columns is shown in Table 5.2. Figure 5.4 shows the chromatogram of the purification of 50 mL PRN feed material on a 1 mL affinity column with P1 ligand washed with equilibration buffer chase, 0.5% (v/v) Tween 20 and 1 M NaCl washes then eluted with 100 mM NaCitrate pH 3. Figure 5.5 shows the corresponding chromatogram of the purification of 200 mL PRN feed material on a 15 mL affinity column with P1 ligand, with an additional wash step with the equilibration buffer before eluting with 100 mM NaCitrate pH 3. The PRN eluate was collected in less than 2 column volumes which would be beneficial when preparing the sample for polishing steps.

Table 5.2: Comparison of small and intermediate scale column couple with P1

| **Parameter** | **Units** | **1 mL-scale** | **15 mL-scale** |
|---|---|---|---|
| **Coupled peptide** | mg | 1.9 | 33.7 |
| **Bed Volume** | mL | 0.96 | 14.78 |
| **Ligand Concentration** | mg/mL resin | 2.0 | 2.3 |
| **HETP** | m | $4.15\times10^{-4}$ | $4.39\times10^{-4}$ |

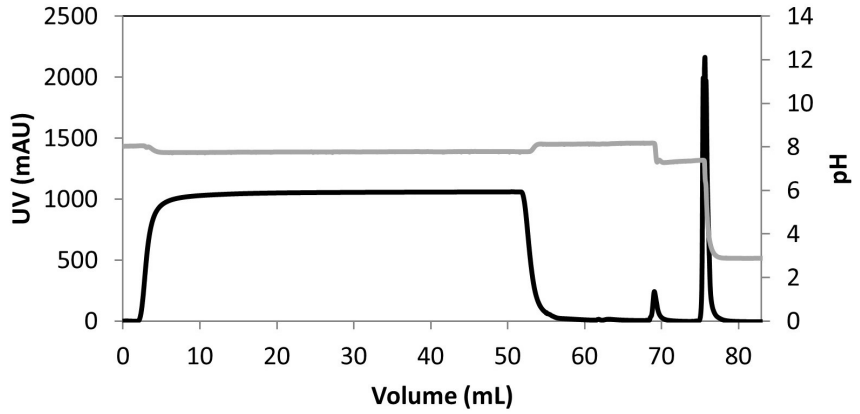


Figure 5.4: $A_{280}$ chromatographic profile of PRN purification by a 1 mL affinity chromatography column coupled with P1 with a step change elution strategy; load volume: 50 mL; binding buffer: 50 mM Tris-HCl, 0.1% (v/v) Tween 20, pH 8.0; washing buffers: 50 mM Tris-HCl, 0.5% (v/v) Tween 20, pH 8.0 and 50 mM Tris-HCl, 0.1% (v/v) Tween 20, 1 M NaCl, pH 8.0; eluting buffer:100 mM NaCitrate pH 3; flow rate: 1 mL/min; black line: UV absorbance; grey line: pH.

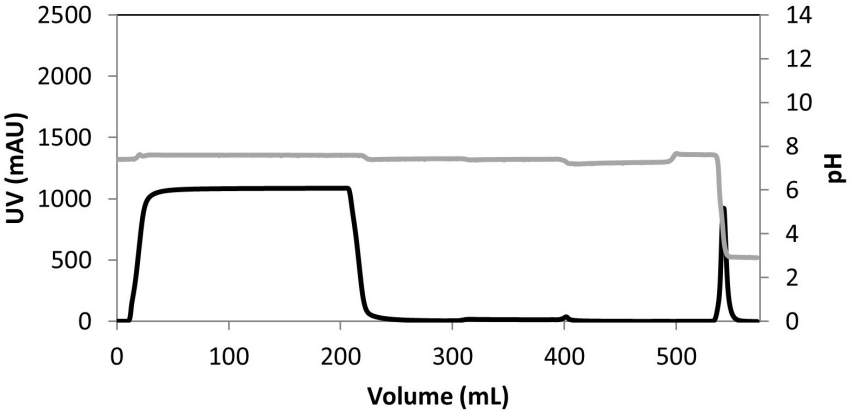


Figure 5.5: $A_{280}$ chromatographic profile of PRN purification by a 15 mL affinity chromatography column coupled with P1 with a step change elution strategy; load volume: 50 mL; binding buffer: 50 mM Tris-HCl, 0.1% (v/v) Tween 20, pH 8.0; washing buffers: 50 mM Tris-HCl, 0.5% (v/v) Tween 20, pH 8.0 and 50 mM Tris-HCl, 0.1% (v/v) Tween 20, 1 M NaCl, pH 8.0; eluting buffer:100 mM NaCitrate pH 3; flow rate: 1 mL/min; black line: UV absorbance; grey line: pH.

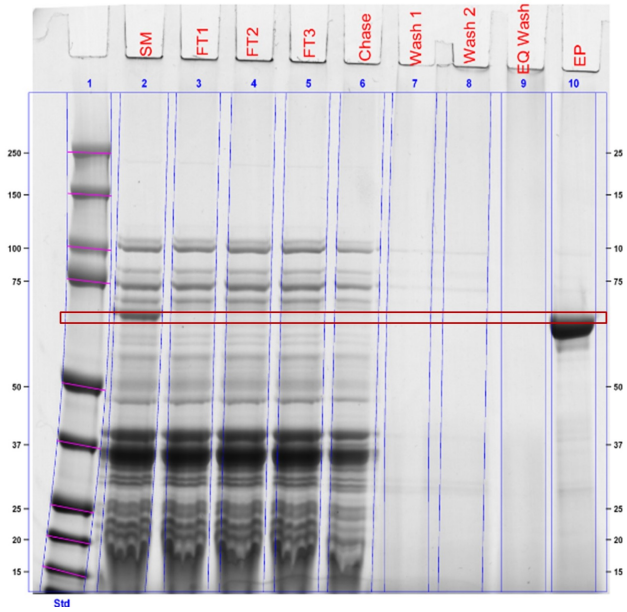


Figure 5.6: SDS-PAGE analysis of fractions collected using 15 mL bed volume column.The samples include: starting material (SM), flow-through fractions (FT), chase, detergent wash (wash 1), salt wash (wash 2), equilibration buffer wash (EQ wash) and elution pool (EP).

The protein profile of the chromatographic process can be visualized by SDS-PAGE analysis in Figure 5.6. There was complete capture of PRN by the AC column as seen by lack of a PRN band present in the flow-through fractions. The chase and on-column wash steps were able to remove additional protein impurities and no PRN was lost in these steps. The purity based on densitometric analysis of lanes loaded with 2, 4, and 6 ug of the elution pool was 88.5 ± 1.3% and 90.3 ± 0.6% for the 1 mL and 15 mL columns. Figure 5.7 shows the normalized mass of PRN, determined by ELISA, in the collected fractions using the 15 mL P1-coupled column. As seen previously by the SDS-PAGE gel, the affinity column was able to capture all of the loaded PRN. The greater than 100% PRN recovery in the EP could be attributed to inherent sources of error associated with this method such as an underestimation of PRN in the feed material due to interference of other non-binding proteins and the presence of detergent. A more accurate method of antigen quantification could be by an HPLC method.

The endotoxin removal by the AC was tracked for each collected fraction, as seen in Figure 5.8. The equilibrium chase following the loading of the feed material was able to remove loosely bound endotoxin species. The subsequent 0.5% Tween 20 and 1 M NaCl washes were able to remove more endotoxin and the final equilibrium buffer wash removed any endotoxin species that became loosely attached during the on-column washes. In terms of a mass balance on the endotoxin, about 46% of the endotoxin loaded onto the column was recovered in the collected fractions. It is possible that the remaining endotoxin was attached to the affinity peptides and within resin pores within the column. The PRN elution had a final concentration of $1.25 \times 10^5$ EU/100 $\mu$g total protein, which was a 2.9 log reduction in endotoxin from the feed material.

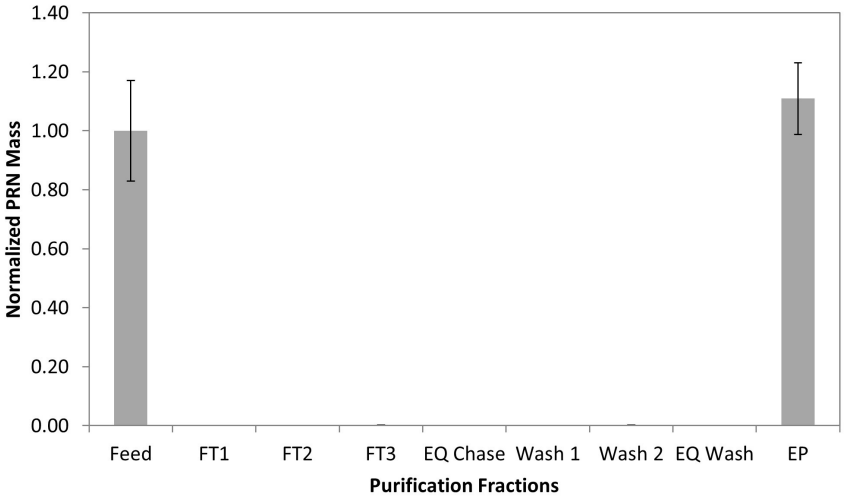


Figure 5.7: Normalized mass of PRN at each chromatographic step using a 15 mL affinity chromatography column.

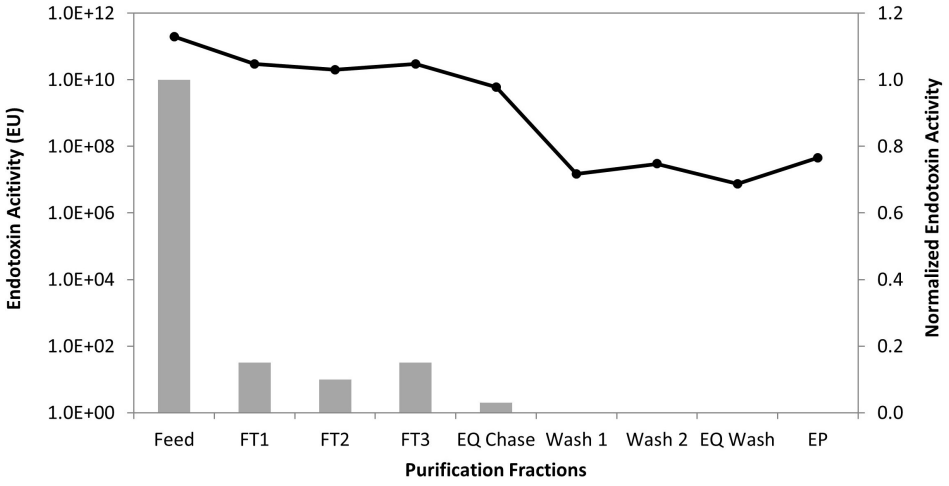


Figure 5.8: Endotoxin activity at each chromatographic step using a 15 mL affinity chromatography column. (Line: endotoxin activity, Bars: normalized endotoxin activity)

## Conclusion

The use of an affinity chromatographic purification has the potential to simplify the multistep purification process of PRN. It is a targeted method that was able to yield a PRN eluate of 90% purity and 100% recovery of the loaded PRN. It has found that due to the high affinity nature of the affinity peptides to the target molecule, an elution buffer of pH 3 was necessary to dissociate bound PRN from the column. At this elution condition, the PRN eluate could be collected in 1-2 column volumes which is beneficial when preparing the sample for subsequent polishing steps. The use of on-column washing steps with 0.5% (v/v) Tween 20 and 1 M NaCl reduced the endotoxin content by 1000-fold; however, an additional endotoxin removal step will be required to meet regulatory limits. Further investigation into ligand leaking and column reproducibility and robustness need to be explored. However, considering the high purity, and recovery achieved at laboratory scales, purification of PRN by high affinity peptides-based chromatography could be a feasible alternative to current industrial practices.

## Acknowledgements

This work was funded by the Mitacs Accelerate program and Sanofi Pasteur.

# References

Amadeo I, Mauro L, Ortí E, Forno G. 2014. Establishment of a Design Space for Biopharmaceutical Purification Processes Using DoE. In: Labrou, NE, editor. Protein Downstr. Process. Des. Dev. Appl. High Low-Resolut. Methods. Totowa, NJ: Humana Press. Methods in Molecular Biology, pp. 11–27. https://doi.org/10.1007/978-1-62703-977-$2_2$.

Camper DV, Viola RE. 2009. Fully automated protein purification. Anal. Biochem. 393:176–181.

Chen RH, Huang C-J, Newton BS, Ritter G, Old LJ, Batt CA. 2009. Factors affecting endotoxin removal from recombinant therapeutic proteins by anion exchange chromatography. Protein Expr. Purif. 64:76–81.

Cherry JD. 1996. Historical Review Of Pertussis And The Classical Vaccine. J. Infect. Dis. 174:S259–S263.

Cuatrecasas P, Wilchek M, Anfinsen CB. 1968. Selective enzyme purification by affinity chromatography. Proc. Natl. Acad. Sci. 61:636–643.

Edwards KM. 1993. Acellular Pertussis Vaccines—A Solution to the Pertussis Problem? J. Infect. Dis. 168:15–20.

Edwards KM, Meade BD, Decker MD, Reed GF, Rennels MB, Steinhoff MC, Anderson EL, Englund JA, Pichichero ME, Deloria MA, Deforest A. 1995. Comparison of 13 Acellular Pertussis Vaccines: Overview and Serologic Response. Pediatrics 96:548–557.

Emsley P, Charles IG, Fairweather NF, Isaacs NW. 1996. Structure of Bordetella pertussis virulence factor P.69 pertactin. Nature 381:90–92.

Guiso N. 2009. Bordetella pertussis and Pertussis Vaccines. Clin. Infect. Dis. 49:1565–1569.

Huang P-S, Boyken SE, Baker D. 2016. The coming of age of de novo protein design. Nature 537:320–327.

Irving RA, Coia G, Roberts A, Nuttall SD, Hudson PJ. 2001. Ribosome display and affinity maturation: from antibodies to single V-domains and steps towards cancer therapeutics. J. Immunol. Methods 248. Bispecific Antibodies:31–45.

Jackson G, Fahim R, Tan L, Chong P, Vose J, Klein M. 1995. Purification of a pertussis outer membrane protein. US5444159A. https://patents.google.com/patent/US5444159A/en.

Li Z, Zhang Y, Wang Q, Li Z, Liu Y, Zhang S, Zhang G, Ma G, Luo J, Su Z. 2016. Purification design and practice for pertactin, the third component of acellular pertussis vaccine,

from Bordetella pertussis. Vaccine 34:4032–4039.

Lipovsek D, Plückthun A. 2004. In-vitro protein evolution by ribosome display and mRNA display. J. Immunol. Methods 290. Antibodies in Proteomics:51–67.

Ongkudon CM, Chew JH, Liu B, Danquah MK. 2012. Chromatographic Removal of Endotoxins: A Bioprocess Engineer's Perspective. Research article. Int. Sch. Res. Not. https://www.hindawi.com/journals/isrn/2012/649746/.

Ritzén U, Rotticci-Mulder J, Strömberg P, Schmidt SR. 2007. Endotoxin reduction in monoclonal antibody preparations using arginine. J. Chromatogr. B 856:343–347. Roy PP, Roy K. 2008. On Some Aspects of Variable Selection for Partial Least Squares Regression Models. QSAR Comb. Sci. 27:302–313.

Sonenberg N, Rupprecht KM, Hecht SM, Shatkin AJ. 1979. Eukaryotic mRNA cap binding protein: purification by affinity chromatography on sepharose-coupled m7GDP. Proc. Natl. Acad. Sci. 76:4345–4349.

Suehara A, Yamamoto E, Fujii S. 2009. Method of separating protective components of bordetella pertussis. US20090068228A1. http://patents.google.com/patent/US20090068228A1/en.

Tinberg CE, Khare SD, Dou J, Doyle L, Nelson JW, Schena A, Jankowski W, Kalodimos CG, Johnsson K, Stoddard BL, Baker D. 2013. Computational design of ligand-binding proteins with high affinity and selectivity. Nature 501:212–216.

Wofsy L, Burr B. 1969. The Use of Affinity Chromatography for the Specific Purification of Antibodies and Antigens. J. Immunol. 103:380–382.

Zorzeto TQ, Higashi HG, Silva MTN da, Carniel E de F, Dias WO, Ramalho VD, Mazzola TN, Lima SCBS, Morcillo AM, Stephano MA, Antonio MÂR de G, Zanolli M de L, Raw I, Vilela MM dos S. 2009. Immunogenicity of a Whole-Cell Pertussis Vaccine with Low Lipopolysaccharide Content in Infants. Clin. Vaccine Immunol. 16:544–550.

# Chapter 6

# CFD simulations of pertactin purification by affinity chromatography

This mini-chapter is a continuation of the PRN affinity chromatography project presented in chapter 5 with Sanofi Pasteur. This section discusses a CFD simulation of the affinity chromatographic columns coupled with peptide 1 and 3 at the 1 mL bed volume scale.

Dr. Jason Szeto and Camille Houy were the experts who were consulted on the FortéBio octet, a method to determine kinetic constants used in the CFD simulations. I conducted the FortéBio experiments, simulated the affinity chromatography columns and wrote this chapter.

# Computational fluid dynamic simulations of pertactin purification by affinity chromatography

## Introduction

Affinity chromatography is a separation method that purifies a target molecule from a mixture based on its specific binding to an affinity ligand. The affinity ligand is chemically immobilized to a support matrix so that when a sample mixture is passed through the column bed, the molecules which have a specific binding affinity to the ligand become bound. The column is washed with buffer to clear other sample components from the column, after which the buffer is changed to facilitate conditions to dissociate the target molecule. The bound molecules are eluted from the support and the final eluate is a concentrated sample of the purified target molecule.

This application simulates an affinity columns for PRN using affinity peptides P1 and P3. The feed fluid entering the column contained two components: PRN and an arbitrary non-binding tracer. The simulation followed a similar purification scheme as the experiments, where the columns were loaded with the feed material, washed with binding buffer which transitioned into a step change to the elution buffer. The reversible reaction describing the binding and dissociation of PRN is shown in the equation below, where $k_{a,Px}$ is the association constant of PRN to the affinity ligand, $k_d$ is the dissociation constant of PRN from the affinity ligand during binding conditions (neutral pH), and $k_{d'}$ is the dissociation constant of PRN from the affinity ligand under eluting conditions (acidic pH).

$$\text{Peptide} + \text{PRN} \underset{k_d}{\overset{k_{a,Px}}{\rightleftharpoons}} \text{Peptide-PRN} \xrightarrow{k_{d'}} \text{Peptide} + \text{PRN}$$

## Methods

### Fluid Flow

COMSOL Multiphysics 5.4 was used to build a 2D axisymmetric model of the affinity chromatography columns. The steady-state model was built using the *Brinkman Equations* physics package to determine the velocity fields that were responsible for the convective mass transport of the PRN specie. The dynamic binding of PRN to the affinity column was simulated using the *Chemistry* and *Transport of Diluted Species in Porous Media* physics packages. The velocity field within the affinity chromatography columns is described by a numerical solution for the Naiver–Stokes equation, continuity equation and the Brinkman equations. In addition, a mass balances on PRN, affinity ligand, and bound PRN-ligand complex was solved using Eq 6.1, where $C_i$ was the species-specific concentration.

$$\frac{\partial c_i}{\partial t} + \nabla \cdot (-D_i \nabla C_i) + u \cdot \nabla C_i = R_i \tag{6.1}$$

The simulation and process parameters used to solve the CFD models are listed in Table 6.1. These specific inputs were selected with the intention of comparing the simulated and experimental results, which would provide some degree of model validation. In the CFD models, the diffusion coefficient of PRN was estimated by the Stokes-Einstein equation, Eq 6.2 and the permeability of the resin bed was estimated using Eq 6.3 (Wang et al., 2007).

$$D = \frac{k_B T}{6\pi\eta r} \tag{6.2}$$

$$K_b = \frac{U_{b,z} h_b}{\Delta P} \tag{6.3}$$

Table 6.1: Simulation parameters used in the CFD model

| Parameter | | Value |
|---|---|---|
| $h_b$ | Bed Height (m) | 0.025 |
| $R$ | Radius of column (m) | $3.5\times10^{-3}$ |
| $r_{be}$ | Average resin bead radius (m) | $1.7\times10^{-5}$ |
| $U_{b,z}$ | Superficial velocity (m/s) | $4.33\times10^{-4}$ |
| $\epsilon$ | Sepharose media porosity (-) | 0.36 |
| $K_b$ | Sepharose media permeability ($m^2$) | $8.67\times10^{-14}$ |
| $\eta$ | FCC atomic packing efficiency (-) | 0.74 |
| $D$ | Diffusion coefficient of PRN ($m^2/s$) | $8.8\times10^{-10}$ |
| $m_{P1}$ | Mass of coupled affinity peptide 1 (g) | $1.87\times10^{-3}$ |
| $m_{P3}$ | Mass of coupled affinity peptide 3 (g) | $5.49\times10^{-3}$ |
| $M_{W,P1}$ | Molecular weight of affinity peptide 1 (g/mol) | 3433.9 |
| $M_{W,P3}$ | Molecular weight of affinity peptide 3 (g/mol) | 3232.6 |
| $M_{W,PRN}$ | Molecular weight of Pertactin (g/mol) | 69000 |
| $k_{a,P1}$ | Affinity peptide 1 association constant (Binding event) ($m^3/s \cdot mol$) | 76 |
| $k_{a,P3}$ | Affinity peptide 3 association constant (Binding event) ($m^3/s \cdot mol$) | 20 |
| $k_d$ | Dissociation constant (Binding event) ($s^{-1}$) | $10^{-10}$ |
| $k_{d'}$ | Dissociation constant (Eluting event) ($s^{-1}$) | 0.3 |
| - | Relative Tolerance | $10^{-3}$ |

The surface concentration of peptides of the reactive resin bed was estimated using approximations for number resin beads (Eq 6.4) to determine the total reactive surface area (Eq 6.5) and surface concentration of the affinity peptides (Eq 6.6). This estimation does not account for any surface area within pores.

$$N = \eta \frac{V_c}{\frac{4}{3}\pi r_{be}^3} \tag{6.4}$$

$$A_{surf} = N 4\pi r_{be}^2 \tag{6.5}$$

$$\begin{aligned} C_{surf} &= \frac{m_{Peptide}}{M_{W,Peptide} A_{surf}} \\ &= \frac{r_{be} m_{Peptide}}{3\eta M_{W,Peptide} A_{surf}} \end{aligned} \tag{6.6}$$

## Bind and Elute Kinetics

Kinetic constants for a 1:1 molar binding ratio were determined using the FortéBio Octet. In this method, streptavidin coated optical biosensors (18-5018, Pall FortéBio, Fremont, CA, USA) were used to attach biotinylated affinity peptides. The peptide decorated biosensors were introduced into wells containing PRN analyte to record the association event. Then the biosensors were washed with 1:10 dilution of 10X Kinetics buffer (18-5032, Pall FortéBio, Fremont, CA, USA) to remove unbound PRN before the sensors were introduced to 1:10 dilution of 10X Kinetics buffer that was adjusted to acidic pH (i.e pH 3 - 6) to facilitate the PRN dissociation from the affinity peptides. The Fortébio measures the biolayer thickness as a function of time as the probe is moved through different wells. During the association step, the biolayer thickness will increase and during disassociation, the thickness will decrease. A more in-depth explanation of the optical biosensor instrument is explained by Abdiche et als from FortéBio (Abdiche et al., 2008).

Associating kinetic constants for P1 and P3 ($k_{a,P1}$ and $k_{a,P3}$) were determined at pH 7. The dissociation constants were determined at acidic pH; however, they were difficult to quantify at pH 3 and 4 (i.e. the pH of the elution buffer during chromatographic purification) since low pH buffer conditions (i.e. less than pH 4) neared the regeneration condition of the biosensor. In low pH buffers the biosensors were striped of all molecules including the biotinylated peptides and the reaction was too fast to record changes in the biolayer thickness (i.e. appeared as a step change). A summary of the kinetic constants determined at different dissociation buffer pH conditions are shown in Appendix B. The simulations were built assuming that the estimated association kinetic constants were correct and that during the column elution stage, there would be complete and instantaneous dissociation of PRN

from the ligand sites.

# Results and Discussion

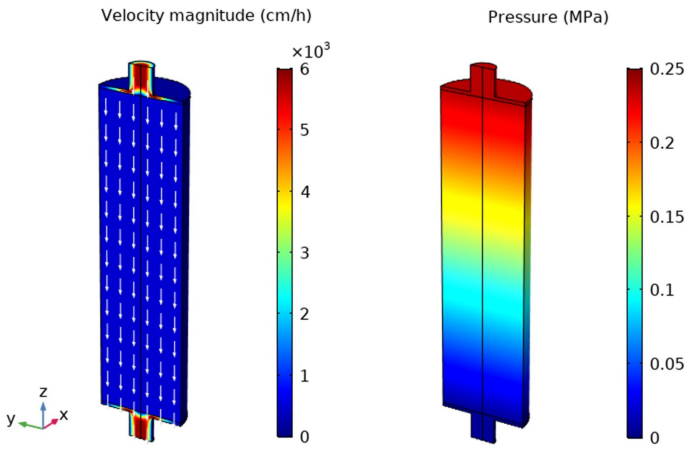


Figure 6.1: Velocity and Pressure profiles used for convective mass transport

Fig 6.1 shows the velocity and pressure profiles for the 1 mL HP HiTrap column which were used to determine the convective mass transport within the column. The manufacture specified maximum pressure drop across the column (delta column pressure) for this column is 0.3 MPa and the measured delta column pressure by the AKTA Pure liquid chromatography system was below this threshold during the experiments.

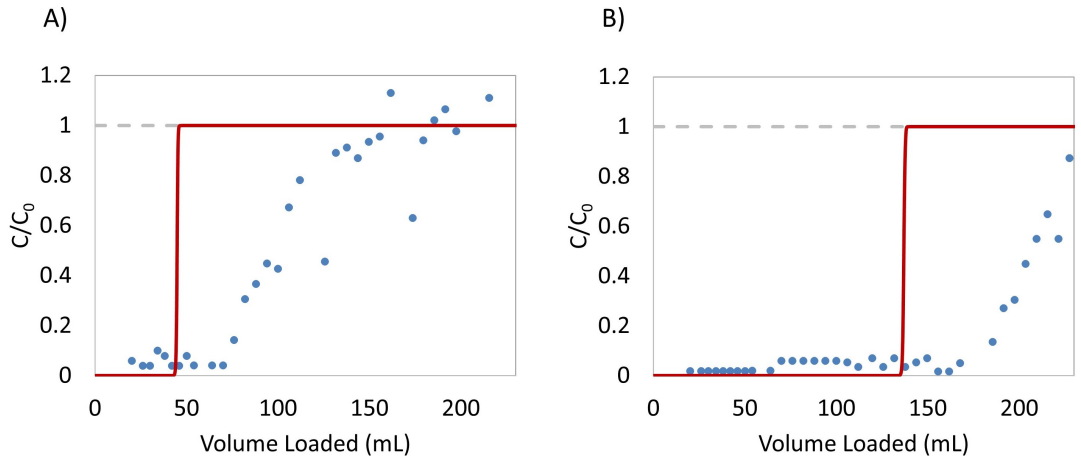


Figure 6.2: Binding Capacity of PRN to Affinity Chromatography Columns at 1 mL/min (red line - simulation, blue dots – experimental) A) Affinity peptide 1 and B) Affinity peptide 3

The binding capacity of the of the two different affinity chromatography columns is shown in Fig 6.2. Column P1 was coupled with 1.9 mg of P1 and column P3 was coupled with 5.5 mg of P3, which would imply that column P1 would have a lower stochiometric binding capacity. The experimental breakthrough was determined by loading feed material into the column and collecting the flow-through. The affinity columns were loaded in 4 blocks of 50 mL of 100x concentrated fermentation broth and intermittently washed with equilibration buffer in order to clear the column of impurities so that any unbound ligand sites would have a greater probability of binding to PRN. The loading scheme onto the column is shown in Fig 6.3. This loading scheme was conducted in lieu of using a pure PRN feed material, as large quantities of pure PRN was not available. The concentration of PRN in the flow-through was estimated by SDS-PAGE and densitometric analysis. One reason for the difference in the steepness of the simulated and experimental breakthrough curves is that the simulation models binding of a PRN feed without considering decreasing binding probability as function of loaded volume. In the experiments, the feed material was primarily impurities with the target molecule making up less than 5% of the feed material. The probability of a PRN molecule finding and binding to the affinity ligand decreases with continual loading and fouling of the column. As a result, there is slow leaking of PRN over a span of 100 mL (100 CVs) until the flow-through concentration equaled the feed concentration. If a purer starting material was used in the experiments, the experimental breakthrough would have been more rapid, since the target protein had a very high binding affinity to the ligands. Including a probability function that described the decrease in the PRN binding probability due to steric hinderance by impurity molecules would make the simulations more representative of the experiments. In addition, the mass of coupled ligand to the resin was determined by tracing the peptide concertation in *pre* and *post* reaction solutions as well as the washing and blocking steps of the coupling reaction using UV at 280 nm and extinction coefficient of each affinity ligand. Any solution that passed through the column was acidified with 2 M Glycine-HCl pH 2.0 to reduce NHS group absorbance to less than 0.005 as specified

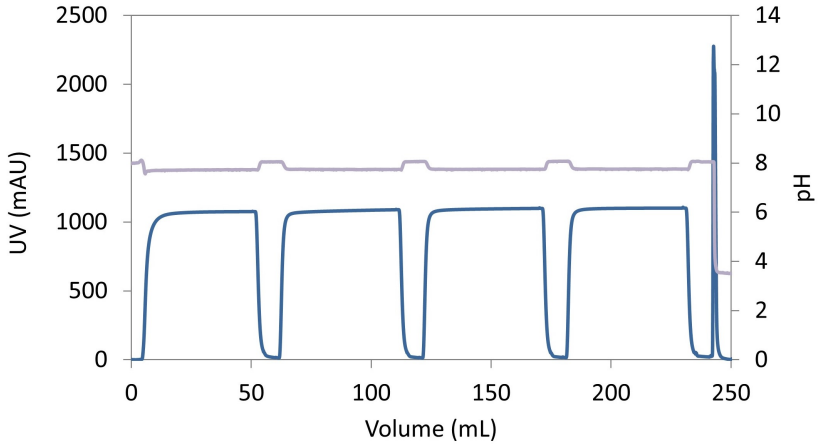


Figure 6.3: The loading pattern of the AC using 4 × 50 mL blocks to determine the dynamic binding capacity of the feed material at 1mL/min

in the manufacturer's instructions. It was difficult to quantify the error in this method for determining the mass of coupled peptide to the resin. As shown in Fig 6.2, the mass of coupled peptide was underestimated by a consistent amount for both columns. If the extent of underestimation of the mass of the coupled peptides was repeatable in additional experiments, then the difference could be artificially corrected.

Fig 6.4 shows the simulated chromatograms for the purification of 50 mL of PRN feed material, which could be compared to Fig 5.1A and Fig 5.2A. In the simulation, the bound PRN molecules are quickly and completely dissociated from the column after a step change to the elution buffer, similar to observations made when eluting the column with pH 3 buffer. As previously suggested, the estimation of the amount of peptide successfully coupled to the resin was underestimated as PRN is found in the flow-through as seen in Fig 6.4A and was not observed in the SDS PAGE analysis. When the elution buffer passes through the bed, the bound PRN was released from the ligand instantly. Fig 6.5 shows the movement and growth of the free PRN front through the bed at different time points after the step change to the elution buffer. The column can be eluted in about 75 s.

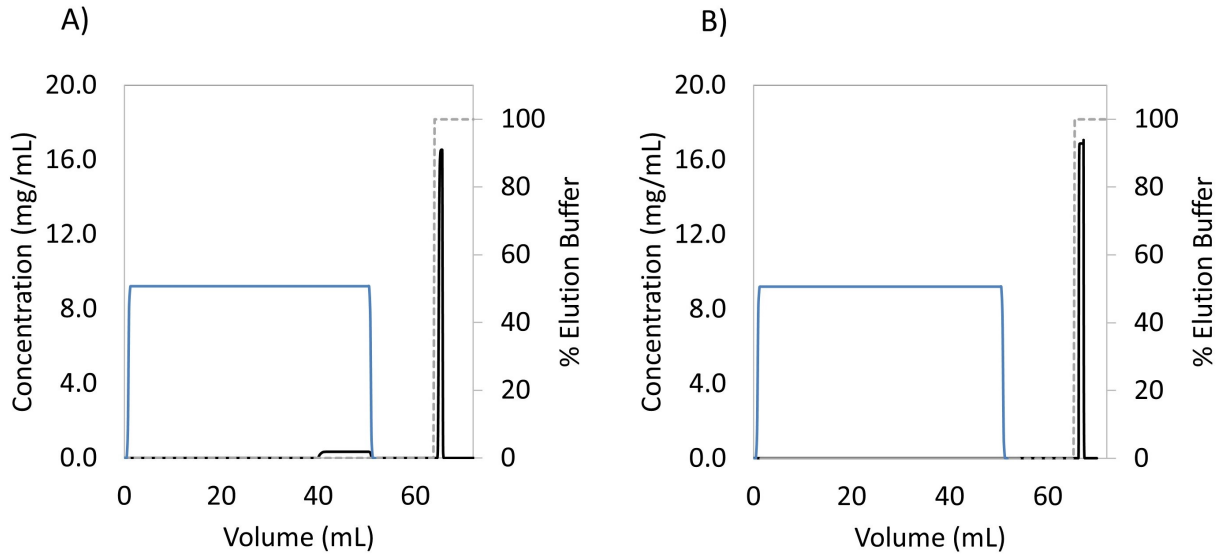


Figure 6.4: Simulated chromatogram of the purification of 50 mL of PRN containing feed material. (black line- PRN, blue line – arbitrary non-binding tracer) A) column coupled with P1 B) column coupled with P3

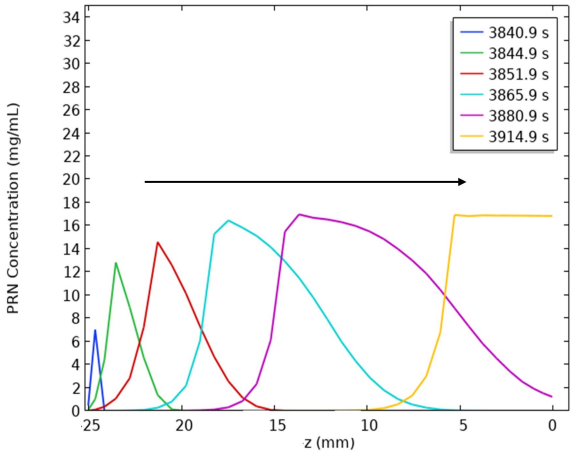


Figure 6.5: Movement of eluted PRN within the P1 bed after a step change to elution conditions.

# Conclusion

The purification of PRN using high affinity peptides was simulated in bind and elute mode. The feed fluid entering the column contained PRN and an arbitrary non-binding tracer that did not interact with PRN or the immobilized ligands on the column. The binding capacity predicted by the simulation did not account for steric hindrance of impurities in the feed; therefore, the breakthrough was steep compared to the shallow breakthrough obtained experimentally. The simulations were more representative of a purer PRN feed. The simulations of the affinity chromatographic purification could be improved by including the key impurities in the feed material and their effect on PRN binding to ligand sites.

## Nomenclature

| | |
|---|---|
| $N$ | Number of resin beads (-) |
| $m_{peptide}$ | Mass of peptide coupled to resin (kg) |
| $\eta$ | Face-centered cubic packing factor |
| $A_{surf}$ | Total surface area on resin beads ($m^2$) |
| $C_{surf}$ | Surface concentration on resin beads ($mol/m^2$) |
| $V_c$ | Column volume ($m^3$) |
| $\epsilon$ | Porosity (-) |
| $K_b$ | Permeability ($m^2$) |
| $P$ | Pressure (Pa) |
| $\mu$ | Fluid dynamic viscosity ($Pa{\cdot}s$) |
| $\rho$ | Fluid density ($kg/m^3$) |
| $\mathbf{I}$ | Identity matrix |
| $\mathbf{u}$ | Fluid velocity field (m/s) |
| $F$ | External Forces (Pa) |
| $R$ | Radius of column (m) |
| $h_c$ | Channel/header height (m) |
| $h_b$ | Packed-bed height (m) |
| $Q_{in}$ | Inlet flow rate ($m^3/s$) |
| $D_i$ | Diffusion coefficient for species $i$ ($m^2/s$) |
| $R_i$ | Reaction rate expression for species $i$ ($mol/m^3 \cdot s$) |

# References

Abdiche Y, Malashock D, Pinkerton A, Pons J. 2008. Determining kinetics and affinities of protein interactions using a parallel real-time label-free biosensor, the Octet. Anal. Biochem. 377:209–217.

Wang C, Soice NP, Ramaswamy S, Gagnon BA, Umana J, Cotoni KA, Bian N, Cheng K-SC. 2007. Cored anion-exchange chromatography media for antibody flow-through purification. J. Chromatogr. A 1155. 19th Annual International Ion Chromatography Symposium:74–84.

# Chapter 7

# Conclusion and Future work

## Conclusion

The purpose of the presented work was to use computational fluid dynamics simulations as a tool to understand the system fluidics and binding kinetics within membrane and resin-based chromatography devices. One of the objectives of biotechnology and pharmaceutical companies is to implement lower cost and highly efficient methods of downstream purification. The devices and methods developed in this work aim to satisfy this goal and present alternatives to currently used methods and practices in downstream bioprocessing.

In chapters 2-4, it was demonstrated that module design and system fluidics greatly affects the efficiency of separation. Based on the CFD simulations, it was identified that conventional chromatography geometries suffer from maldistribution effects caused by both the feed and eluate sides of the bed. The laterally-fed class of chromatographic devices addresses the fluid distribution deficiencies found in these devices by the implementation of lateral feeding and collecting channels above the bed. This flow arrangement allows for velocity balancing by the feeding and collecting channels, which results in a narrow solute RTD. The narrow RTD implies flow-through and elution peaks would be more resolved in multicomponent purification processes, which could result in purer and more concentrated fraction collection. The characteristic velocity pattern within the laterally-fed class of chromatography devices can be translated into other separation technologies such as dialysis, hollow fiber networks and filters. Complementary velocity patterns on the feed and permeate side will help reduce the variability in the solute residence time.

In chapters 5 and 6, the potential of simplifying the multistep purification process of pertactin (PRN) using an affinity chromatography column was investigated. The project was developed out of interest in using modern purification methods such as high-affinity ligands and product development technology such as CFD simulations at Sanofi Pasteur, a vaccine manufacturing company. It was found that as a result of the specific binding between PRN and the affinity ligand, high purity and recovery could be achieved. The affinity chromatography approach to PRN purification is still in the developmental stages and will require future optimization and robustness studies.

In conclusion, the thesis presented two approaches to improving the efficiency in downstream purification: device design and method development.

# Future work

In this thesis, the original designs for the tapered feeding and collecting channels of the LFMC and cuboid packed-bed devices were shown. Presently, the design has evolved and improvements to the design to include branched channels are being made by other members of the group. In addition, reproducing the velocity pattern seen in the laterally-fed class of chromatography devices to reduce the variation in the residence time of different streamlines can be applied to different chromatography and filtration devices.

The affinity chromatography approach to PRN purification is still in the developmental stages and the work presented in this thesis demonstrated the potential and a proof of concept. However, the process is not optimized in terms of all process parameters (i.e. flowrate, column size, type of support matrix, etc.), and I have not proven repeatability and robustness of the resin preparation. In addition, practical considerations such as an in-depth cost analysis, quantification of ligand leaching, and long-term material sourcing logistics need to be made prior to moving forward with the industrialization of the process.

# Appendix A

# DoE ANOVA

Randomized run order was determined by JMP 7.0 while blocking the elution pH parameter.

Table A.1: Run Order

| | Factors | | | | | |
|---|---|---|---|---|---|---|
| Experiment # | Peptide | | Wash Sequence | | Elution pH | |
| 1 | P1 | -1 | Wash (1) + Wash (2) | 1 | 3 | -1 |
| 2 | P1 | -1 | Wash (1) | -1 | 3 | -1 |
| 3 | P3 | 1 | Wash (1) + Wash (2) | 1 | 3 | -1 |
| 4 | P3 | 1 | Wash (1) | -1 | 3 | -1 |
| 5 | P1 | -1 | Wash (1) +Wash (2) | 1 | 4 | 1 |
| 6 | P3 | 1 | Wash (1) + Wash (2) | 1 | 4 | 1 |
| 7 | P3 | 1 | Wash (1) | -1 | 4 | 1 |
| 8 | P1 | -1 | Wash (1) | -1 | 4 | 1 |

**Models:**

$$Yield = 3526.5 - 1823.5pH$$
$$LRV = 2.92875 + 0.26625pH + 0.17375Wash + 0.07375Peptide - 0.05125(Peptide \times Wash)$$

Table A.2: Model fit values

| | $R^2$ | $Q^2$ | $R^2 - Q^2$ |
|---|---|---|---|
| **Yield** | 0.774 | 0.329 | 0.445 |
| **LRV** | 0.998 | 0.984 | 0.0135 |

## Yield

**Actual by Predicted Plot**

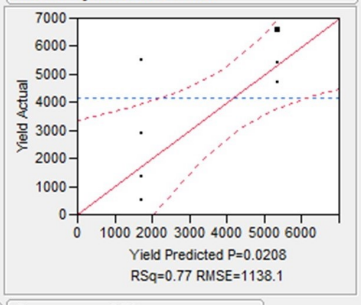


**Summary of Fit**

| | |
|---|---|
| RSquare | 0.773917 |
| RSquare Adj | 0.717396 |
| Root Mean Square Error | 1138.053 |
| Mean of Response | 4134.333 |
| Observations (or Sum Wgts) | 6 |

**Analysis of Variance**

| Source | DF | Sum of Squares | Mean Square | F Ratio |
|---|---|---|---|---|
| Model | 1 | 17734145 | 17734145 | 13.6926 |
| Error | 4 | 5180658 | 1295164.5 | Prob > F |
| C. Total | 5 | 22914803 | | 0.0208* |

**Parameter Estimates**

| Term | Estimate | Std Error | t Ratio | Prob>\|t\| |
|---|---|---|---|---|
| Intercept | 3526.5 | 492.7914 | 7.16 | 0.0020* |
| pH | -1823.5 | 492.7914 | -3.70 | 0.0208* |

**Residual by Predicted Plot**

**Sorted Parameter Estimates**

| Term | Estimate | Std Error | t Ratio | Prob>\|t\| |
|---|---|---|---|---|
| pH | -1823.5 | 492.7914 | -3.70 | 0.0208* |

**Press**

| Press | Press RMSE |
|---|---|
| 15367076.444 | 1600.36852 |

## LRV

**Actual by Predicted Plot**

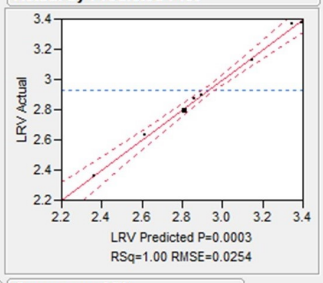


**Summary of Fit**

| | |
|---|---|
| RSquare | 0.997786 |
| RSquare Adj | 0.994834 |
| Root Mean Square Error | 0.025413 |
| Mean of Response | 2.92875 |
| Observations (or Sum Wgts) | 8 |

**Analysis of Variance**

| Source | DF | Sum of Squares | Mean Square | F Ratio |
|---|---|---|---|---|
| Model | 4 | 0.87315000 | 0.218288 | 337.9935 |
| Error | 3 | 0.00193750 | 0.000646 | Prob > F |
| C. Total | 7 | 0.87508750 | | 0.0003* |

**Parameter Estimates**

| Term | Estimate | Std Error | t Ratio | Prob>\|t\| |
|---|---|---|---|---|
| Intercept | 2.92875 | 0.008985 | 325.96 | <.0001* |
| Peptide | 0.07375 | 0.008985 | 8.21 | 0.0038* |
| Wash | 0.17375 | 0.008985 | 19.34 | 0.0003* |
| pH | 0.26625 | 0.008985 | 29.63 | <.0001* |
| Peptide*Wash | -0.05125 | 0.008985 | -5.70 | 0.0107* |

**Residual by Predicted Plot**

**Sorted Parameter Estimates**

| Term | Estimate | Std Error | t Ratio | Prob>\|t\| |
|---|---|---|---|---|
| pH | 0.26625 | 0.008985 | 29.63 | <.0001* |
| Wash | 0.17375 | 0.008985 | 19.34 | 0.0003* |
| Peptide | 0.07375 | 0.008985 | 8.21 | 0.0038* |
| Peptide*Wash | -0.05125 | 0.008985 | -5.70 | 0.0107* |

**Press**

| Press | Press RMSE |
|---|---|
| 0.0137777778 | 0.04149967 |

| Model Fit Indicator | Description | Acceptable Range |
|---|---|---|
| $R^2$ | The percent of the variation of the response explained by the model and it indicates how well the model fits the current data.<br><br>$R^2 = 1 - (SS_{res}/SS_{tot})$<br><br>Where $SS_{res}$ is the sum of squares of the residual and $SS_{tot}$ is the total sum of squares of the response corrected for the mean | 0.5 to 0.75<br>Low significance model<br><br>0.75 to 1.0<br>Good and significant model |
| $Q^2$ | The percent of the variation of the response predicted by the model according to cross validation. Indicates how well the model predicts new data.<br><br>$Q^2 = 1 - (PRESS/SS_{tot})$<br><br>Where $PRESS$ is the prediction residual sum of squares and $SS_{tot}$ is the total sum of squares of the response (Y) corrected for the mean | 0.5 to 1.0<br>Stable model |
| $R^2 - Q^2$ | A difference between $R^2$ and $Q^2$ indicates a level of stability behind the regression model. | 0.0 to 0.3<br>Stable model |

# Appendix B

# FortéBio Curves

Table B.1: Kinetic constants determined using the FortéBio Octet

| Peptide | Association pH | Dissociation pH | $K_a$ (1/Ms) | $K_d$ (1/s) | $K_D$ (M) |
|---|---|---|---|---|---|
| P1 | 7.00 | 6.51 | 75100 ± 100 | $1.5\times10^{-4}\pm 5\times10^{-7}$ | $2.02\times10^{-9}$ |
| P1 | 7.00 | 6.04 | 76300 ± 100 | $2.1\times10^{-4}\pm 4\times10^{-7}$ | $2.75\times10^{-9}$ |
| P1 | 7.00 | 5.10 | 79600 ± 200 | $6.6\times10^{-4}\pm 1\times10^{-6}$ | $8.32\times10^{-9}$ |
| P1 | 7.00 | 4.10 | 24000 ± 1000 | $4.6\times10^{-3}\pm 2\times10^{-5}$ | $1.92\times10^{-7}$ |
| P3 | 7.00 | 6.04 | 20400 ± 300 | $7.2\times10^{-4}\pm 2\times10^{-6}$ | $3.50\times10^{-8}$ |
| P3 | 7.00 | 5.10 | 26000 ± 1000 | $8.4\times10^{-4}\pm 7\times10^{-6}$ | $3.22\times10^{-8}$ |
| P3 | 7.00 | 4.10 | 14000 ± 2000 | $2.9\times10^{-3}\pm 2\times10^{-5}$ | $2.12\times10^{-7}$ |

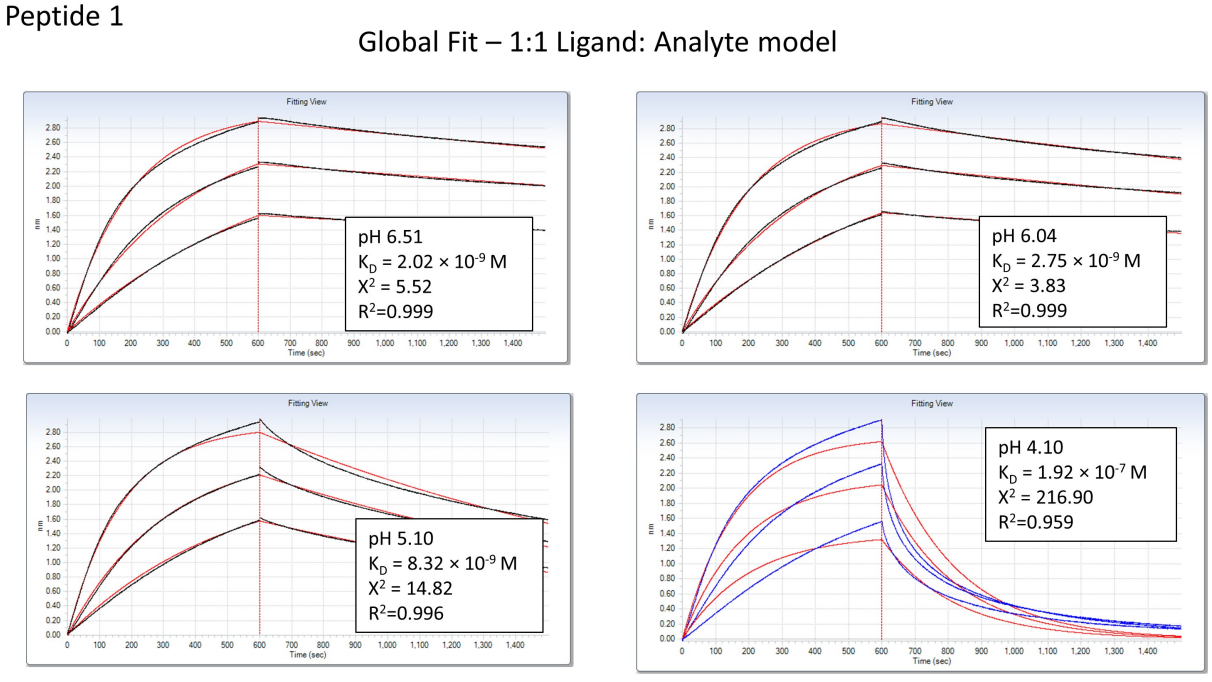


Figure B.1: Binding and dissociating curves using affinity peptide P1 at pH 7 binding and different pH conditions for dissociating.

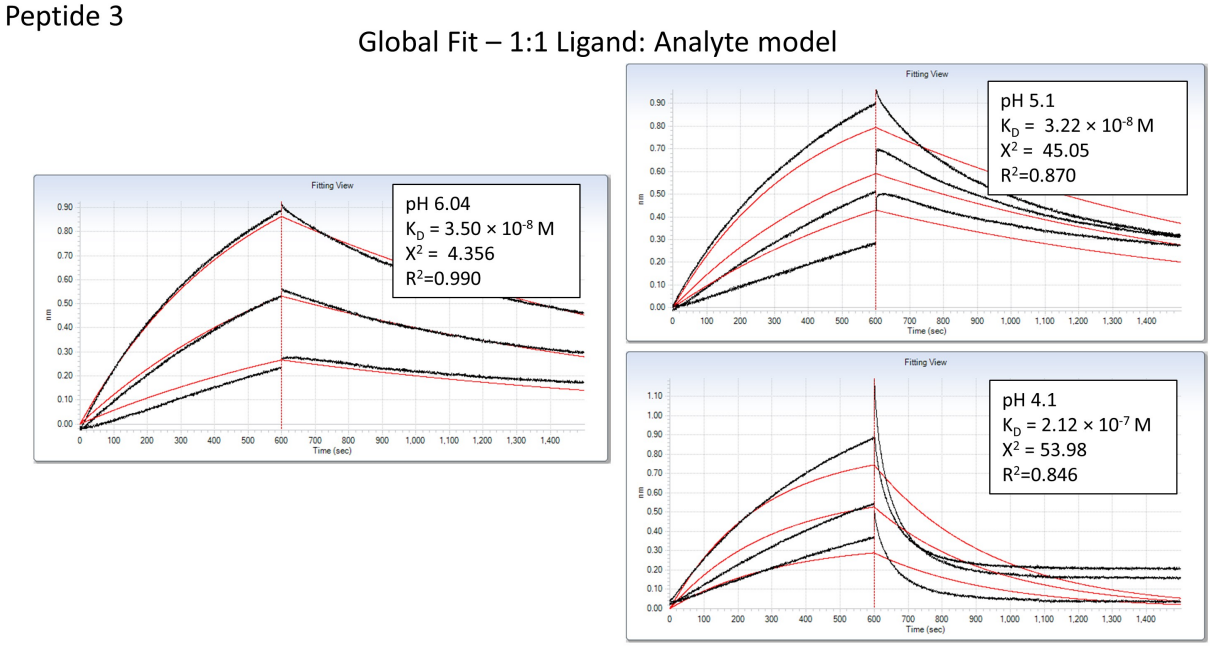


Figure B.2: Binding and dissociating curves using affinity peptide P3 at pH 7 binding and different pH conditions for dissociating.

# Appendix C

# Copyrights

9/9/2019 Rightslink® by Copyright Clearance Center

Copyright Clearance Center RightsLink®

Home | Create Account | Help | LIVE CHAT

**Title:** Computational fluid dynamic (CFD) simulation of laterally-fed membrane chromatography

**Author:** Umatheny Umatheva,Pedram Madadkar,P. Ravi Selvaganapathy,Raja Ghosh

**Publication:** Chemical Engineering Research and Design

**Publisher:** Elsevier

**Date:** September 2018



LOGIN

If you're a copyright.com user, you can login to RightsLink using your copyright.com credentials.

Already a RightsLink user or want to learn more?

Please note that, as the author of this Elsevier article, you retain the right to include it in a thesis or dissertation, provided it is not published commercially. Permission is not required, but please ensure that you reference the journal as the original source. For more information on this and on your other retained rights, please visit: https://www.elsevier.com/about/our-business/policies/copyright#Author-rights

BACK | CLOSE WINDOW